CHAPTER - 2

Literature Review

The present literature review focused on cast 7075 aluminium alloy. Cast Al 7075 alloy has some segregation issues, and it can be overcome by the addition of modifiers, changes in the cooling effect, and heat treatment. The effect of solute segregation and pattern/morphology change on mechanical properties are discussed. The related findings of various modification techniques by different researchers are reported concisely in tabular form. At the end of the section, the research gap and objectives of the work are also discussed.

2.1 Introduction of 7075 aluminium alloy

7075 aluminium alloy is a quaternary alloy of aluminium, zinc, magnesium, and copper, with the minor addition of chromium [8]. The chemical composition of 7075 aluminium alloys is given in Table 2.1.

Table 2.1 Chemical composition of 7075 aluminium alloy as per standard [42–44]

Alloy	Wt.%						
	Zn	Mg	Cu	Mn	Cr	Si (max)	Fe (max)
7075	5.1–6.1	2.1-2.9	1.2-2.0	0.30	0.18-0.28	0.40	0.50

Wrought 7075 aluminium alloys with high strength used in aerospace can replace steel and iron components in high-speed trains to reduce weight [45]. The precipitation-hardened Al 7075 has higher tensile strength because of the formation of coherent and incoherent precipitates [43, 46, 47]. The general characteristics trend of Al 7075-T6 is presented in Figure 2.1. It also shows that the castability and weldability of the alloy are poor, and the strength of the alloy is increased after subsequent heat treatment and forming processes, as shown in Table 2.2. The subsequent microstructural changes during the hot stamping of the sheet are shown in Figure 2.2, where the transformation of the intermediate phase size, shape, and fraction is changed. The finished product's cost is high because of a lengthy process route and operations. The wrought 7075 is used after machining or forming processes followed by

heat treatment, increasing the cost compared to the casting route [48].

Table 2.2 Properties of Al 7075-T6 [43]**.**

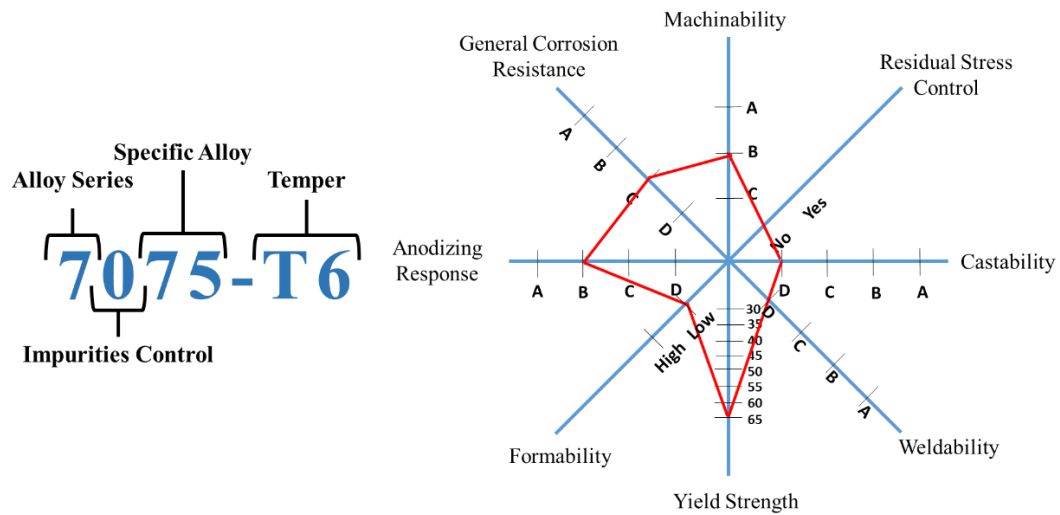| Wrought Alloy	Yield Strength (MPa)	Tensile Strength (MPa)	Elastic Modulus (GPa)	Fatigue Strength (MPa)	Shear Modulus (GPa)	Density (g/cc)	Hardness (BHN)
7075-T6	503	572	72	159	26.9	2.81	150

Figure 2.1 Characteristics of Al7075-T6 with rating A= Excellent, B= Good, C= Fair, and D= Poor [42]**.**
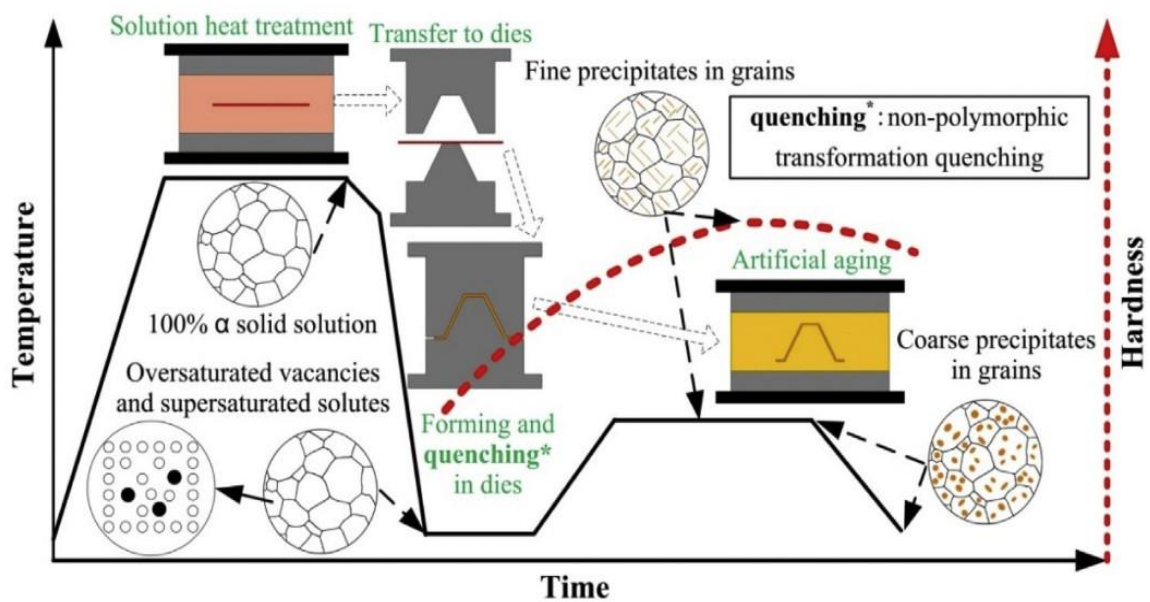

Figure 2.2 Microstructural changes during hot stamping of heat-treatable alloy sheet [49]**.**

Researchers have conducted many studies of the alloy to combat the high cost and castability of 7XXX aluminium alloys. Various casting processes, such as powder metallurgy, rapid solidification, semi-solid metal, and electromagnetic casting, have been used to overcome the poor castability of wrought aluminium alloys [50–53]. Unfortunately, many foundry industries do not commercially favour these casting technologies because of their complexity and additional expenses for particular devices and complex processing techniques. Recently, from a practical standpoint, developing new alloys and changing existing commercial alloys through chemical alloying has been of great interest since these approaches can be efficiently used in typical foundries without requiring extra tools and processes [50, 54–58].

Segregation of solutes and hot tearing due to chemical composition inconsistencies in the macro or microstructure are potential issues with cast Al 7075. Variations in the segregation pattern and the wide freezing range of the alloy can alter the cast Al 7075's morphology, and there is a close relationship between the development of morphology and segregation patterns [11, 56, 59, 60]. The segregation pattern can be changed by adopting some methodologies described in Figure 2.13. Many researchers have applied these methods in their investigations of different alloys. The change in segregation pattern by chemical, mechanical, thermal, and application of post-treatment and semi-solid processing, and many more methods are applied successfully on the 7XXX aluminium alloys [15, 19, 34, 40, 61–64]. A detailed discussion on the particular topic is followed in this chapter.

2.2 Phase diagram of 7XXX aluminium alloy

The quaternary system phase diagram has been vitally important for refining alloy compositions. Scientists started studying the Al-Zn-Mg-Cu diagram by plotting fragments in the 1960s to 1970s [65, 66]. The Al-Zn-Mg-Cu system is strengthened by an increase in zinc, magnesium, and copper concentrations, which leads to secondary segregated metastable phases upon ageing [67]. These metastable phases are formed at grain boundary in as-cast structure, but upon ageing, it is distributed homogeneously depending upon the ageing cycle. Producers often adopt more gentle ageing techniques to stave off the development of a chain network of grain boundary segregations, reducing the strength of aluminium alloys. Step ageing is the course of action suggested for the optimal strength and corrosion resistance combination [68, 69]. The addition of micro-alloying elements like manganese, chromium, and zirconium (inhibit recrystallization) into alloys of the Al-Zn-Mg-Cu system increases strain

hardening [67].

The aluminium alloy system comprises four elements: zinc, magnesium, copper, and silicon. These alloying elements are known as principal alloying elements [43]. The application of alloying elements mainly depends on their solid solubility in aluminium. Seven elements exceed maximum solid solubility by 1% in aluminium (Table 1.1), like magnesium, copper, silicon, lithium, manganese, germanium, and silver, but none is formed a continuous solid solution, and either formed intermediate compound or own solid solution [70]. The supersaturated solid solution of α-Al is decomposed, and 2XXX, 6XXX, and 7XXX alloys are known as precipitation-hardened, dispersion-hardened or age-hardened. Thus, their strength is more excellent than casting alloys from other categories [24].

Various perspectives exist for casting 7XXX system alloys, but they have been extensively used as wrought [11]. The information on invariant reactions from the quaternary phase diagram helps to improve the solidification characteristics for broader applications. The temperature of the low-melting eutectic (T_E) is an essential characteristic of all alloy systems, and it is usually because of the non-equilibrium solidification of alloys [71]. For the Al-Zn-Mg-Cu system, the chemical composition, eutectic phases, and strengthening phase are shown in Table 2.3 [70]. The main phases constituting 7XXX aluminium alloy's microstructure are α-Al, M($MgZn_2$), and T(AlCuMgZn) as a eutectic segregated at the grain boundary [72].

Table 2.3 Chemical composition, eutectic phase, and strengthening phase for the Al-Zn-Cu-Mg system [70].

System	Mass%			Phase composition of eutectics	Strengthening phases*	T_E (°C)
	Mg	**Cu**	**Zn**			
Al-Zn-Mg-Cu	1.5-2.5	0.4-1.5	5-8	(Al) +M+T (Al, Cu, Mg, Zn)	η ($MgZn_2$), η' ($MgZn_2$)	470-475

The formation of eutectic and strengthening phases is studied from the phase diagram. The multi-component or high-order phase diagrams are complex, but the polythermal, ternary diagram isotherms help to study the phase formation [66]. Figure 2.3 shows the ternary phase diagram of Al-Cu-Zn at 350 °C with Al-Cu, Al-Zn, and Cu-Zn binary phase diagrams. Klopotov et al. [73] studied that the ternary diagram forms the binary α-phase (FCC), β-phase (SC) and ternary γ-phase (copper-based), and noticed that the different amounts of copper

in solid solution of zinc and aluminium alloys form a lattice difference in the identical crystal lattice of α and β phases.
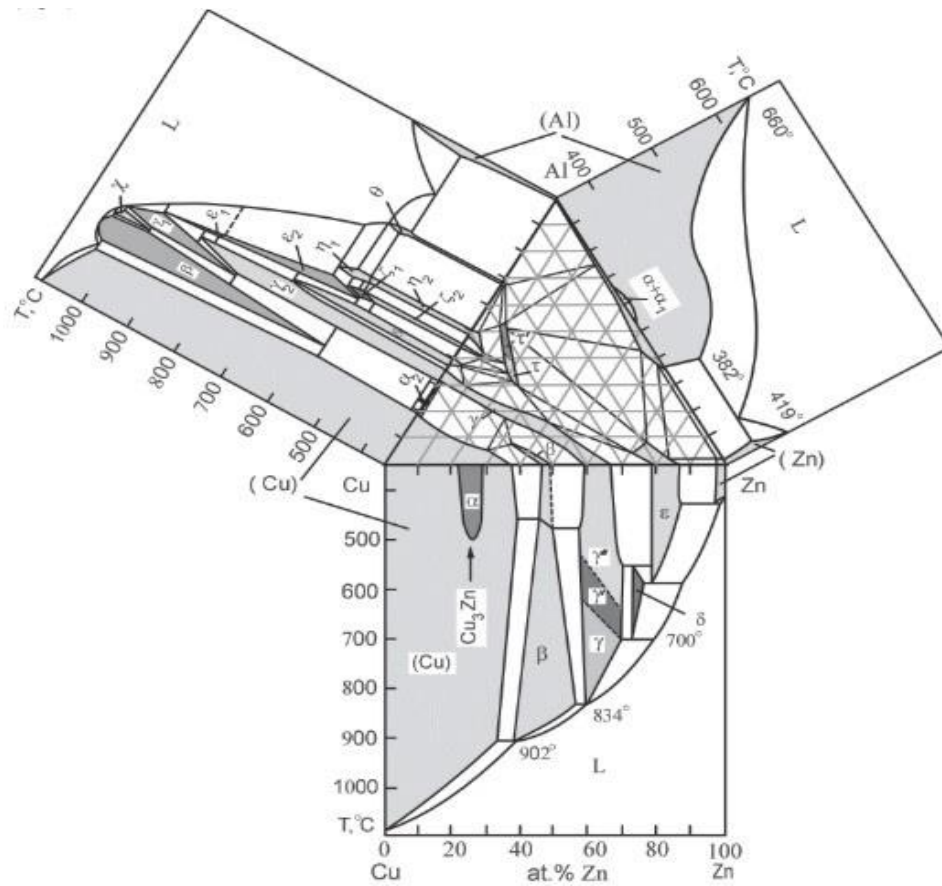

Figure 2.3 Isothermal section of the ternary phase diagram of Al-Cu-Zn at 350 °C with Al-Cu, Al-Zn, and Cu-Zn binary phase diagrams [73].
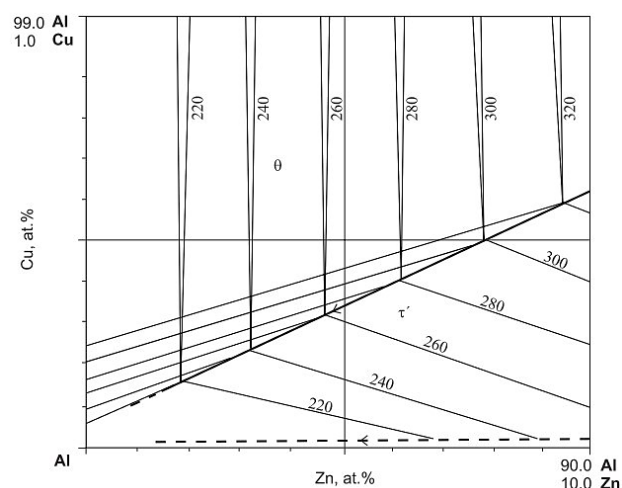

Figure 2.4 Solvus of the (Al) phase and three-phase equilibrium (Al) + θ + τ at different temperatures [°C] [74].

11

The highest amount of Cu that can be dissolved in (α-Al) is 5.5% if there is no Zn present, and the maximum amount of Zn that can be dissolved is 83.1% when there is no Cu. In equilibrium with θ, the amount of Cu dissolved in (Al) increases with a rise in Zn, while in the (α-Al) + τ two-phase field, it declines as the Zn content rises, as shown in Figure 2.4 [74].

The construction of higher-order phase diagrams with over three components requires computation, and nowadays, it is possible using CALPHAD [71, 75, 76], FACTSAGE [19, 77, 78], PANDAT [79–81], and many more. Many researchers used computational software to study the multi-component phase diagram and concluded the phase formation at different temperatures [81].
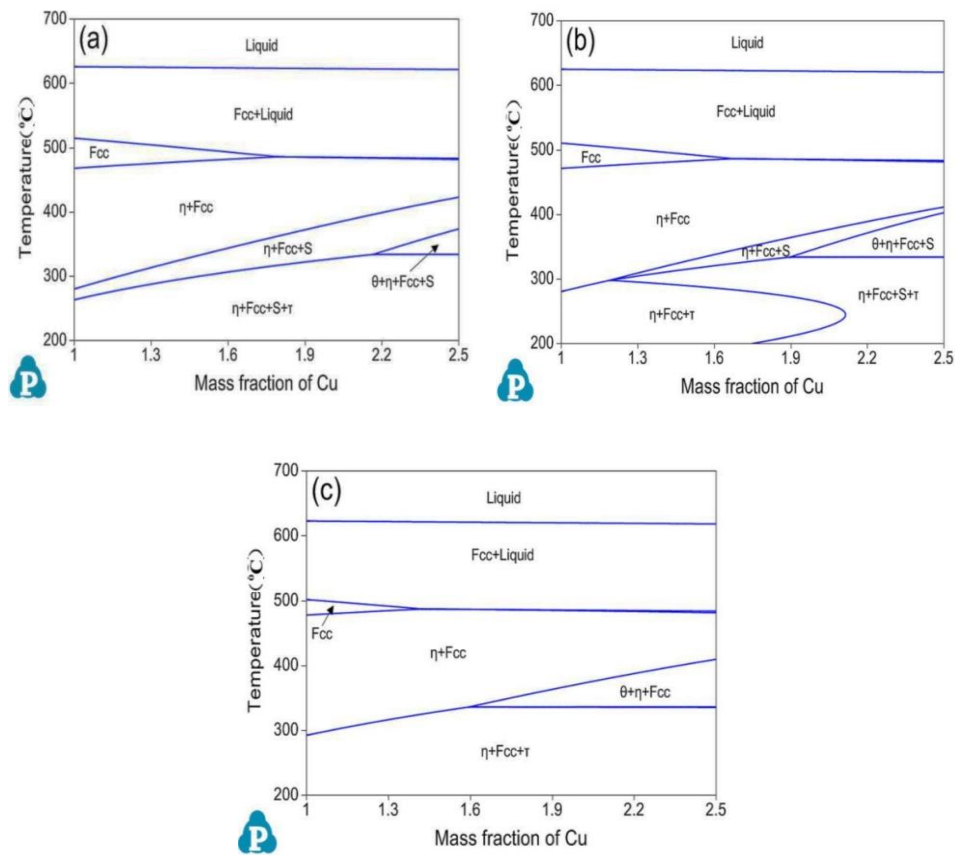

Figure 2.5 Calculated vertical section of the Al-Zn-Mg-Cu phase diagram for (a) Al-10.5Zn-2.2Mg-xCu, (b) Al-11Zn-2.2Mg-xCu, (c) Al-12Zn-2.2Mg-xCu [4].

Using Pandat software, Wang et al. studied the vertical sections of the Al-Zn-Mg-Cu phase diagram for (a) Al-10.5Zn-2.2Mg-xCu, (b) Al-11Zn-2.2Mg-xCu and (c) Al-12Zn-2.2Mg-xCu alloys with different Cu content ($1 \leq x \leq 2.5$ wt.%). It was noticed that the single-phase FCC region disappears at nearly 500 °C temperature (above and below) when the content of

Cu is higher than 1.8 wt.%. The copper content is set below 1.8 wt.% to get a single-phase region for homogenization and heat treatment [4], as shown in Figure 2.5 (a to c). Data suggests magnesium is almost insoluble in the Al_2Cu phase, while Zn dissolves in amounts not over 2%. In the Al_2CuMg phase, the solubility of Zn does not exceed 1%.

Polythermal sections in Figure 2.6 reveal that regardless of the different concentrations of zinc, magnesium, and copper being studied, the alloys crystallize almost identically. The formation of a primary crystal of α-Al solid solution surrounded by liquid, containing 5% Cu in an alloy, and crystallization is finished with a solidus temperature of ~500–530°C [82]. However, the outrageous amount of copper in the alloy decreases the solidus temperature as its content exceeds the solubility limit, and an increase in zinc amount further decreases the solidus temperature. The ternary Al-Cu-Zn phase diagram concluded that the Al_2Cu, $Al_3Cu_5Zn_5$, $CuZn_5$, and Zn are in equilibrium with aluminium shown in Figure 2.7 (a), and the last two phases are most stable at high concentrations of copper and zinc [65].
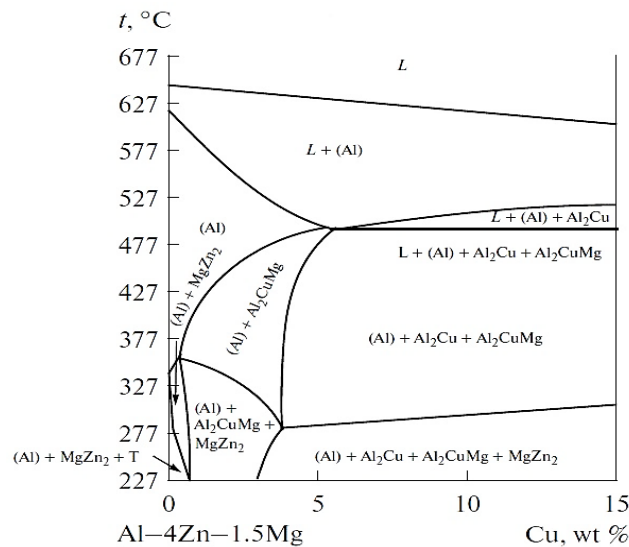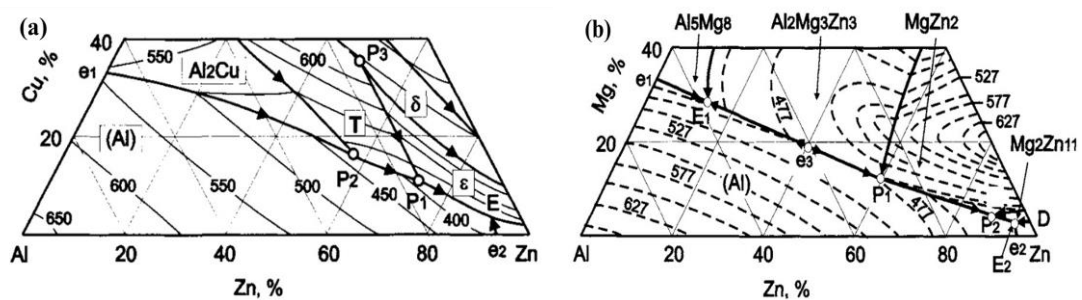

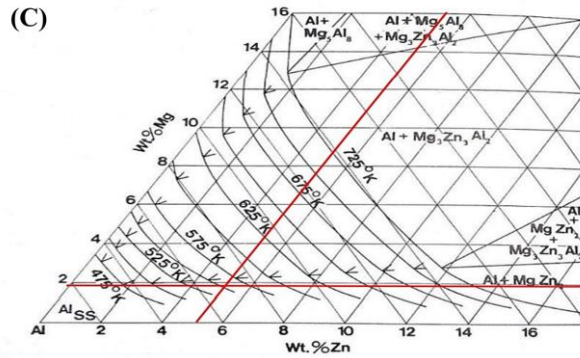**Figure 2.6 Polythermal section of Al-4% Zn—1.5% Mg-Cu [82].**

Figure 2.7 Projection of liquidus surface in the aluminium corner of (a) Al-Cu-Zn system; T–Al₃Cu₃Zn₂, ε–CuZn₅; and δ–a solid solution based on AlCu, (b) Al-Mg-Zn system [83]**, and (c) Al-Zn-Mg (red line shows Al-5.1Zn-1.9Mg)** [84]**.**

Table 2.4 shows that the mutual solid solubility of Cu and Zn is congruent with the respective binary system.

Table 2.4 Limit solubility of Cu and Zn in solid (Al) of Al-Cu-Zn system [83]**.**

T, °C	427	377	352	327	277	227
Cu,%	2.7	1.8	1.5	1.3	0.7	0.45
Zn,%	70	47	43	29	14	6

Figure 2.7 (b) provides a visual representation of the liquidus surface of the Al-Mg-Zn phase diagram. In the Al-Mg-Zn system, two quasi-binary segments can be identified, namely Al-Al₂Mg₃Zn₃ (489°C) and Al-MgZn₂ (475°C). Al-MgZn₂ exhibits a three-phase invariant transformation that is aligned with the four-phase transformation.

Table 2.5 Limit solubility of Mg and Zn in solid aluminium in the Al-Mg-Zn system [85]**.**

Phase region	T, °C	475	460	447	440	400	350	300	200
(Al) + Al₈Mg₅ + Al₂Mg₃Zn₃	**Mg,%**	-	-	12.5	12.3	10.5	8.4	6.0	2.8
	Zn,%	-	-	1.8	1.6	1.1	0.6	0.4	0.2
(Al) + MgZn₂ + Al₂Mg₃Zn₃	**Mg,%**	2.8	2.6	-	2.3	1.7	1.1	0.7	0.2
	Zn,%	14.3	12.5	-	11.4	8.6	6.0	3.7	1.0

Table 2.5 shows that the solubility of Mg and Zn in (Al) decreases significantly as the

temperature lowers. The development of GP zones and unstable versions of the second phases, $Al_2Mg_3Zn_3$ (T') and $MgZn_2$ (η'), substantially impact precipitation hardening. The non-equilibrium eutectics are formed during solidification, typically composed of $Al_2Mg_3Zn_3$ and $MgZn_2$ [66]. Figure 2.7 (c) shows the liquidus sections of Al-Zn-Mg. Putra et al. reported that Mg5Al8 and Mg3Zn3Al2 second phases dissolve in the α-Al matrix higher than 277 °C, and these phases have been completely dissolved, and their solubility has risen at 460 °C [84]. Summarizing the liquidus section of Al-Cu-Zn, Al-Mg-Zn, and Al-Zn-Mg ternary phase diagrams, the second phases are completely dissolved above nearly 450 °C.

Figure 2.8 shows the vertical section of the Al-Zn Mg ternary phase diagram. At lower concentrations of magnesium, the formation of α + η + τ (ternary eutectic phase), and α + η (binary eutectic phase) exists at the grain boundary during the solidification of this alloy [86].
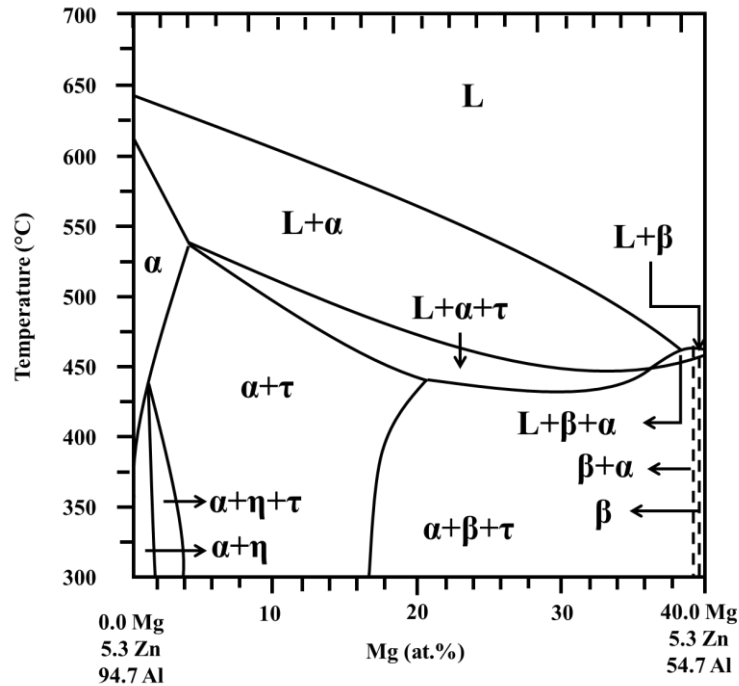

Figure 2.8 Vertical section ternary phase diagram of Al-Zn-Mg at 5.3 at.% [86].

The equilibrium phase diagram can show the formation of phases in an Al-Zn-Mg-Cu alloy and it is complex for the Al-Zn-Mg-Cu alloy. So the illustration of the phase diagram is crucial. Liang et al. [87] revealed how solubility works between Al-Cu, Mg-Zn, Al-Mg-Cu and Al-Mg-Zn phases and showed a primary spatial relationship between the phases in the phase diagram. Later, Mondolfo et al. [83] presented the integration of Al-Mg-Zn and Al-Mg-Cu phase regions. The Al-Zn-Mg-Cu alloy phase diagram in the Al-rich corner can be

depicted using the studies of the Al-Mg-Zn, Al-Mg-Cu, and Al-Cu-Zn phase diagrams, shown in Figure 2.9. The η ($MgZn_2$), θ (Al_2Cu), S (Al_2CuMg) and T (AlZnMgCu) may be seen in the Al-Zn-Mg-Cu alloy's phase diagram. It can be concluded that the transformation of phases during solidification is determined by the emergence of Mg-Zn, Al-Cu, Al-Cu-Mg and Al-Zn-Mg-Cu phases. The amount of Mg and Zn in the Mg-Zn binary phase diagram plays a critical role in determining the phase composition, and the temperature range for Mg-Zn remains stable from 320 °C to 580 °C [88].
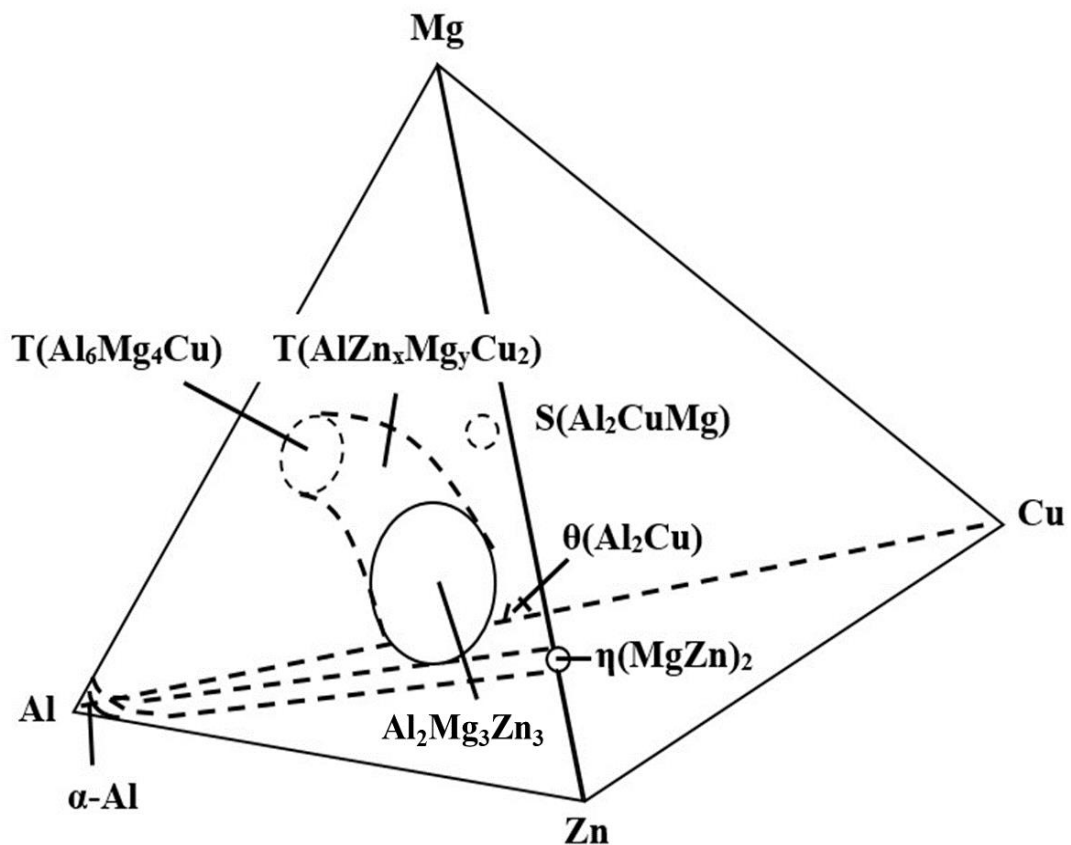

Figure 2.9 Aluminium-rich corner of Al-Zn-Mg-Cu phase diagram [64, 88]**.**

The precipitation hardening of an alloy enriched with Zn and Mg occurs in the planar zones because of the formation of insightful precipitates in the M-Phase. The M-Phase composition shifts from $MgZn_2$ to CuMgAl in a quaternary structure, presented as Mg [Al, Cu, Zn]$_2$ [64]. Figure 2.10 shows the range of phase formation composition in the 3D view phase diagram of Al-Cu-Zn-Mg. It is a significant character of this phase diagram that the 3 stages of the Al-Mg-Zn system and the 3 stages of the Al-Cu-Mg system form continuous solid solutions. The Al-Cu-Mg system needs to be balanced so that zinc is added to the CuMgAl and

$Cu_6Al_2Mg_7$ compounds to reach equilibrium. Three domains can be found in the continuing solid solution created by $CuMg_4Al_6$ and $Mg_3Zn_3Al_2$, $MgZn_2$ and $CuMgAl$, and $Cu_6Mg_2Al_5$ and Mg_2Zn_{11} [89].
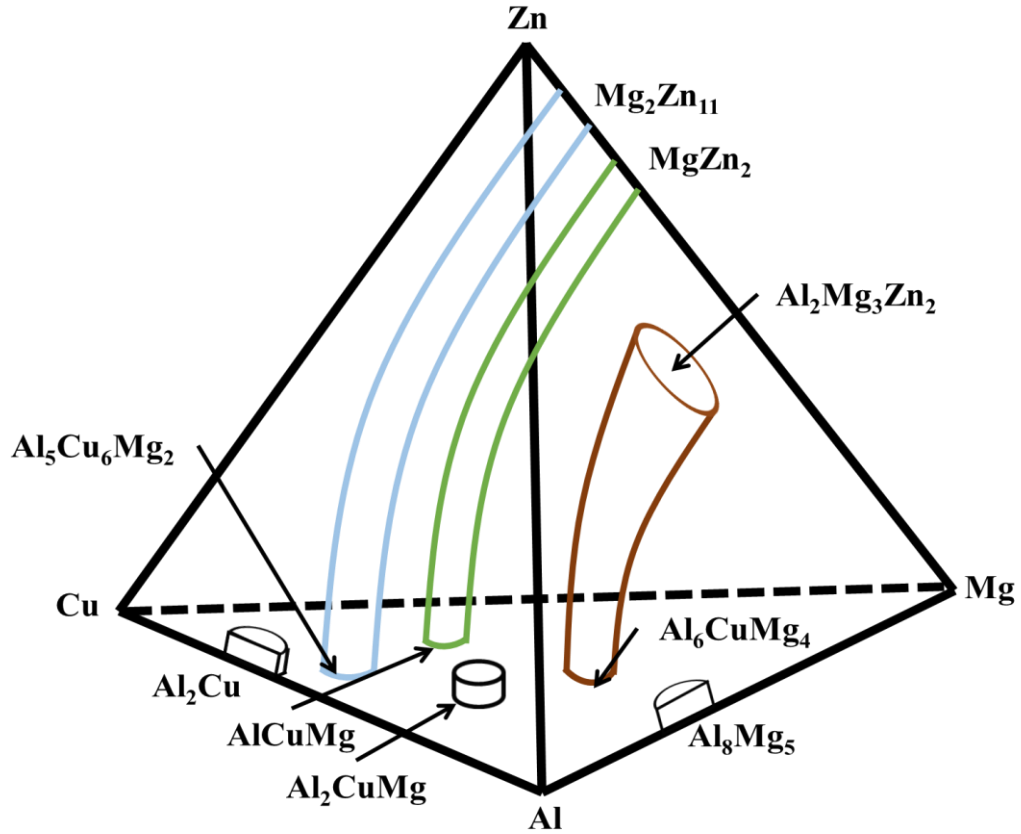

Figure 2.10 Aspect of 3D view of Al-Cu-Zn-Mg phase diagram with compositional ranges of phases [66, 89]**.**

Finally, insightful information on the phase diagram helps to change the structure-property relationship. Zn, Mg and Cu are all essential in the development of key phases like the η ($MgZn_2$) phase, S (Al_2CuMg) phase and T (AlCuMgZn) phase, which will have a major influence on the properties [90]. Additional trace elements and contaminants, like Ti, Zr, Fe and Si, will also affect the microstructure by creating intermetallic compounds [91]. The 7xxx aluminium alloys can be enhanced to create the ideal balance of properties through modifications of the microstructure by the addition of modifiers/refiners to the alloy mixture and heat treatment. In addition, the Zn/Mg ratio is an essential factor in determining the precipitation reactions and phases that occur, with a Zn/Mg ratio of 2.0 being the critical value below which T becomes more likely than η [92].

The cooling curve and the time-temperature and transformation diagram are also meaningful to understanding the formation of the eutectic phase during solidification. Chinella et al. presented a cooling curve and TTT diagram for Al 7075 using JMatPro in Table 2.6.

Table 2.6 JMatPro TTT and CCT curve critical times and temperatures of 7075 [92].

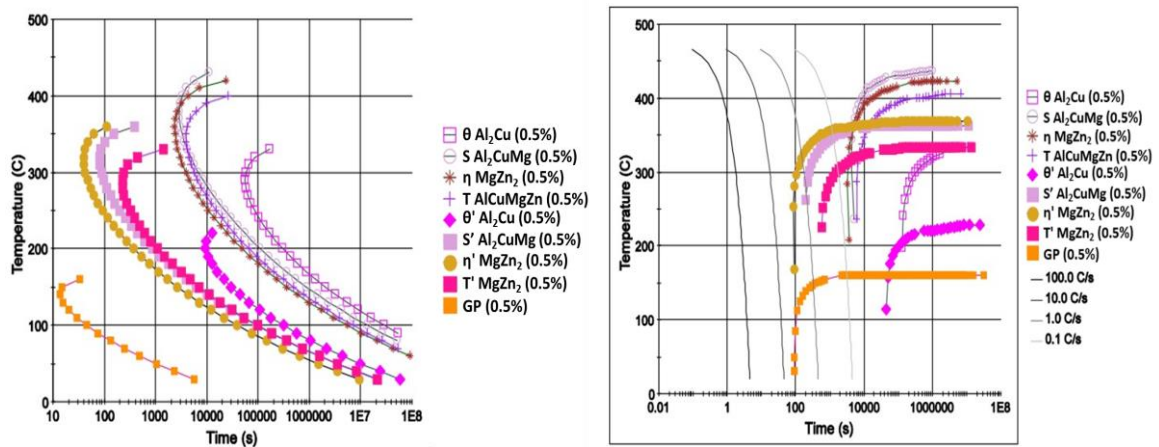| Alloy	Mg, wt.%	(Zn+Mg), wt.%	TTT Nose			CCT cooling rate (°C/s)
			Phase	Time (s)	Temp. (°C)	
7075	2.5	8.1	GP	14	140	10
			η'	40	320	-
			S'	80	320	-
			T'	230	280	-
			η	2300	350	-

Figure 2.11 Calculated TTT, and CCT curve for 7075 (start temperature = 475 °C) by JMatPro [92].

Figure 2.11 shows the TTT and CCT curve for Al 7075 drawn using JMatPro. TTT curves help to expect phases by scheduling the cycle for the solution and age-hardening heat treatments [93]. CCT curves can aid in determining the proper cooling rates and intervals to achieve the desired microstructures or avoid undesired precipitates in cooling castings or when using quenching processes after solution treatment of wrought alloys to plan phase formation [94].

2.3 Effect of Grain Refiners and Modifiers on the 7XXX aluminium alloys

In recent years, there have been higher expectations for improved mechanical performance from aluminium alloys. Various techniques are used to reach that goal, mainly purifying and grain refinement, which has dramatically affected the mechanical performance of aluminium products [34, 95]. To satisfy the performance, the quality of the product should be remarkable. The quality improvement in bulk production processes like casting can be upgraded using grain refinement and cleaning of molten metal and is desirable during the melting process and solidification process. Grain refinement is an efficient and effective method of increasing metallic materials' strength and plasticity [96]. The Hall–Petch relation theoretically explains the most significant improvement through grain refinement by increasing strength at room temperature [97]. The addition of different reinforcement, modifiers, micro-alloying elements, and hybrid reinforcement are listed in Figure 2.12. In the inorganic category, oxide, boride, carbides, nitride, and sulphide are added in cast Al 7075 [10].
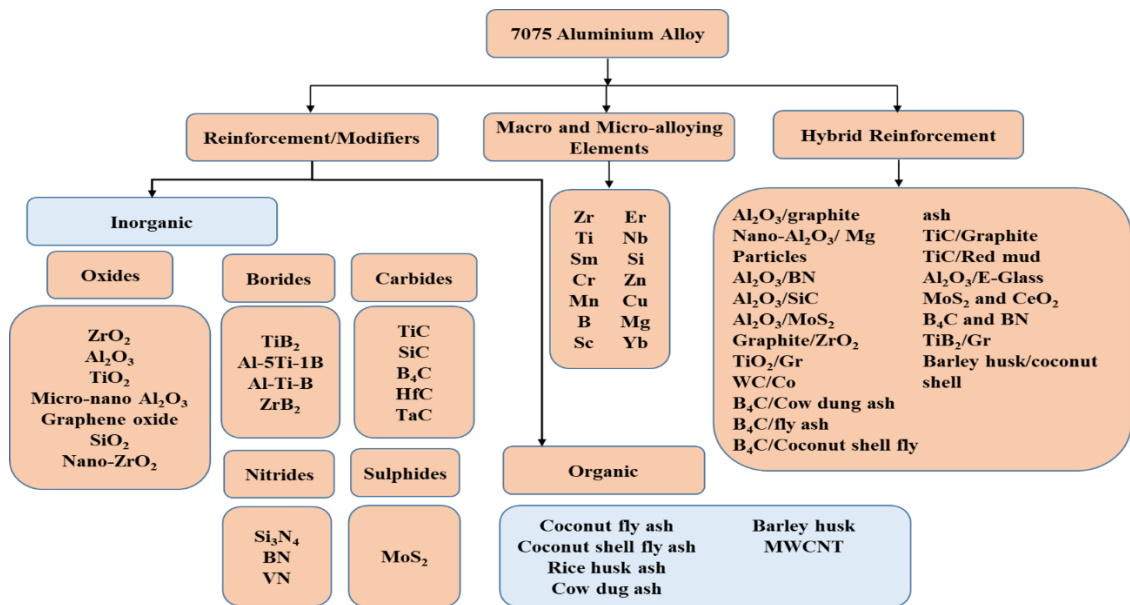

Figure 2.12 List of different reinforcement, modifier, macro and micro-alloying elements, and hybrid reinforcement in 7075 aluminium alloy [10]

As discussed in previous Section 1.1, the quality issue with the casting of Al 7075 is because of poor response towards castability and solute segregation because of high solute concentration. To control the issues, the process modification can alter the microstructure. In the last decade, many researchers adopted many ways to change the microstructure;

chemical treatment, thermal treatment, mechanical treatment, post-treatments, severe plastic deformation (SPD) processes, and much more processing, as shown in Figure 2.13. The detailed schematic of these treatments is illustrated in Figure 2.15. Chemical composition, parameters of solidification, additives included, and heat treatment are the parameters that affect the microstructure and mechanical properties [98]. The enhancement of mechanical strength in the mushy zone was estimated according to chemical composition, depending on the amount and nature of the alloying element, grain refinement or modification, and eutectic morphology change.

Chemical processing is employed in the industrial sector and blending modification has become an area of intense study [99]. Grain refiners, modifiers, and micro-alloying elements can change the eutectic morphology without disrupting the existing facility of the foundry shops, which is less expensive than other methods.
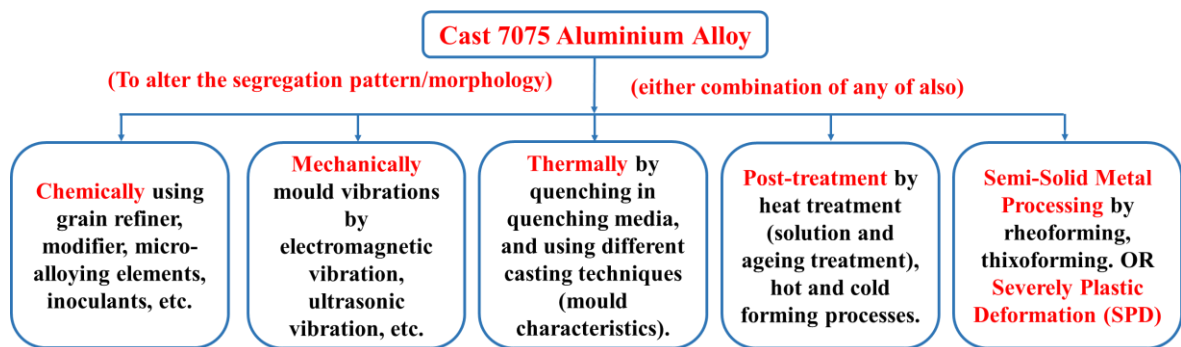

Figure 2.13 Several ways to change the segregation pattern/morphology of cast Al 7075 microstructure.

The addition of modifiers, refiners or micro-alloying elements affects the segregation pattern of 7XXX aluminium alloy [19, 45, 99, 100]. Over the past few years, many researchers have conducted an in-depth study of the 7075 aluminium alloy to gain a better understanding of the segregation behaviour and associated casting issues [59, 61, 101–103]. Many researchers investigated by adding oxide [104, 105], boride [89, 106], carbide [107–112], nitride [113], sulphide [114], micro-alloying elements [11, 26], organic reinforcement [115–117], and hybrid reinforcement [106, 115, 116, 118–123] in 7075 aluminium alloy, as presented in Figure 2.12.

The primary motive for the addition of reinforcement/modifier is the modification of microstructure, and an improvement in the mechanical, physical, wear, and corrosion properties. The solidification of metallic materials can be segmented into three stages,

considering their particular features and the ultimate effect on the solidified microstructure: early-stage solidification (ESS), middle-stage solidification (MSS) and last-stage solidification (LSS) [124]. The effect of these solidification stages is presented in Figure 2.14. Most of the past research has focused on middle-stage solidification (MSS), which is mainly on dendritic growth. The early-stage solidification resulting in a wider solidification range leads to macro-segregation issues. [125]

The early stage of solidification can be managed by the addition of selected elements or refiner/modifiers, which alters the chemical segregation at the liquid/solid interface to enhance the heterogeneous nucleation.
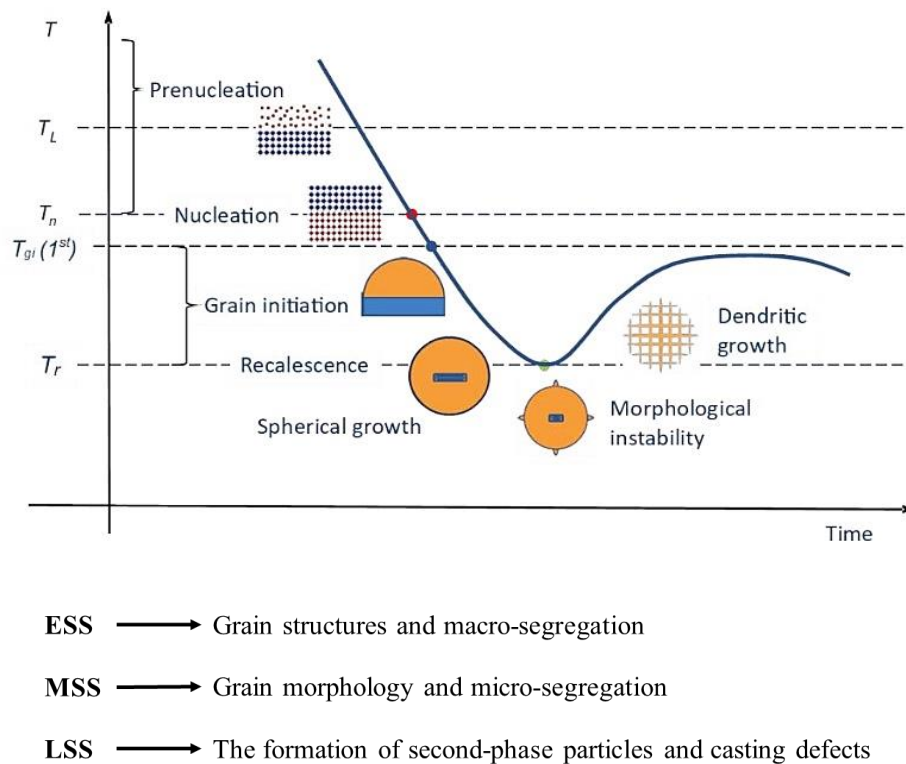

ESS ⟶ Grain structures and macro-segregation

MSS ⟶ Grain morphology and micro-segregation

LSS ⟶ The formation of second-phase particles and casting defects

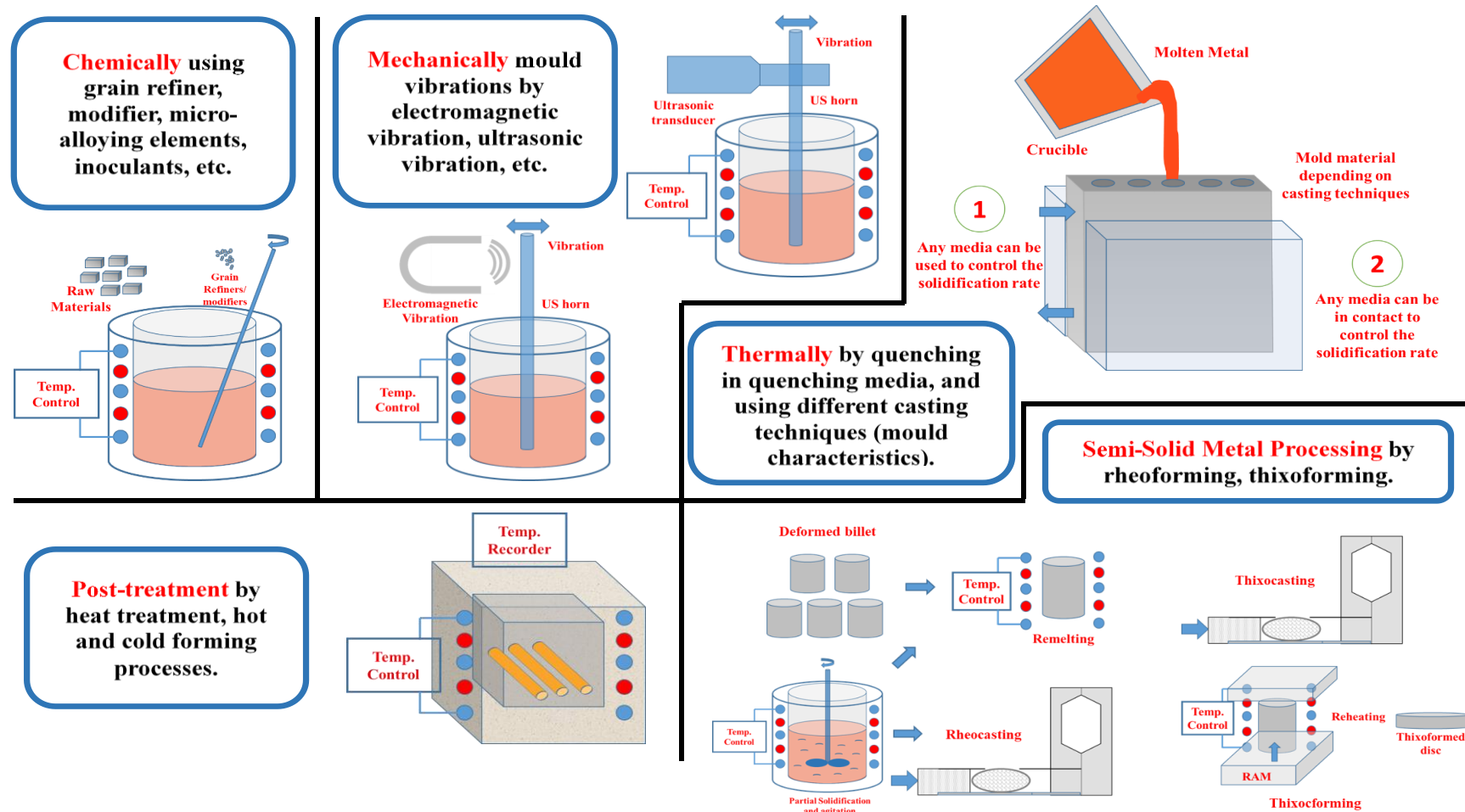**Figure 2.14 Effect of solidification stages on the solidified microstructure [124].**

Figure 2.15 Schematic illustration of different treatments applied to alter the segregation pattern [15, 19, 34, 40, 61–64, 126]**.**

.

Some researchers have used different grain refiners and modifiers, and their approaches are outlined in Table 2.7.

Table 2.7 Addition of grain refiners and modifiers via different approaches by researchers.

Types of reinforcement/ modifiers or combination	Particle size	Quantity	Production approach	References
Al_2O_3	Nano	1.5% wt.	Casting	[127]
SiC	7–34μm	6 & 9% wt.	Centrifugal Casting	[128]
Ti & Gr	≤80 & ≤150 μm	3, 5, 6 & 8% wt. combined	In situ process	[129]
TiB_2	Nano size	1.5% vol.	In-situ process	[130]
TiB_2	20-500 nm	6% wt.	In-situ process	[131, 132]
TiB_2 & Gr	–	1.5–6 & 1% wt.	In-situ process	[133]
TiC	6-8 μm	–	laser shock peening (LSP) and friction stir welding (FSW)	[134]
SiC & B_4C	10 & 5mm	1:1 vol. fraction	Liquid pressing process	[135]
Gr	–	Up to 15% wt.	Mechanical alloying and hot extrusion	[136]
Ag-C NP	10-20 nm	0.5-2.0% wt.	Mechanical milling	[137]
Gr	38.33 μm	0.5-1.5% wt.	Mechanical milling	[138]
TiO_2	30-40 nm	10-20% wt.	Mechanical milling	[139]
ZrO_2	110 nm	2 & 5% wt.	Mechanical milling	[140]
SiC	80nm	1% vol.	Rheoforming	[141]
(SiC+Ti)	7 & 35 μm	(40+5) %vol.	Squeeze Casting	[142]
SiC & Cr	7±0.6 & 30±1.4 mm	50 & 5 %vol.	Squeeze casting	[143]
SiC	20μm	10, 15 & 20% vol.	Stir casting	[144, 145]
SiC	20–40μm	10% wt.	Stir casting	[146, 147]
SiC	150μm	2–6% wt.	Stir casting	[109]
SiC	20–40μm	10 & 15% wt.	Stir casting	[148]
SiC	Ranges from 45 nm–50 μm	Ranges from 1 to 15% wt.	Stir casting	[149–152]
MWCNTs	30 nm	1-3% wt.	Stir Casting	[153]
Al_2O_3	36-72 μm	-	Stir Casting	[154]

TiC	–	2.5–7.5% wt.	Stir casting	[155]
TiB$_2$	–	15% wt.	Stir casting	[149]
Si$_3$N$_4$	–	2-8% wt.	Stir casting	[156]
MoSi$_2$	2–8 μm	2–5% wt.	Stir casting	[157]
ZrB$_2$ & hBN	5 & 3 mm	5% wt. each	Stir-squeeze cast technique	[158]
Al$_2$O$_3$ & h-BN	5-10 μm each	2.5 & 5% wt. each	Two-step stir casting	[159]

Figure 2.16 illustrates the percentage utilization of various grain refiners and modifiers added to Al 7075. A recent survey by Soni et al. [160] on the addition of grain refiners/modifiers shows that over 10 percentage research work was done on the addition of SiC, Al$_2$O$_3$, B$_4$C, and graphite in 7075 aluminium alloy. Sowrabh et al. [10] critically compiled a merged review of the addition of reinforcements, production techniques, and their effects on the properties of Al 7075. Table 2.7 shows the various production approaches and reports that stir casting is economical, flexible, and suitable for making large amounts of materials easily, but improper distribution, inadequate wetting, porosity formation from excessive stirring and agglomeration of reinforcement are issues [161, 162].
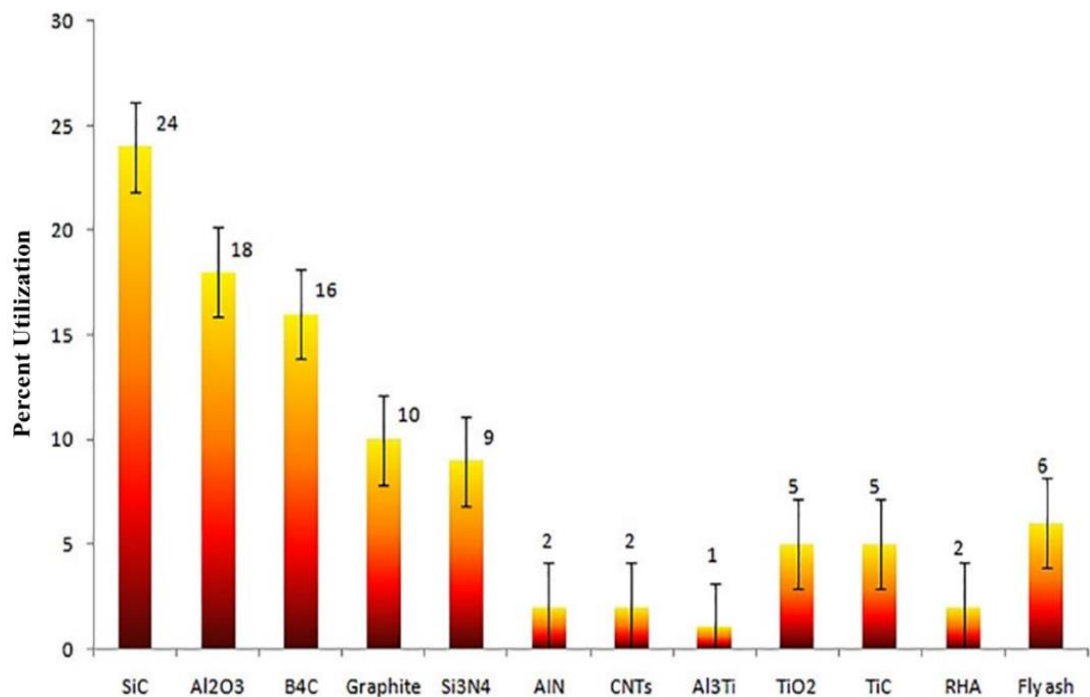

Figure 2.16 Percentage utilization of grain refiners and modifiers in Al 7075 [160]**.**

Yuxin et al. [19, 100] summarize the effect of alloying elements, the formation of precipitates, and their effects on the properties of Al-Zn-Mg-Cu, presented in Table 2.8.

Table 2.8 Summary of alloy elements, precipitates, and major effects on properties of Al-Zn-Mg-Cu [19].

Element	Precipitate	Content (wt.%)	Major effects
Zn + Mg	η (MgZn$_2$); T (Al$_2$Mg$_2$Zn$_3$)	0.0–10 (Zn $\geq$ 0.9)	Increased tensile strength heat treatment effect
		Zn + Mg $\geq$ 10%	Decreased conductivity, fracture toughness, stress-corrosion resistance, and spalling-corrosion resistance
Mg	β (Al$_8$Mg$_5$)	0.0–4.0 (Mg $\geq$ 0.0)	Reduced welding crack tendency
Mg + C	S (CuMgAl$_2$)	Zn/Mg> 2.2 Cu > Mg	Improved alloy strength
Cu	θ (CuAl$_2$)	$\leq$ 3	Improved corrosion resistance
			Expanded the stable temperature range of the GP zone, and improved the tensile strength, plasticity and fatigue strength
Cr	Incoherent E (Al$_{18}$Cr$_2$Mg$_3$)	$\leq$ 0.35	Nucleation and precipitation of coarse equilibrium phase
	(CrMn)Al$_{12}$; (CrFe)A$_{l7}$	0.1 - 0.2	Fine grain strengthening; inhibits recrystallization nucleation and growth and improves anti-SCC ability.
Mn	Al$_6$Mn	0.2 - 0.4	Improved maximum tensile strength and fracture toughness, the performance of low cycle fatigue, quenching sensitivity
	Al$_{20}$Cu$_2$Mn$_3$	> 0.4	Reduced the number of strengthening phases Zr
Zr	Al$_3$Zr	0.05–0.16	Improved the strength, toughness, ageing effect and corrosion resistance of the alloy
Ag		0.16	Promoted the formation of the GP region and transition phase; delayed the over-ageing of the alloy
Co	(Co, Fe)Al$_9$, Co$_2$Al$_9$	0.05$\leq$ $\geq$0.2	Improved the hardenability; retention of sub-crystalline structure
Ti		0.01 - 0.08	Refined grain, improved casting properties
Er	Al$_3$Er; Al$_8$Cu$_4$Er	0.1 - 0.15	Improved toughness; and hardenability; dimples appear
Sc	Al$_3$Sc	0.1 - 0.4	Grain refinement; recrystallization inhibition.
Sc+Zr	Al$_3$(Sc,Zr)	0.6	Improved anti-SCC ability
Y	Al$_3$Y	0.3	Improved the hardness, tensile strength, elongation
Gd	Al$_3$(Gd,Zr)	0.11	Hindered dislocation; grain boundary movement
Si	Mg$_2$Si; AlFeMnSi	$\geq$0.15	Reduced plasticity and fracture toughness

Fe	Al_6FeMn	≥0.15	Reduced plasticity and fracture toughness

Tan et al. [163] studied the effect of varying percentages of Zn in Al-Zn-Mg-Cu and established a relationship for precipitation using JMatPro. Increase in the Zn content from 4.4 to 7.2 wt.%, the fraction of solid (wt.) of the $MgZn_2$ phase increased from 0.0311 to 0.0551 at RT. If the Zn content is below 5.8 wt.%, the growth rate of the $MgZn_2$ phase rises, but as it goes beyond this limit, it slowly declines. The increase in Zn content also affects T-AlZnMgCu and S-Al_2CuMg phases, at 5.8 and 5.1 wt.%, the fraction amount becomes zero, respectively. Simultaneous, steady content of 2.3 wt.% Mg, the growth rate of precipitates of $MgZn_2$ slowly declines with the rise of Zn content. The content of Zn and Mg, and their ratio, remarkably affect the main $MgZn_2$ strengthening phase. The Mg and Zn elements contribute to the reinforcement of the Al-Zn-Mg-Cu aluminium alloy. With a greater Zn/Mg ratio, the tensile strength of the Al-Zn-Mg-Cu aluminium alloys is increased, but a higher amount of Zn and Mg increases the quench sensitivity of the alloy [164]. As the Mg concentration increased, the T(AlCuMgZn) amount increased from 0 percent to 4.22 percent, with the η($MgZn_2$) concentration initially increasing and then decreasing. As the Mg content increases, the reduction in the crystallization temperature of α-Al and Zn/Mg ratio occurs, so it was reported that a ratio over 2.2 could cause the formation of the T(AlCuMgZn) phase [29]. The amount of T(AlCuMgZn) phase and the crystalline phase volume fraction increased with an increase in Cu content and decreased with a higher Zn/Mg ratio [165].

The effect of different grain refiners/modifiers added Al 7075 is summarized in Table 2.9.

Table 2.9 The researchers reported on details, components, reinforcement, additives, grain refinement, method, and characteristics.

Elements/ Reinforcement/ Additive/ Grain Refiners	Method	Properties	Discussion	Ref
Al-4.5Cu-0.3Mg-0.05Ti+ Zr (0.05wt.%-0.5wt. %)	Die Casting Route (Master alloys Al-5Ti-1B + Al + Mg+ Cu-50Al) remelted for Zr addition	UTS (217-250 MPa)	Coarse Al_3Zr particles are present in the intergranular regions.	[166]
Al7075+Al-2Sc and Al-15Zr	Die Casting Route + Thermo-mechanical treatment	Peak Hardness 195 BHN with 50% Rolling at 100 °C + UTS 611 MPa Peak Hardness 160 BHN	Al_3(Sc, Zr) nano-dispersoids are uniformly distributed throughout the microstructure.	[167]

		with 30% Rolling at 100 °C + UTS 612 MPa		
Al–Zn–Mg–Cu–Sc–Zr+ Er content (0–0.4%)	Die casting Route	0.4% Er - corrosion potential was reduced because of Al8Cu4Er and Al$_3$Er, two phases that enhanced the potential difference between the grain boundary and the matrix.	Er controls the microstructure; the dendrite arms and grain size are refined first, then coarsened and refined again.	[168]
7075-T6+Reinforcement by SiC	vortex casting method + nano, submicron and micron SiC added	Nano (1wt.%) - 682 MPa Sub-micron(2wt.%) - 652 MPa Micron(2wt.%) - 627 MPa	For micron particles, the final tensile strength was improved in specimens with 2 wt. %.	[169]
7075 alloy powder with 1 wt.% Ti submicron particles (0.2 - 2 μm)	Selective laser melting (SLM)	UTS - 291 ± 19 MPa; EL-7.9 ± 2.9%. After T6 - UTS 503; ± 6 MPa; EL - 7.5 ± 1.2%	Inoculation of 7075 by Ti powder produced crack-free, fine-equiaxed microstructure.	[170]
Al7075+Nb	Ingot Casting + Melt spinning	The micro-hardness of 0.5 wt.% Nb- 0.9 GPa. 3 times more than without adding Nb.	Nb addition modified the dimensions and shapes of both the α-Al and intermetallic phases. The average grain size reduced from 9.1 μm to 2.46 μm.	[171]
Al7075+ (WC-Co) (50 μm)	Addition of Cermet 3, 6, and 9 wt. % by Stir Casting	UTS 193 MPa; EL-1.86 for 9 wt.% 108 BHN	Increases the yield stress and tensile strength by 49% and 58% but drastically decreases the percentage elongation by 84%.	[172]
Al7075+6wt.%SiC (~20 μm)	Stir Casting	Wear of 10N, 2 m/s sliding speed, 500 m sliding distance - optimum wear	Wear mechanism by SEM, abrasive wear and ploughing.	[173]
Al7075+Si$_3$N$_4$ (2 to 8) wt.% increase 3%, HfC (0.5 to 2) wt.% increase 0.75% and MoS$_2$ (2 to 5) wt.% increase 1.5 %	Stir Casting	UTS- 209 MPa, EL-24.2 Hardness - 152 VHN, Fatigue stress - @70Kg; 17653 cycles - No failure	Al7075+5wt.% Si3N4+1.25wt.% HfC+3.5wt.% MoS$_2$ shows the optimum result of tensile and fatigue because of the fine grain size.	[174]
Al7075+0.2 Graphene	Die-Cast	refined the grain size of 7075 Al alloys from 78 μm to 45 μm	Graphene can promote heterogeneous nucleation and has little effect on the thermal properties of as-cast 7075.	[175]
Al7075+(0-20 Vol.% SiO$_2$), and foaming agent	Direct Melt Foaming Method	the grain size of α-Al is reduced, forming MgAl$_2$O$_4$, MgO, Al$_2$O$_3$, and Mg$_2$Si	The refining effect of the SiO$_2$ is because of heterogeneous nucleation of the α-Al	[176]

			grain by SiO_2 particles or restriction of the α-Al grain growth.	
$7075+TiB_2$ (3-6 wt. %)	Rheocasting	Before HT - 70BHN After HT - 75BHN Rheocast has a lower Wear rate than die-cast.	The average grain sizes are 23 μm, and the shape factors are 0.96 of rheocast 4.5 wt.% $TiB_2/7075$	[177]
Al7075+Nano TiO_2 (5 and 10wt. %)	Stir Casting	As cast -70 BHN; UTS-212 MPa 5wt.% TiO_2 -78 BHN; UTS-247 MPa 10 wt.% TiO_2 -99 BHN; UTS-298 MPa	The volumetric wear loss of matrix and TiO_2 particles reinforced nanocomposites increased with increasing applied load and speed.	[178]
Al7075+ (0.1 - 0.6 wt. %) Sc (Micro-alloying)	Die-Cast + addition by master alloy +Hot rolling + Solution treatment followed by ageing treatment	1. 0.6 wt.% Sc -128 HV; 2. After homogenization @ 460°C for 10h –Micro-hardness - 98 HV; UTS - 195 MPa; 3. Via hot rolling@400 °C;50% reduction, solution (470°C for 1h and aging treatment 120°C for 24h) - 152HV, UTS - 450 MPa	Sc significantly reduces the grain size from 129.92 μm to 32.17 μm with 0.6% Sc	[179]
Al7075+ (1-4 wt. %) TiB_2	AM (Laser Melting deposition)	Optimum properties of 4wt. % TiB_2 127.8 HV	The grain size decreased by 32 % compared with the unreinforced 7075 Al specimen.	[180]
Al7075+5wt.% nano B_4C + 10 wt.% of Al2O3 and improved by 2,4,6 and 8wt.% of ZrO_2 nanoparticles"	Stir Casting	Al7075 HMMCS + 8wt. % ZrO_2 has less wear resistance.	The wear resistance increased as the weight fraction of ZrO_2 increased within the Al 7075 hybrid nanocomposite.	[181]
Al7075 + (0.5,1.5 & 2.5 wt. % ZrO_2) (50-75 μm)	Stir Casting	2.5 wt.% ZrO_2 Hardness - 122 HV UTS - 131 MPa; EL - 4.7%	The hardness, strength of yield, and tensile strength increased with increasing the weight % of ZrO_2 to 2.5 wt. % while the elongation decreased.	[182]
Al7075+ (3, 6, 9, 12 wt. %) (5-11 μm)	Compocasting process	6 wt. % ZrO_2 Hardness -61.3 BHN UTS - 148 MPa	An enormous increase in the properties was observed up to 6 wt.%, and the improvement was minimal after that.	[183]
Al 7075+X wt.% B_4C+2wt.% Fly-ash (X= 2,4,6,8)	Stir Casting	(Al 7075/2 wt.% FA/8 wt.% B_4C) micro-hardness - 123.29 HV, 37.2% higher than base matrix alloy	Adding B_4C and fly ash increases the micro-hardness of the cast composite.	[117]

AA7075+1 vol %. TiC (molten salt-assisted processing NP)	Stir Casting	Nan-treated TiC AA7075 - 188 HV As-cast AA7075 - T6 - 165 HV	After T6 treatment, an average grain size of 18.5 μm.	[184]

Wang et al. [27] studied the combined effect of Zr and Ti in the as-cast Al-8.4Zn-1.9Mg-0.85Cu-0.15Zr-xTi (in wt%, x = 0, 0.1, 0.2, 0.35, 0.5) alloys, and found that Ti is >0.2 wt.% forms the Al_3Ti and Al_3Zr phases during solidification, illustrated in Figure 2.17. The higher the amount of Ti improved ductility, but there was no significant improvement in strength.
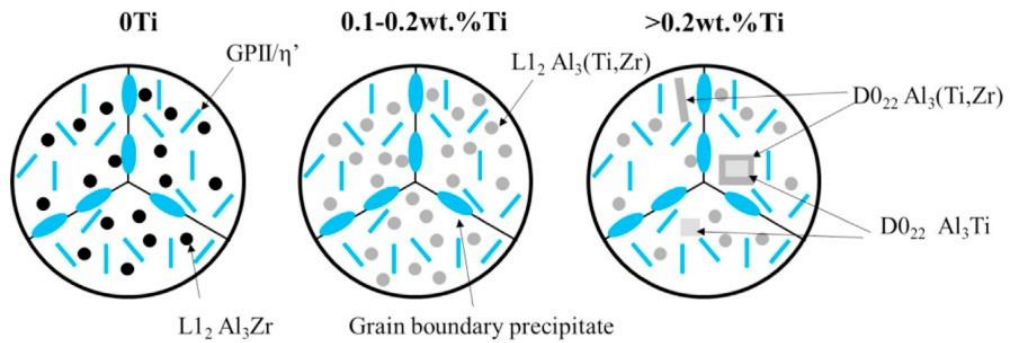
Figure 2.17 Schematic illustration of Ti in Al-xTi and formation of Al₃(Ti, Zr) [27]**.**

Very few studies have mentioned the use of zirconium as a reinforcement in aluminium, and only a small amount of zircon oxide is noted [185]. Kuldeep et al. [186] added h-BN and ZrO_2 as reinforcements and observed the best results of Al 7075/6 wt.% ZrO_2 with 187 MPa tensile strength and 92 BHN hardness. Vijay Kumar et al. [187] fabricated a stir cast Al 7075/xGr+yZrO₂ (x = 0, 3, 2, 1 and y = 0, 1, 2, 3), and got the highest compressive strength in 1% Gr+3% ZrO_2. Rahma et al. [188] studied the varying amount of TiO_2 addition in Al 7075 and found the tensile strength as shown in Figure 2.18.
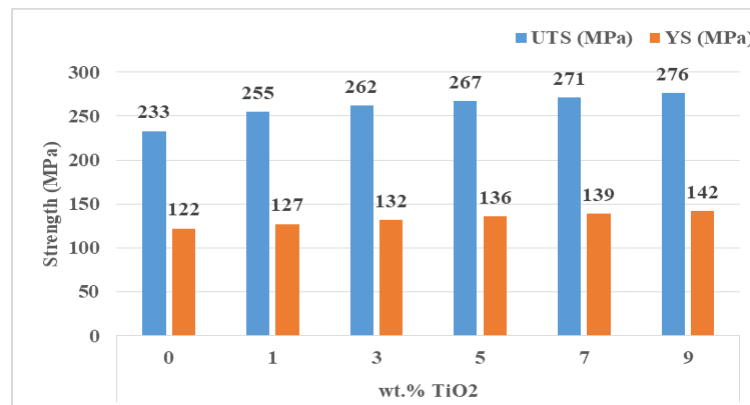
Figure 2.18 Strength of Al 7075/xTiO₂ (x= 0, 1, 3, 5, 7, 9) [188]**.**
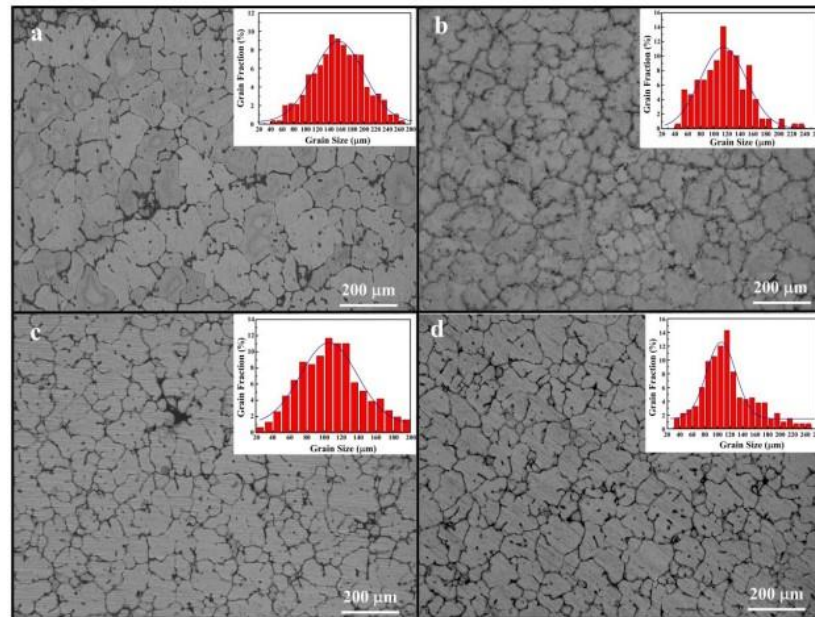
Figure 2.19 Micrographs of as-cast Al 7075/xSr (x = a. 0, b. 0.05, c. 0.1, d. 0.2 wt.%) before T6 treatment [189]**.**

Ma and his co-workers [189] added Sr in Al 7075 and modified the microstructure before and after extrusion, followed by T6 treatment. The microstructural difference before and after Sr modified Al 7075 is illustrated in Figure 2.19 and Figure 2.20, respectively [189].
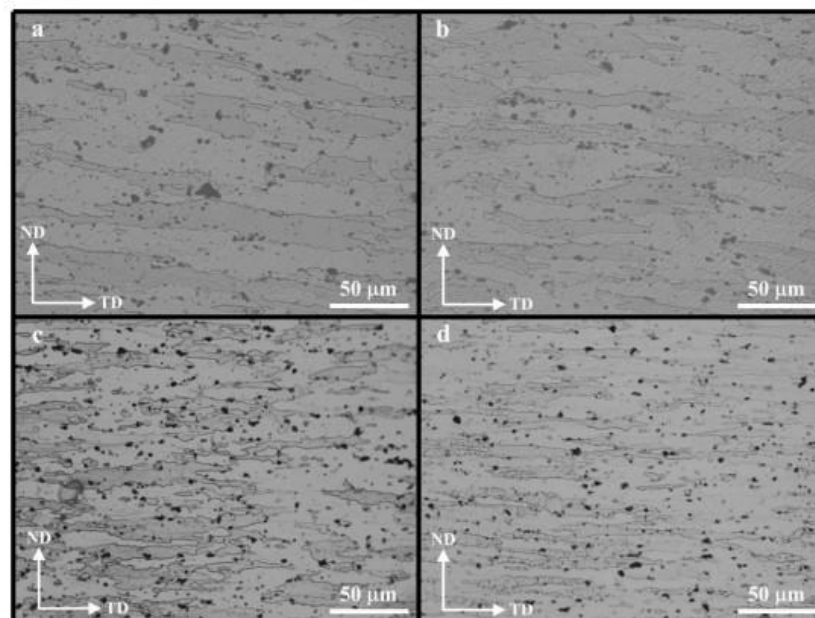
Figure 2.20 Micrographs of homogenized at 460 °C for 6 h, and extruded at 460 °C, followed by T6 treatment [189]**.**

Zhang et al. [190] reviewed Al-Cu-Mg/2 wt.% Zr by selective laser melting (SLM). Zr lowers micro-cracking and improves the mechanical properties of the alloy. Zr being added causes the creation of phases with a lower melting point, which can fill in cracks during the last part of solidification and diminish the probability of cracks. The presence of Al_3Zr particles causes the grains to transition from columnar crystals to ultrafine equiaxed grains. Kai et al. [191] determined that when the Sc content was increased to 0.25%, grain dispersion was improved, particle size was more consistent, and secondary dendrite spacing decreased. When the amount added exceeded 0.30%, no grain refinement occurred, as Figure 2.21 demonstrates.
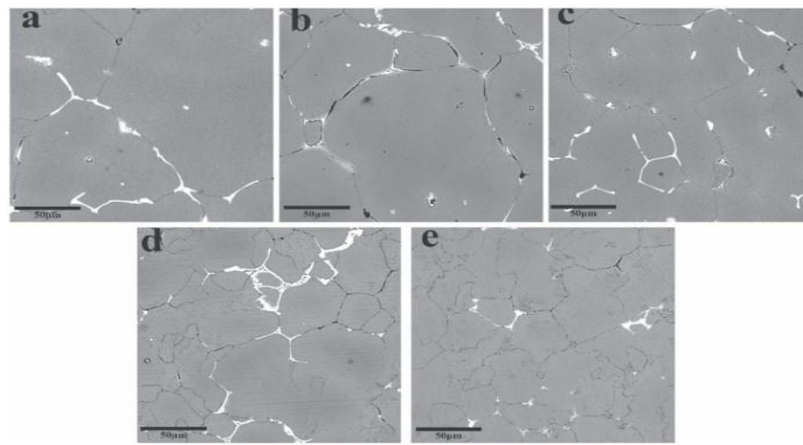
Figure 2.21 SEM images of Al 7055/Y-xSc (x = a. 0, b. 0.2, c. 0.25, d. 0.3, e. 0.35) [191].

Zuo et al. [184] treated Al 7075 by nano-TiC with varying cooling rates, and changed the grain size of the alloy, as shown in Figure 2.22.
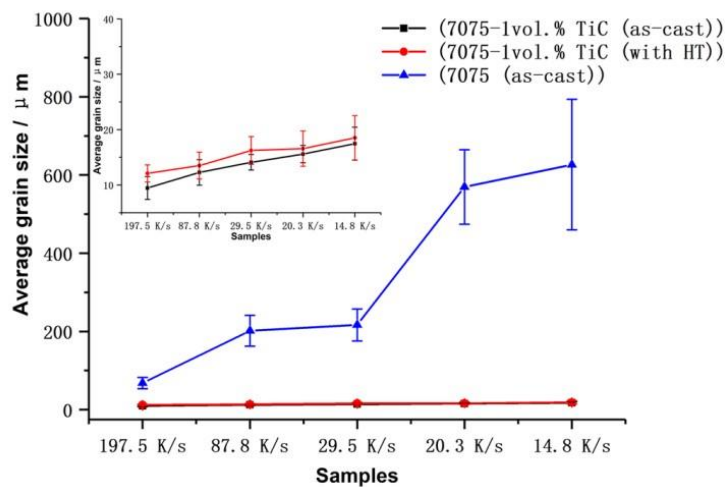
Figure 2.22 Average grain size variation AA7075 before and after nano-treating by TiC [184].

According to the literature review, the tensile strength of Al 7075 in its as-cast form is 88 - 275 MPa. Depending on the varying size of grain refiners/modifiers in Al7075, for micron-size particle additions, tensile strength values range between 132 to 312 MPa, and for nano-size particle additions, it varies between 400 to 590 MPa which is near to wrought 7075 alloys [10, 35, 105, 115, 188, 192–196][197–202].
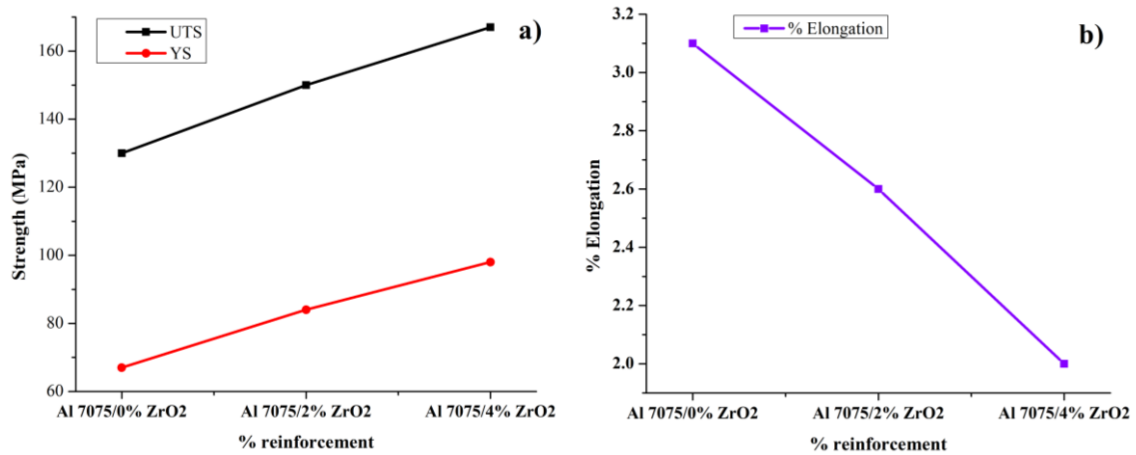
Figure 2.23 Mechanical properties of Al 7075/ZrO₂; a) UTS and YS, b) % Elongation [203].

As shown in Figure 2.23, Prasanna et al. [203] added xZrO$_2$ (x = 0, 2, 4) in Al 7075, and found the 4 wt.% ZrO$_2$ added Al 7075 increased its tensile strength by 28.46 % and its hardness by 15.92 %. Kar et al. [204] added TiC and red mud in Al 7075 and reported mechanical properties before and after heat treatment, as shown in Figure 2.24.
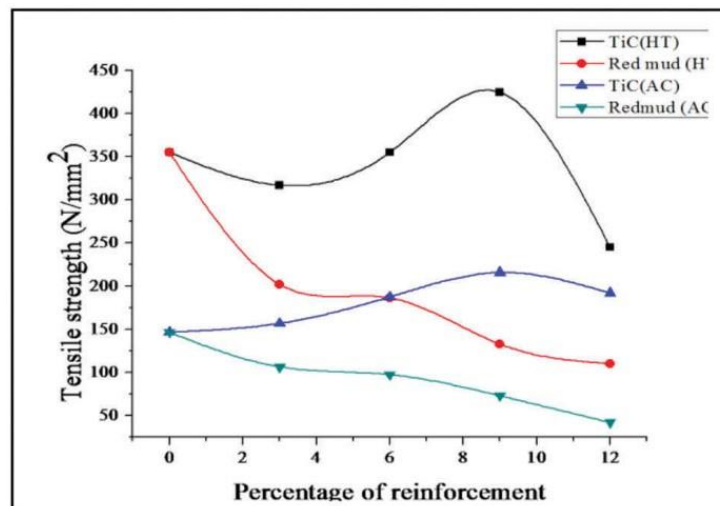
Figure 2.24 Mechanical properties of TiC and red mud added Al 7075 before and after HT [204].

Yang et al. [205] observed that when the addition of Zr (ranging from 0 to 0.30 wt.%) in Al

7075, reduced the grain size and improved the mechanical properties up to 0.20 wt.% Zr, as shown in Figure 2.25 (a) & (b).
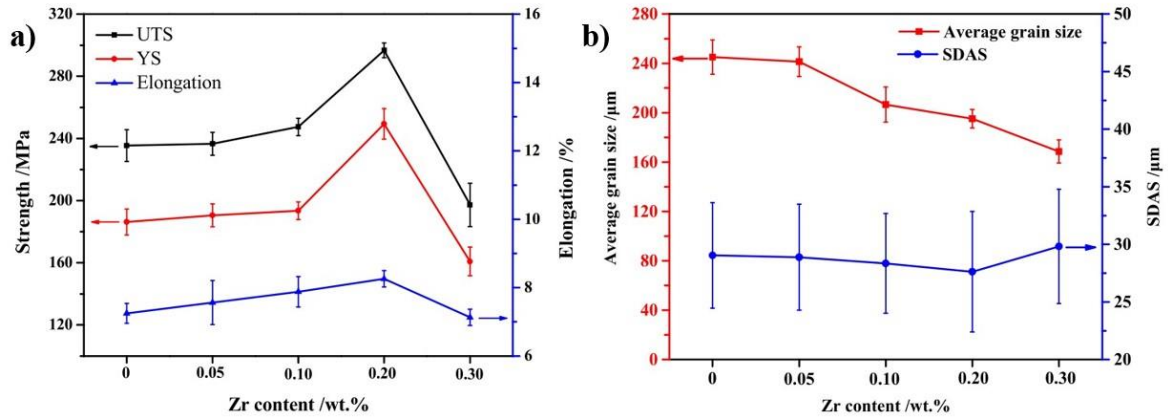
Figure 2.25 Mechanical properties, and grain size relation of Al 7075/Zr (0 − 0.30 wt.%) [205]**.**

Li et al. [206] added nano TiN/Ti in Al-Zn-Mg-Cu (Al-7.0Zn-2.5Mg-2.5Cu), and established the Hall-Petch relationship for tensile strength and hardness value, as shown in Figure 2.26 (a) & (b).
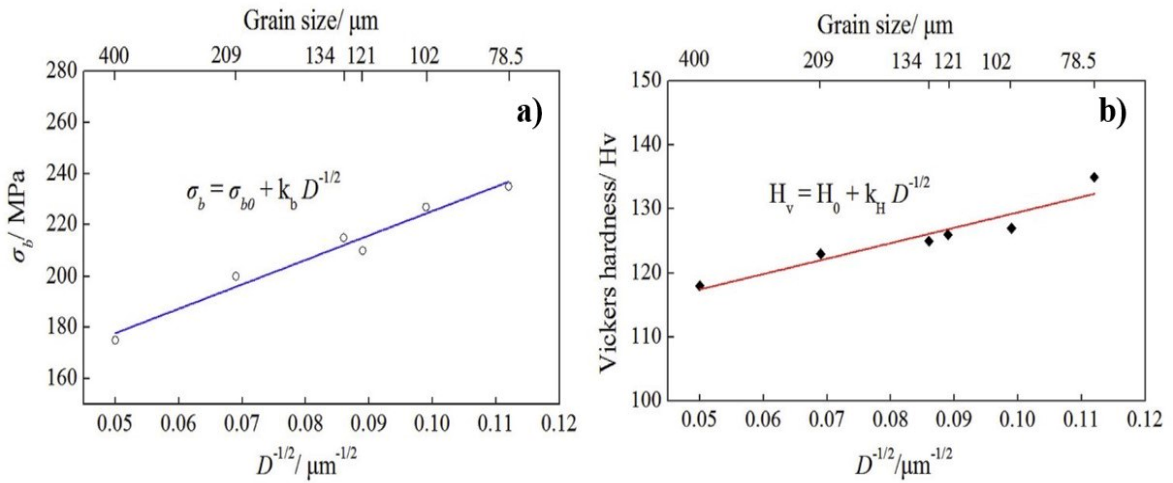

Figure 2.26 Relationship between mechanical properties and grain size by Hall-Petch equation [206].

Ruirui et al. [193] mixed Al_2O_3 nanoparticles in Al 7075 by stir casting, Al 7075/1.5 wt. % Al_2O_3 observed the highest tensile strength of 165 MPa and 112 HB hardness, as shown in Figure 2.27 (a) & (b).
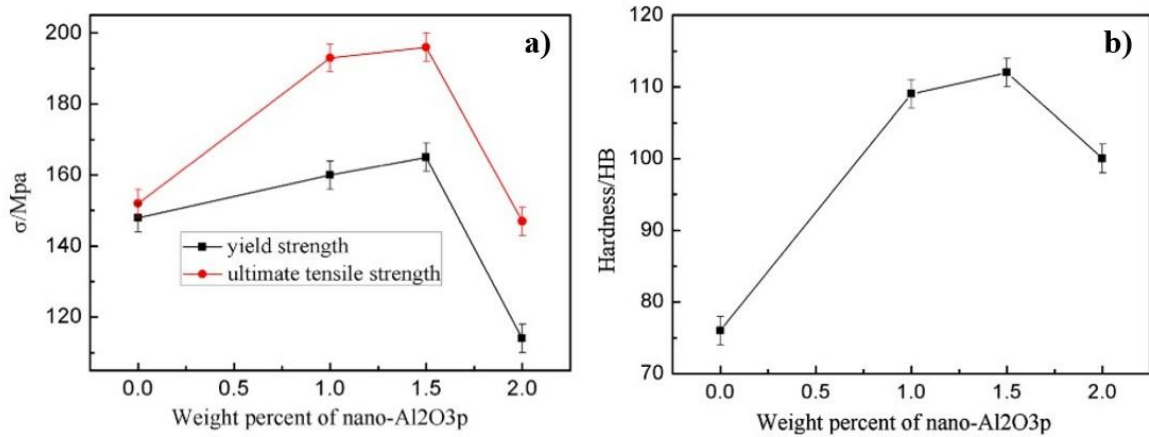
Figure 2.27 Mechanical properties of as-cast Al 7075 and Al₂O₃ nanoparticles added [193]**.**

Park et al. [207] analysed elemental mapping of as-cast Al-7.0Zn-2.5Mg-1.5Cu-0.2Zr (wt.%) by SEM (JSM7900F, JEOL, Tokyo, Japan), and EDS (Oxford Instruments) and examined precipitation analysis, as shown in Figure 2.28 (a) to (d). In Figure 2.28 (a) & (b), Al_7Cu_2Fe and $Al_2(ZnMgCu)_3$ are seen on the dendritic cell boundaries of the gas bubble filtered as-cast (G-A), electromagnetically stirred for the 30s (E 30-A), gas bubbled filtered with T4 treatment (G-T4) and electromagnetically stirred for 30s with T4 treatment (E30-T4) specimens. The atoms of Al-Zn-Mg-Cu alloys segregate at the boundaries of dendritic cells during solidification, and form Zn-, Mg- and Cu-rich phases. The solubility of Cu is extended in the Zn-Mg-rich intermetallic phase, often referred to as the $Al_2(ZnMg)_3$—T phase, resulting in a composition of $Al_2(ZnMgCu)_3$ [208].
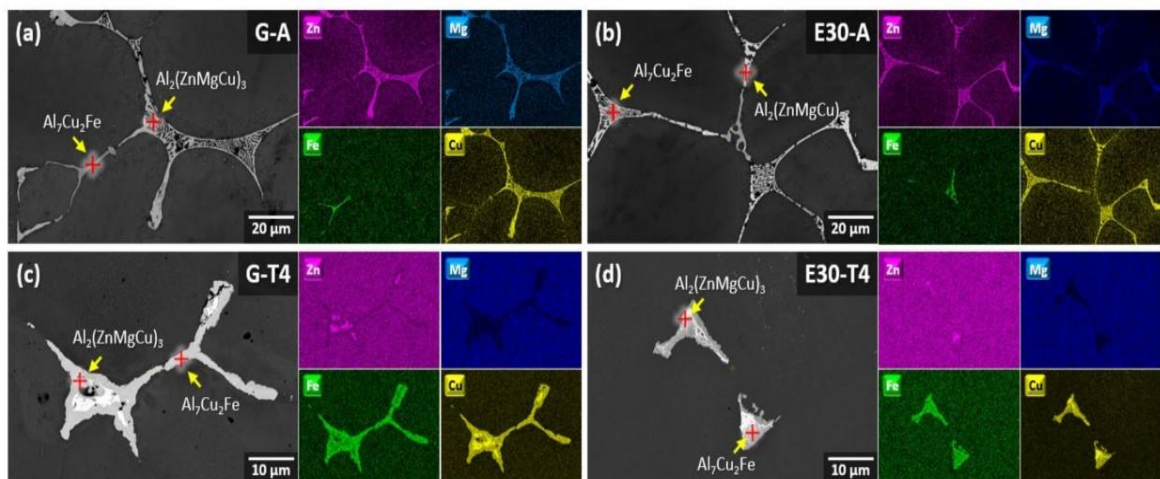
Figure 2.28 Analysis of the precipitation in Al-Zn-Mg-Cu alloys after casting and heat-treating using BSE micrographs and EDS elemental mapping. (a) G-A, (b) E30-A, (c) G-T4 and (d) E30-T4 specimens exhibited Al_7Cu_2Fe and $Al_2(ZnMgCu)_3$ phases [207]**.**

In conclusion, during the solidification of 7xxx aluminium alloys, grain refiners/modifiers, micro-alloying elements, or elements addition create heterogeneous nucleation sites, causing morphological changes in the microstructure. The heat treatment process or other thermo-mechanical processes can improve the grain boundary precipitates distribution inside the matrix, which enhances the mechanical properties.

2.4   Solidification of the 7XXX aluminium alloys

Casting is a very common and widely used material processing technique that involves placing the material in a mold and allowing it to solidify. To start the casting process, the material should be in a liquid state with a temperature beyond its melting point. The system is changed when the temperature decreases, and this allows crystallization to happen. With different casting conditions and fundamental properties of the system, the solid phase will begin to nucleate and grow into many types of structures [209]. Solidification begins with the appearance of nuclei, and when the cluster of atoms come together during random motion in the melt, termed embryonic crystals, that permit further sitting of atoms on their surfaces, which causes the solid phase growth [37]. During solidification or crystallization of alloys, the phase changes from liquid to solid depending on Gibbs' free energy of the system thermodynamically [210]. The substantial supercooling is the primary driving force to form nuclei in homogeneous nucleation, and the resultant microstructure depends on the degree of supercooling, as shown in Figure 2.29. It is well known that nucleation and growth are fundamental to understanding the solidification of alloys. The solidification of alloys is solidified over a range depending on alloying elements, thermal gradient, and the degree of undercooling. The addition of (cold) oxides (foreign particles), impurities, or even the mould wall provides a heterogeneous nucleation site that controls the final microstructure. It is known that heterogeneous nucleation requires less activation energy than homogeneous nucleation. Solidification of cast Al 7075 studies can contribute to understanding emerging processing like selective laser melting, additive manufacturing, 3D printing technology and many more. The heterogeneous nucleation needs a preferential site for nuclei rather than relying on supercooling [63, 211, 212].
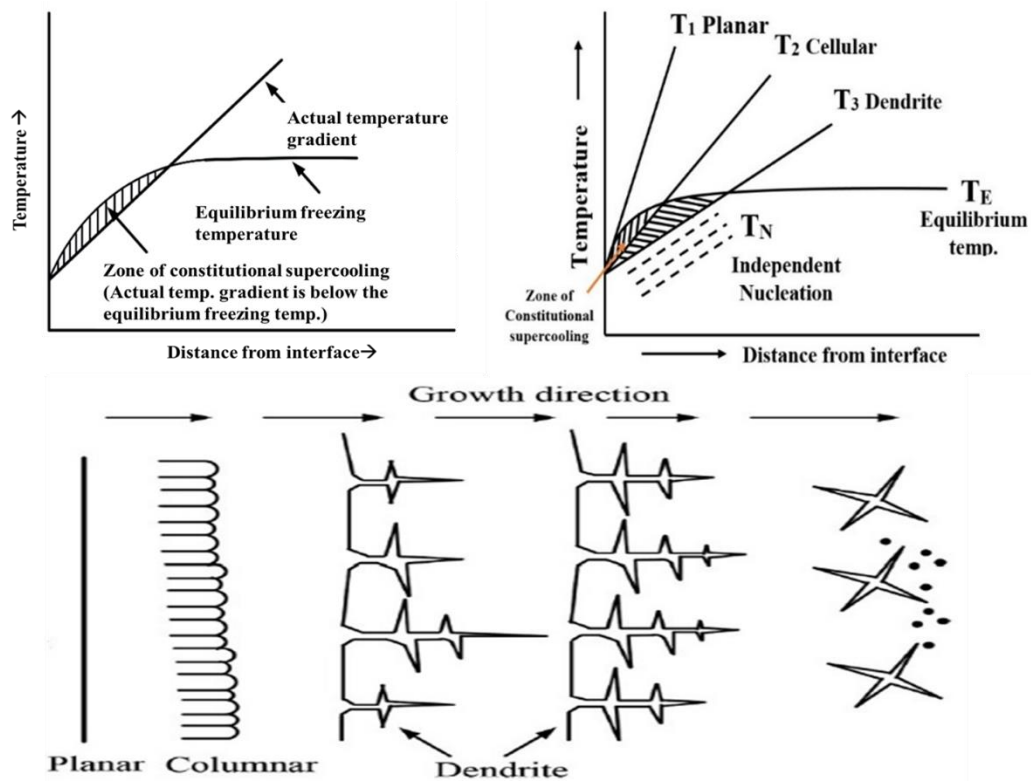
Figure 2.29 Schematic presentation of constitutional supercooling effect on grain growth morphology [37].

Because of supercooling, the defects may result from melt flow, solid transport, feeding, microstructure evolution, strength improvement in the mushy zone, solidification shrinkage, and thermal contraction [213]. Common casting defects are hot tearing, porosity, macro-segregation, and distortion of geometry, which mainly arise because of solidification shrinkage, and thermal contraction. Figure 2.30 illustrates the common casting defect in the casting of alloys [214, 215]. The 7xxx aluminium alloys are prone to hot tearing and micro-segregation because of a wider solidification range. The aluminium alloys like 2xxx, 6xxx, and 7xxx have an enormous difference between liquidus and solidus temperature [216]. In solidification, when the initial solid is created and the liquid-to-solid shift continues, the heat of fusion created by the transformation needs to be taken away or dissipated, as shown in Figure 2.31 (a) [217]. This usually takes place by conduction through the solid, away from the area of solidification. For an alloy to solidify, solute must be redistributed between the liquid and solid, since the composition of the liquid and solid at the solidification front changes constantly as the temperature decreases within the solidification range, as shown in Figure 2.31 (b) [218].
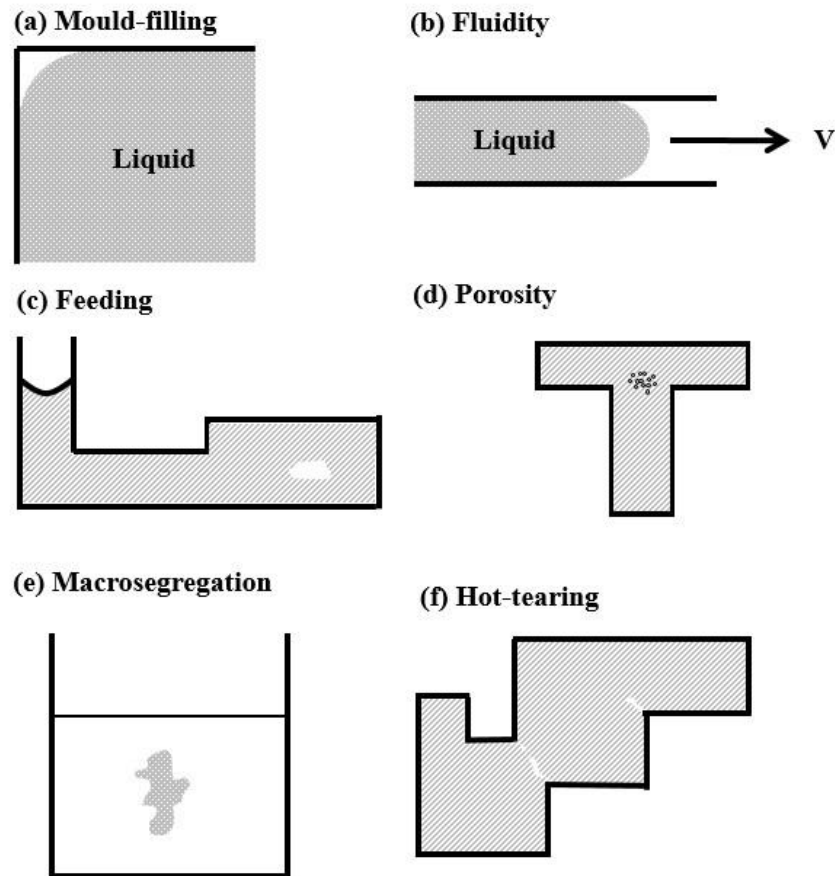
(a) Mould-filling

Liquid

(b) Fluidity

Liquid → V

(c) Feeding

(d) Porosity

(e) Macrosegregation

(f) Hot-tearing

Figure 2.30 Common casting defect arises because of metal flow, feeding, solidification shrinkage, and thermal contraction [214, 215].
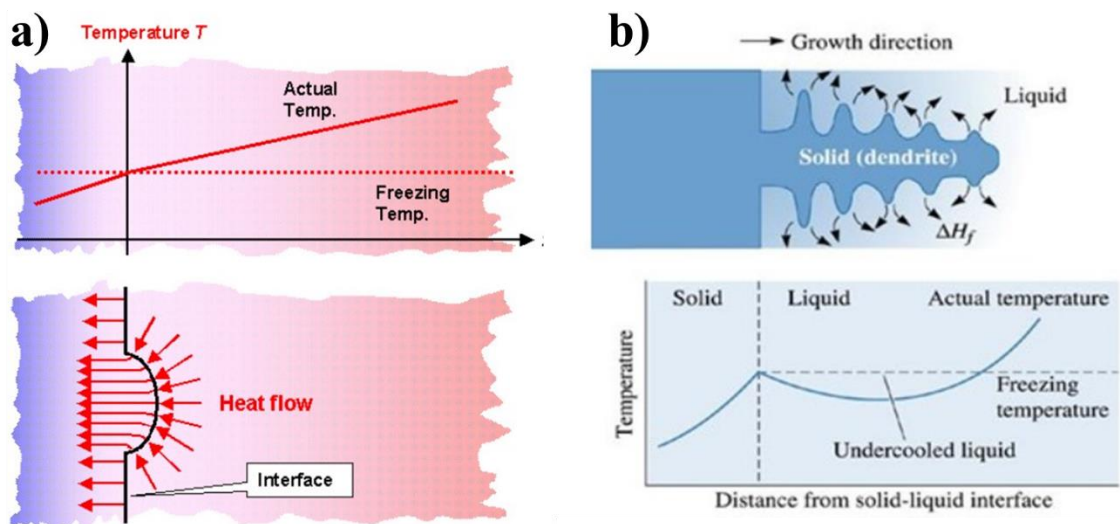

a) Temperature T

Actual Temp.

Freezing Temp.

Heat flow

Interface

b) → Growth direction

Liquid

Solid (dendrite)

ΔH_f

Solid | Liquid | Actual temperature

Temperature

Freezing temperature

Undercooled liquid

Distance from solid-liquid interface

Figure 2.31 Heat dissipation during liquid-to-solid transformation opposite to the S/L interface front (a), and solute redistribution at the S/L interface due to localised supercooling [217, 219] **(b).**

Geng et al. and his team have researched the solidification behaviour of Al- 4 wt.% Cu and Al- 4 wt.% Mg and observed that segregation is created between primary dendrites and creates a smooth liquid channel in Al-4Cu, while segregation occurs not only in the primary dendrites but also between secondary dendrites in Al-4Mg, shown in Figure 2.32 (a) to (d) [220].
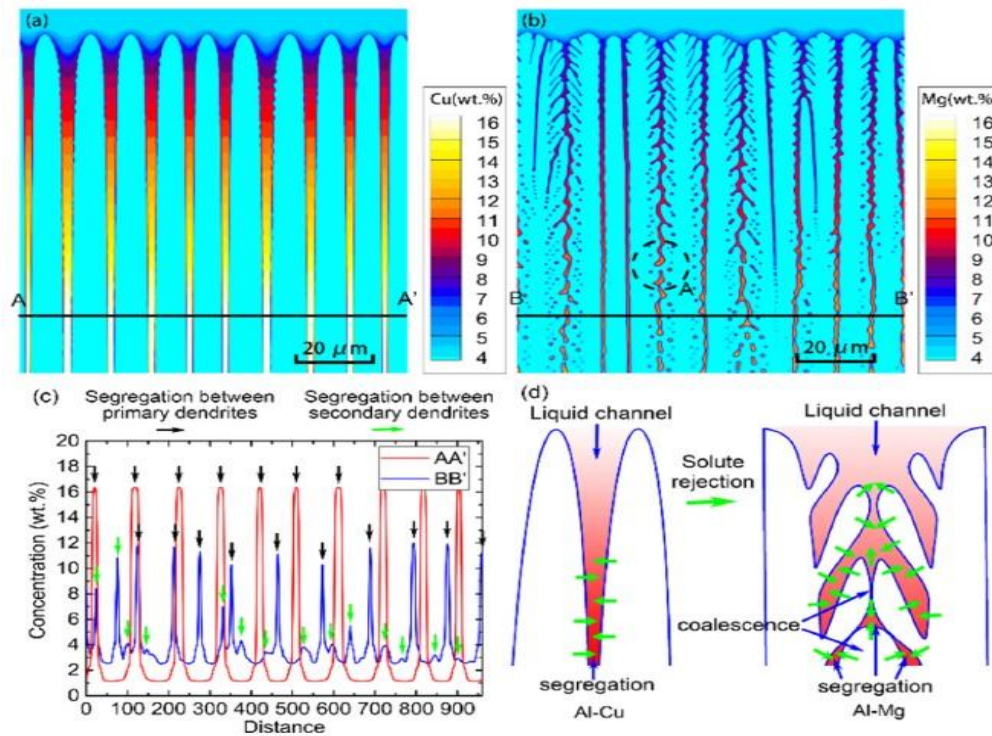
Figure 2.32 Solute distribution within liquid channels in columnar growth of (a) Al-4 wt.% Cu alloy and (b) Al-4 wt.% Mg alloy; (c) solute distribution along line AA′ and BB′; Black arrows show segregation between primary dendrites, while green arrows show segregation between secondary dendrites; (d) Schematic of the segregation and dendrite coalescence for Al-Cu and Al-Mg alloys [220].

The chemical partitioning coefficient changes according to the difference in chemical concentration of the two regions in the phase diagram, and it differs in grain and grain boundaries structure-property relationship. Segregation of certain solutes to the grain boundaries is driven by the Gibbs adsorption isotherm, resulting in a difference in chemical composition between the grain boundary and the bulk. As a result, equilibrium segregation phenomena are a major factor in transporting and changing phases [221]. The redistribution of the solute depends on the phase diagram, diffusion, undercooling, fluid flow, and so on. The redistribution of solute during solidification essentially depends on the distribution or

partition coefficient, k. The equilibrium coefficient $(k_E = C_S/C_L)$ depends on the characteristics of the system, while the effective distribution coefficient $(k_E = C_S/C_0)$ depends on the condition under which solidification takes place. As shown in Figure 2.33 (a) & (b), the solute and solvent rejection depend on the equilibrium partition coefficient k, where k<1 and k>1, respectively [218].
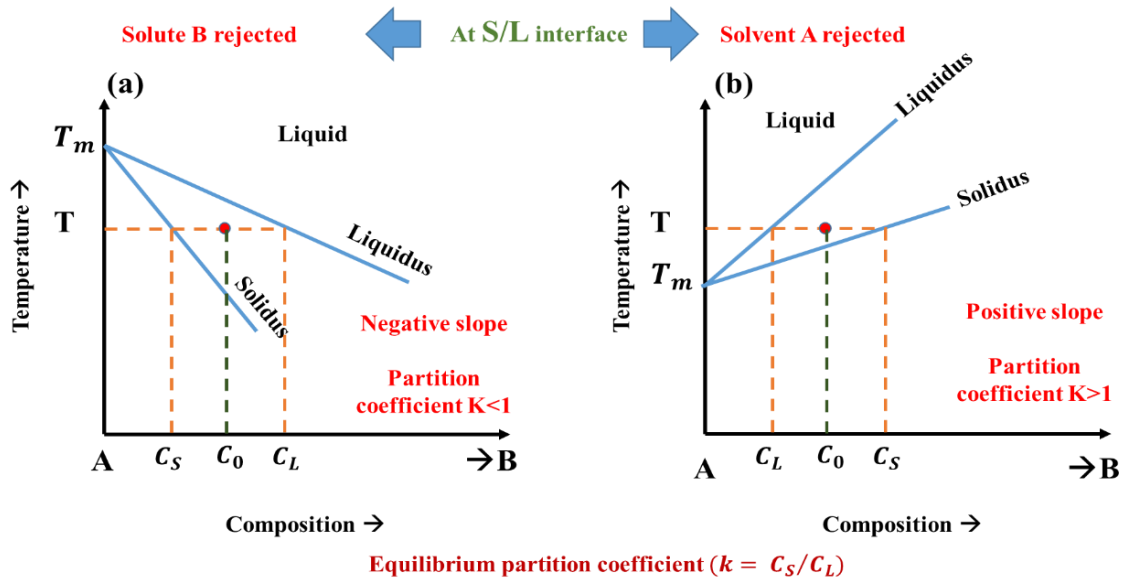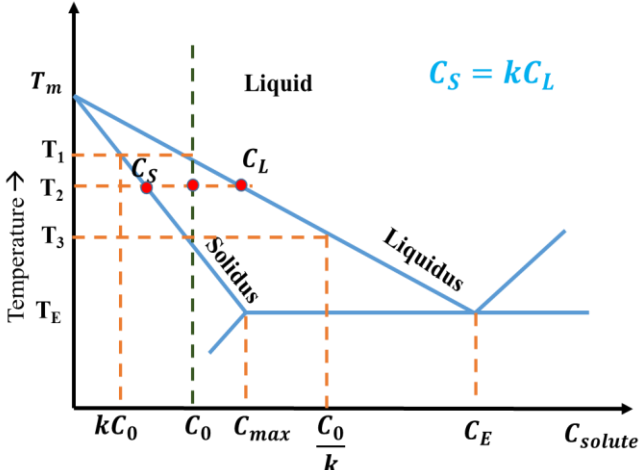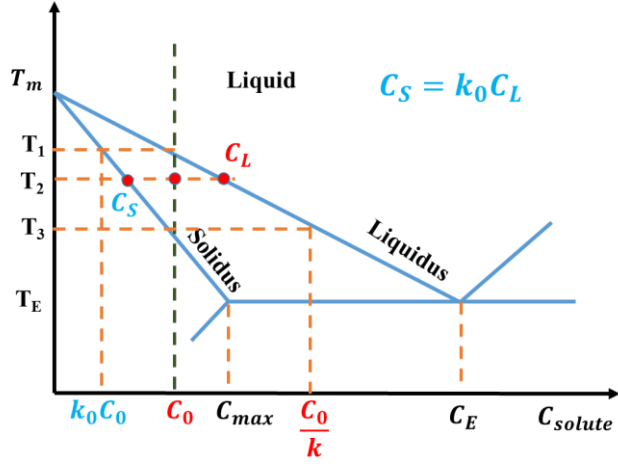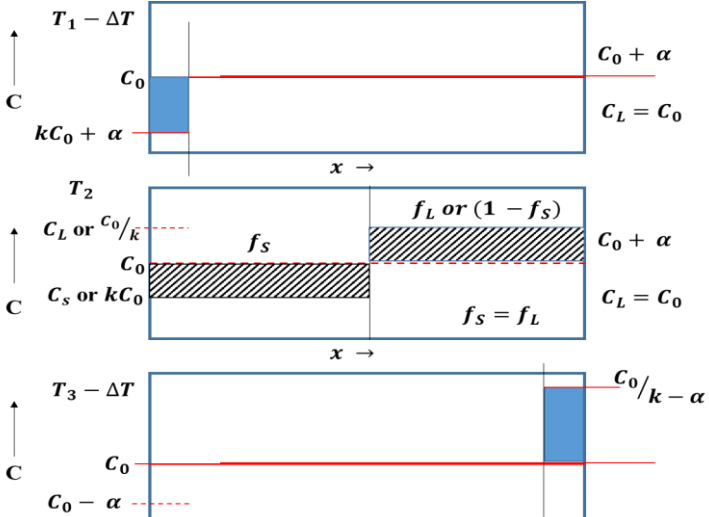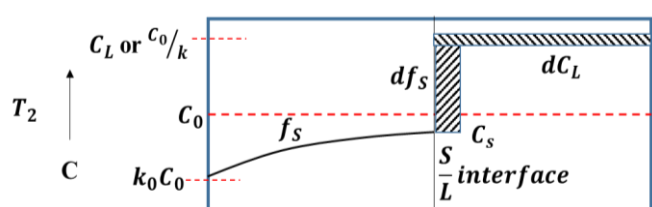

Figure 2.33 Rejection of solute and solvent according to the equilibrium partition coeff, k.

Further understanding of the solute redistribution with the help of the partitioning coefficient, diffusion, and phase diagram is shown in Figure 2.34. The perfect mixing of liquid and solid is in case-I, with equal parts of each, and that allows for the conservation of solute. In comparison, Case-II has a perfect mixture in liquid but no diffusion in solid, leading to an unequal distribution which attempts to achieve the original compositions, thus producing a non-equilibrium lever rule (coring structure) [222]. Non-equilibrium cooling during alloy solidification of casting can cause coring, so an ageing or homogenization treatment is carried out to get rid of the segregation and homogenize the solute distribution [223].

Case–I Complete diffusion in solid and liquid (Equilibrium solidification)	Case–II Complete liquid diffusion but no solid diffusion
Where, D_L & D_S is the diffusion of the solute in the liquid, and solid, respectively and l = Initial length of liquid channel.	

$C_S = kC_L$

Complete diffusion in solid: $D_S\, t \gg l^2$; and **complete diffusion in liquid**: $D_L\, t \gg l^2$

$C_S = k_0 C_L$

No diffusion in solid: $D_S \ll l^2$; and **complete diffusion in liquid**: $D_L\, t \gg l^2$

$$f_L = \left(\frac{C_L}{C_0}\right)^{1/k-1}$$

or

$$f_L = \left(\frac{C_0}{C_L}\right)^{1/1-k}$$

So, in case I:
composition of liquid at T_2: $C_L = C_0/f_L + k(1 - f_L)$
Depending on the value of k.
And, in case II:
$$So, C_S = kC_0(1 - f_S)^{k-1} \text{ and } C_L = C_0(f_L)^{k-1}$$
$$known\ as\ Scheil\ equation\ to\ represent\ solute$$
$$distribution\ ^{[210]}.$$

Case–III Incomplete diffusion in liquid and no diffusion in solid

The convection is assumed to be negligible. Neither S nor L is of uniform composition. Solid rejected (k < 1), and pile up and form a solute-rich boundary ahead of the growth front. So, equilibrium only exists at the (S/L) interface because of limited liquid diffusion and no diffusion in solids. Here, the interface has a solute segregation.

$$C_S = k_0 C_L$$

$$\frac{C_L - C_0}{\frac{C_0}{k} - C_0} = e^{-\left(R/D_L\right)z}$$
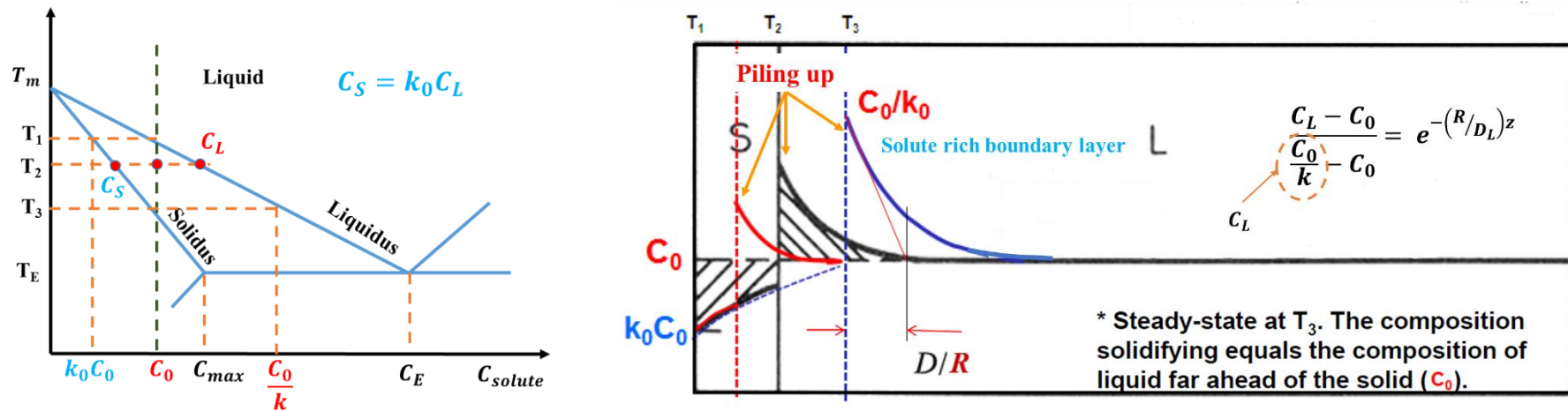
Where R = growth rate (cm/sec), z = distance from the S/L interface (If Z=0, then $C_L - C_0$ has the maximum value.)

Figure 2.34 Solute redistribution phenomena Case–I complete diffusion in solid and liquid, Case–II Complete liquid diffusion but no solid diffusion, and Case–III Incomplete diffusion in liquid and no diffusion in solid (more severity of segregation in this case) [209, 210, 218, 221, 223–226].

In case–III in contrast to case–I, incomplete diffusion in liquid, and no diffusion in solid, where the solute and solvent not moving while equilibrium solidification will be reached. Thus, the liquid is sufficiently cooled locally, allowing for a process of solidification without diffusion. Further, in this case, there are three variations (a) the S/L profile varies when the temperature is between T2 and T3, (b) the temperature T3 showed a steady-state. The solidification of the composition is equal to the liquid composition far before the solid (C_0), and (c) revealing the final transient in the composition profile at T_E and below, as shown in Figure 2.35.
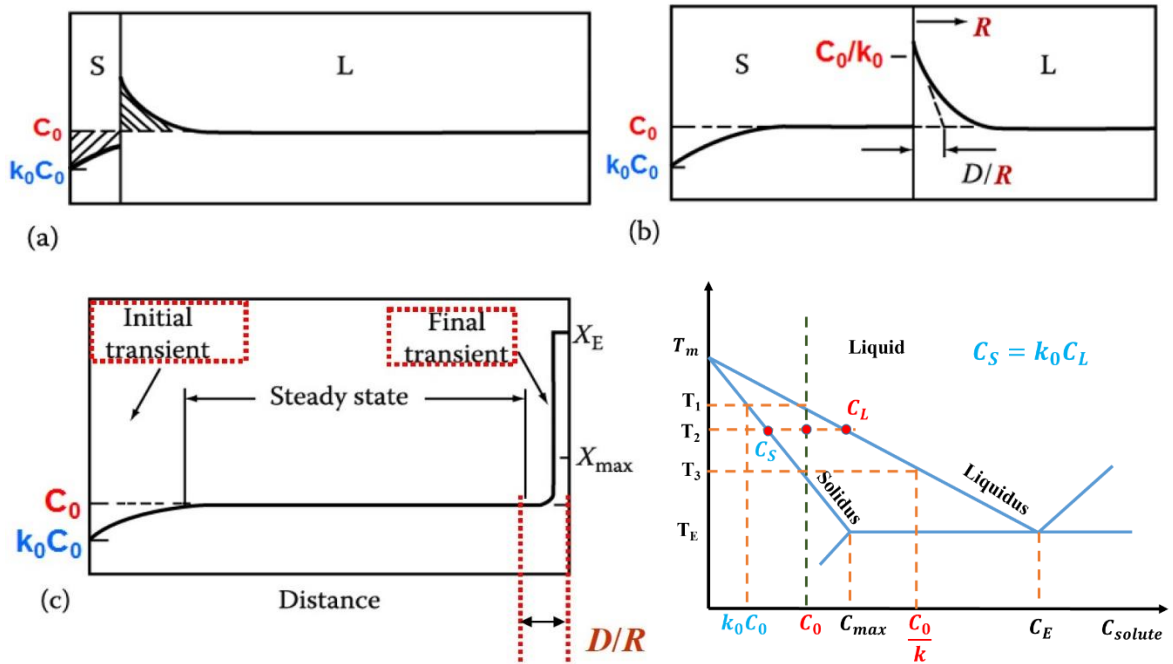
Figure 2.35 Solute concentration profile of no diffusion in solid and diffusional mixing in liquid (case-III) (a) initial transient, (b) steady state, and (c) terminal transient.

In case-II, by application of the Scheil equation, it tries to maintain equilibrium chemical composition ahead of the S/L interface, and experiences coring structure will form separate layers of solids as eutectic, as shown in Figure 2.36 [227].
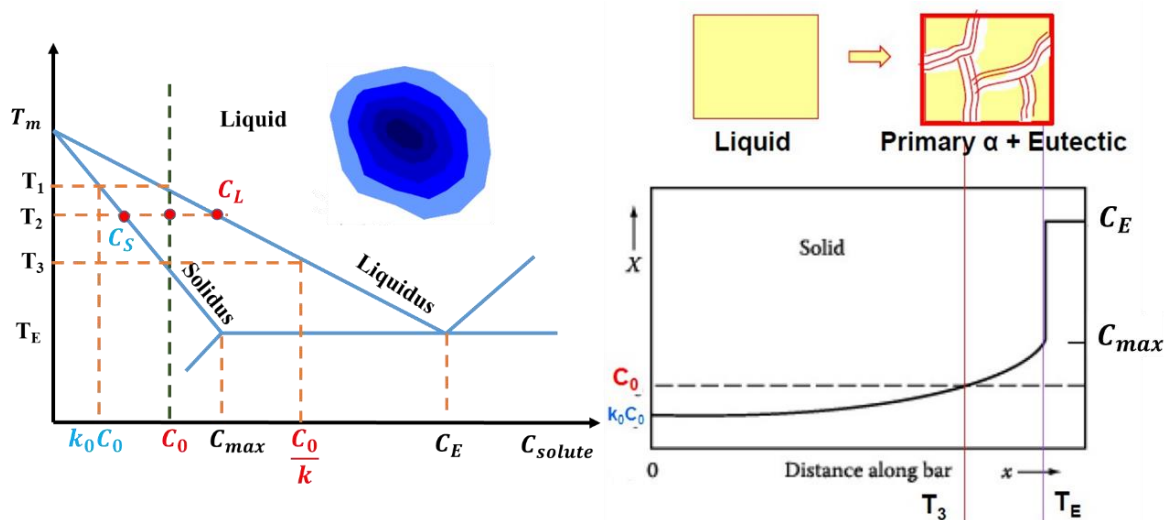

Figure 2.36 Solute concentration profile for the coring structure of eutectic [227].

Kohn et al. experimented with the concentration of copper before the S/L interface in quenched Al-Cu alloy by electron microprobe, as shown in Figure 2.37 [228]. The segregation

of solute in Al-Cu alloy is also illustrated in Figure 2.32 (d).
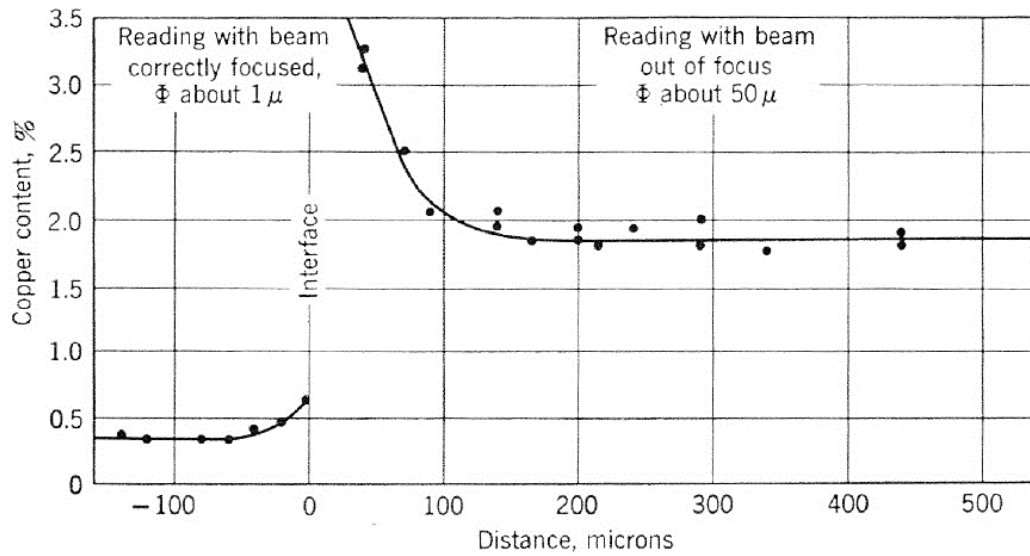
Figure 2.37 Copper concentration in quench Al-Cu alloy during solidification [228].

In the summarizing above theories and discussion, the redistribution of solute is more severe in case–II and case–III. From the diffusion point of view, the segregation is more severe because of chemical heterogeneity over the S/L interface front. The result of no diffusion in solid increases the solute concentration ahead of the S/L interface and pile-up the concentration, hence, all possible diffusion occurs at the interface. The most chances of segregation arise in the coring, cellular, and dendritic structures. The control of microstructure can be achieved by applying heat treatment or homogenization treatment.

As describing microsegregation, there are normal segregation, grain boundary segregation, cellular segregation, dendritic segregation, inverse segregation, coring and intercrystalline segregation, and gravity segregation [210, 229]. So, to understand the segregation problem, other aspects need to be explored, like constitution supercooling for dendritic structure, and cellular structure growth [230]. To get the non-dendritic structure and reduce the microsegregation, the modification of microstructure during solidification can be possible by the addition of modifiers or inoculants, and grain refiners to create heterogeneous nucleation sites and inhibit the recrystallization which acts as a nucleation catalyst. The modification theories more likely depend on nucleation and growth and the combination of them, and it is illustrated in Figure 2.38 [223].
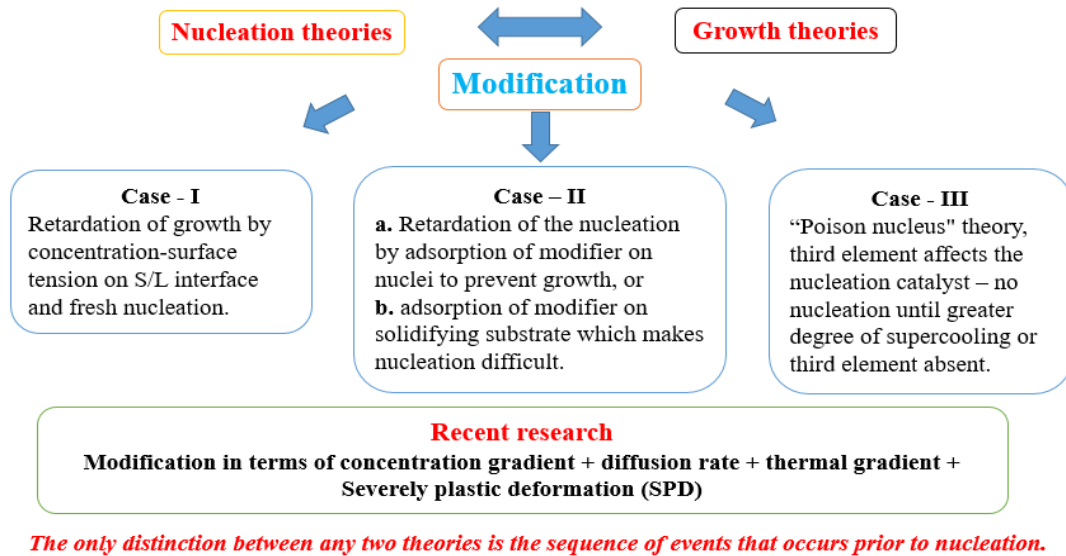
Figure 2.38 Modification of microstructure by nucleation and growth theories Thall et al. [231] investigated case-I, Plumb et al. [232] investigated case-II, and Tiller [233] investigated case-III.

2.4.1 Development of cellular and dendritic structure and constitutional solidification

During solidification of alloy, the solidification mode or a phenomenon known as constitutional supercooling can be planar, cellular or dendritic depending upon the solidification condition and materials system involved [234]. It is well-known that in pure metals, the development of structure mainly depends on thermal supercooling or undercooling. But, in alloy solidification, supercooling may be developed by a negative thermal gradient or by constitutional supercooling with a positive thermal gradient. It is known that the solidification of the alloy in front of the S/L interface produces a solute concentration. As the initial nuclei form during alloy solidification, the solute that is being rejected is sent to the liquid and collects near the S/L interface because of the different diffusion rates of the solute in both phases [209, 223].

The four different S/L interface morphologies, as seen in Figure 2.39, are planar, cellular, columnar and dendritic. The morphological progression resulting from an initially planar interface becoming unstable, as shown in Figure 2.40 (a) to (d) [234]. The initial evolution of the unstable and stable S/L interface is shown in Figure 2.41 [218]. In diluted alloys, the crystallization rate is slow comparatively. Initially, planar S/L boundary can produce cells, and they will remain stable. These cells have deep trailed grooves that create strong lateral solute rejection [229].
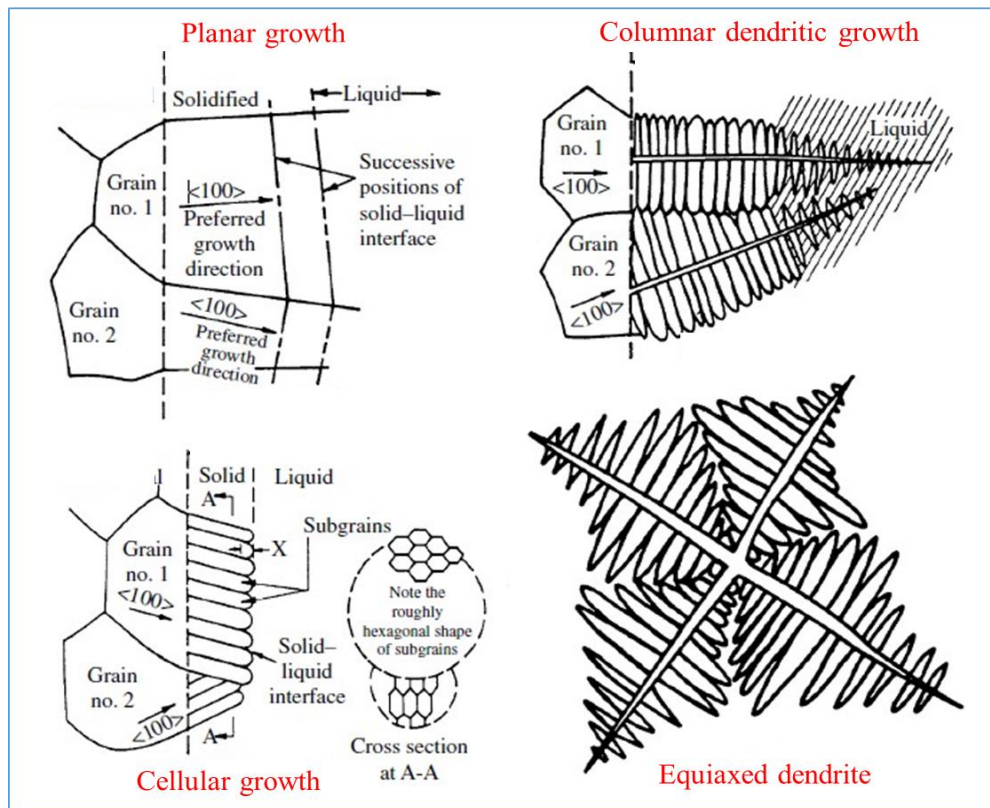
Figure 2.39 Schematics showing the microstructure of solid-liquid interface modes of solidification [235]**.**
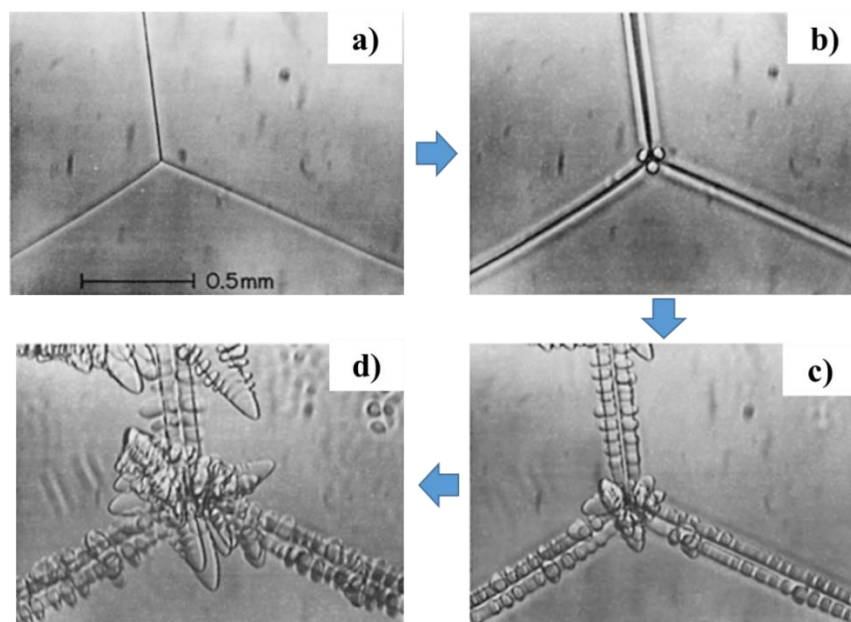

Figure 2.40 Grain boundary triple lines affecting the interface stability of the S/L interface in sequence [234]**.**
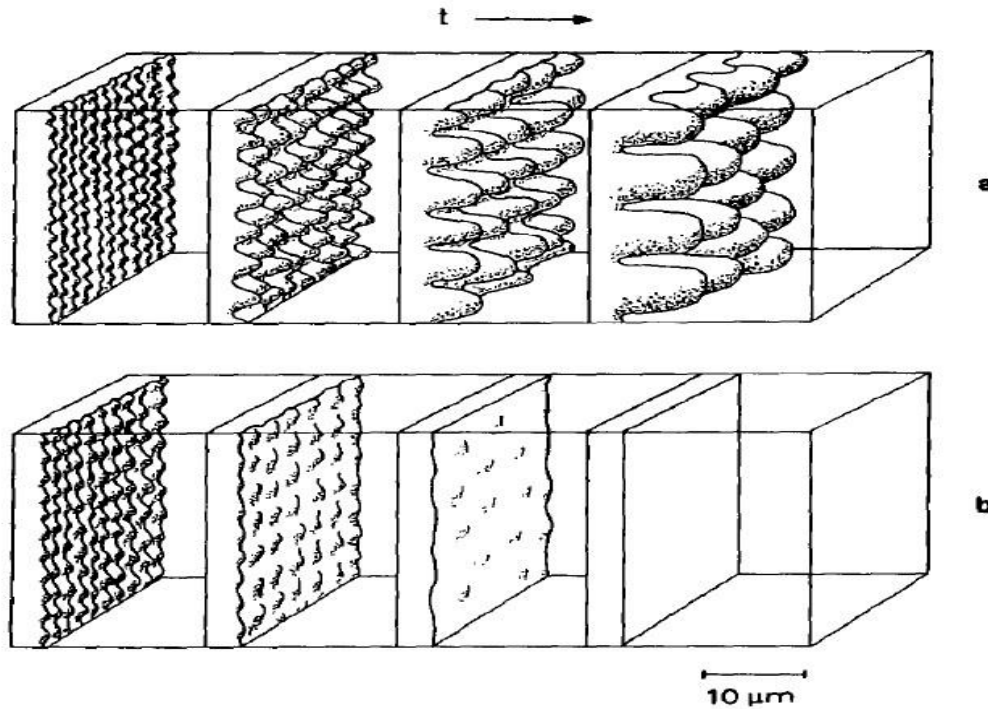
Figure 2.41 Initial evolution of a) unstable, and b) stable S/L interface [218].

Also, higher solute diffusion has a similar latent heat of conduction in pure metal, which can make it possible to breakdown the planar front into dendrites. Conventionally, a slow solidification process like casting, with its solidification front moving at a much slower rate (order of μm/s) compared to the interface diffusion rate V_D (0.1–1 m/s), allows for complete solute redistribution, and the interface can come to a local equilibrium concentration following the phase diagram. Hence, the liquidus temperature varies with respect to the solute concentration at the interface to establish thermal equilibrium. So, it must satisfy the thermal parameter by the equation $\frac{G}{R} = \frac{\Delta T_f}{D_L}$; where G = temperature gradient, R = interface growth rate, ΔT_f = freezing range, and D_L = diffusion coefficient in liquid [236]. Chen et al. studied dynamic S/L interface during solidification of Al7075/np-Al$_2$O$_3$ and investigated from a model that the velocities determined for the interface were four times lower than the velocities measured for micron particles, which implies that smaller particles are more likely to be engulfed by the interface than pushed away. Hence, the constitutional super-cooling of local melts and the gathering of solutes were responsible for the formation of a cellular interface [237]. The proposed theory of constitutional supercooling by Tiller et al. [238] is of breaking of the S/L interface during solidification, and also Muller et al. [239] proposed interfacial stability theory. To avoid the constitutional supercooling, the condition which will

46

be satisfied is: $\frac{G}{R} \geq \frac{\Delta T_f}{D_L}$, and if $\frac{G}{R} < \frac{\Delta T_f}{D_L}$, then it experiences constitutional supercooling, as shown in Figure 2.42. Depending upon the slope of the tangent line, breaking of planar interface, and higher degree of supercooling are the base to change the structural morphology, as shown in Figure 2.43.
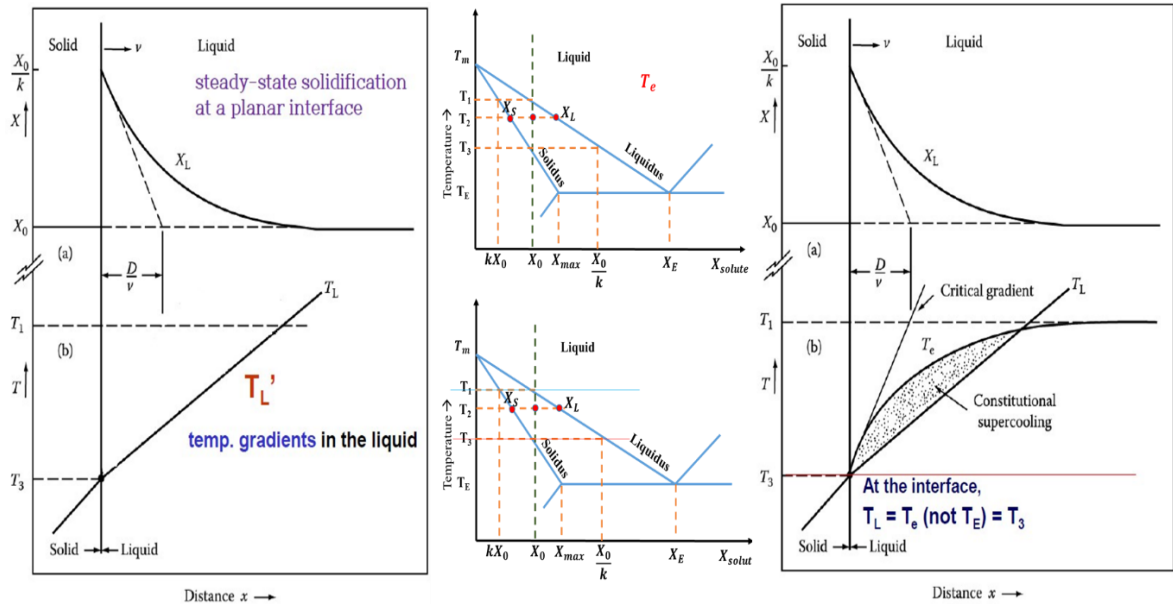

Figure 2.42 According to the solute profile of no diffusion in solid, segregation piles up between X_0 to $\frac{X_0}{k}$ experiencing constitutional supercooling [218, 230, 234].
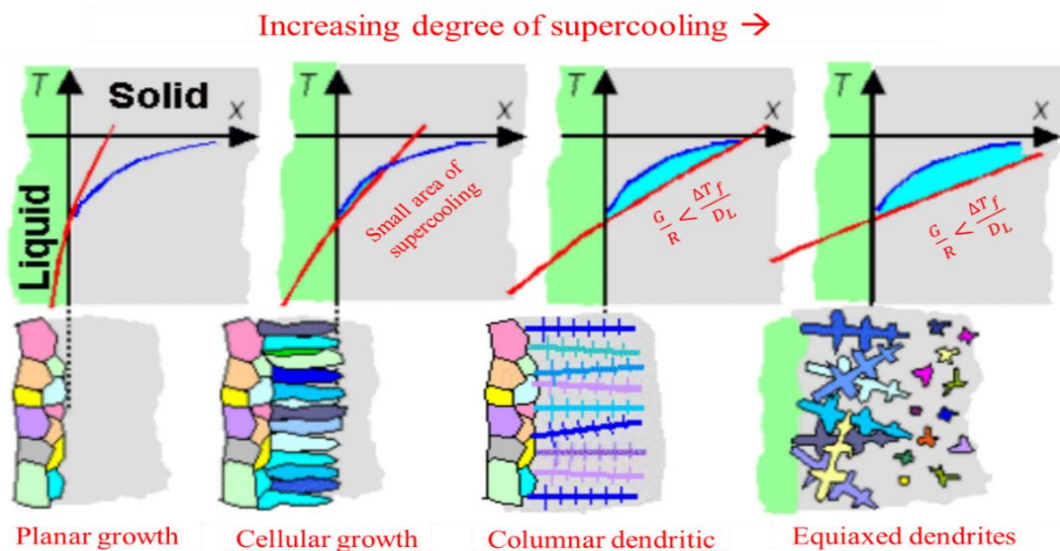
Figure 2.43 Depending on the slope of the critical gradient, the growth of unique structure because of constitutional supercooling [217].

Hence, solute redistribution point of view, cell formation can be suppressed by the reduction in solute content, and growth speed, and also by increasing the temperature gradient (T_L'), $\frac{G}{R} \geq \frac{\Delta T_f}{D_L}$. The formation of structural morphologies like cellular, columnar dendritic, and equiaxed dendrite arises when the temperature gradient at the interface is reduced below the critical gradient, and experiencing constitutional supercooling, as shown in Figure 2.44 [218, 240, 241].
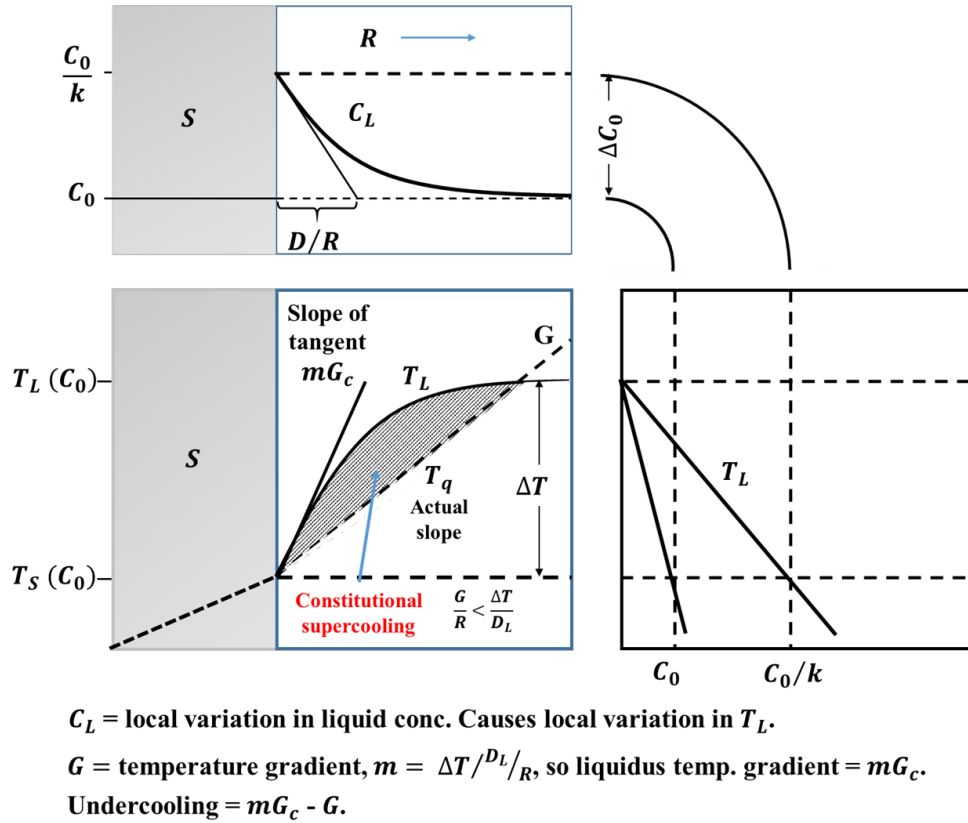

C_L = local variation in liquid conc. Causes local variation in T_L.

G = temperature gradient, $m = \frac{\Delta T / D_L}{R}$, so liquidus temp. gradient = mG_c.

Undercooling = mG_c - G.

Figure 2.44 Illustration of constitutional supercooling responsible for cellular, columnar dendrite, and equiaxed dendritic structure [218].

The large solidification range (ΔT) and higher growth rate (R), promote perturbation, as shown in Figure 2.45 (b). Control over the temperature gradient and growth rate is essential. The addition of a small amount of solute increases the instability of the interface, therefore making dendrite formation more likely. Moreover, a faster cooling rate reduces the time for lateral diffusion of the rejected solute, which leads to the formation of smaller cells and a lower DAS (dendritic arm spacing) to prevent constitutional supercooling [234]. Practically, in nonferrous alloys, a larger freezing range is observed, and because of that, the S/L interface experiences constitutional supercooling. In 7075 aluminium alloy, the freezing

range is between 477 and 635 °C [242]. So, the formation of cellular and dendritic structures makes sense to understand the probability of liquid getting trapped in between the arms and leading to the formation of a shrinkage cavity because of chemical inhomogeneity, finally, it creates micro-shrinkage porosities. The problem is also arising from solute redistribution because of the transformation in diffusional properties of the solid and liquid [218].

2.4.1.1 Cellular structure development

As previously mentioned, the small amount of solute content leads to the perturbation at a constitutionally supercooled S/L interface is a transient phenomenon. At the tip of the perturbation, a solute is readily ejected out and captured in the lower section of the interface and the further tip grows slowly, as shown in Figure 2.45 [243].
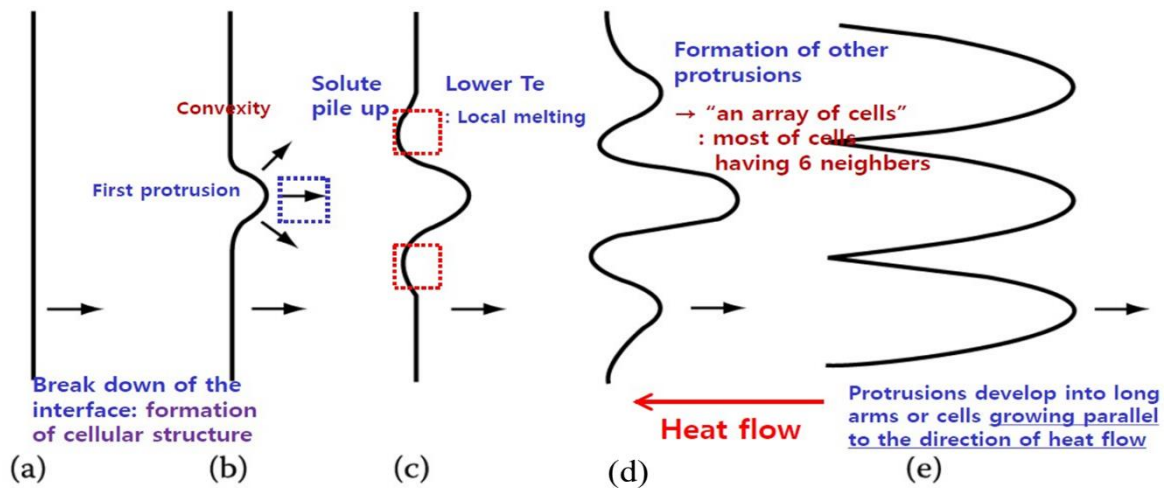

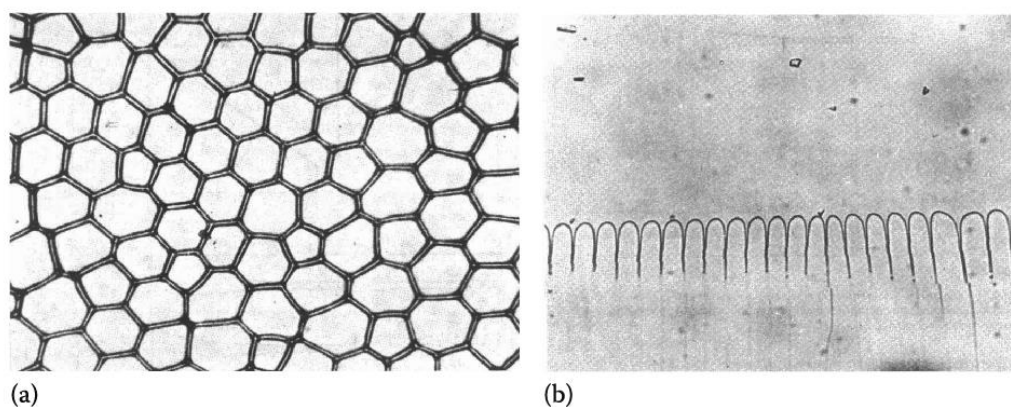**Figure 2.45 Temperature gradient, solute distribution for cellular growth** [243]**.**

Figure 2.46 A decanted interface of a cellular solidified Pb-Sn alloy (x 120) [244] **(a), and Longitudinal view of cells in carbon tetra-bromide (x 100)** [245] **(b).**

49

The development of cellular structure arises when the temperature gradient of the planar interface is reduced below the critical gradient, and instability of the interface starts because of constitutional supercooling at superheated liquid. The resultant morphology of these creates transverse periodicity in the solidification process, as shown in Figure 2.46 (a) & (b) [246]. During the cellular solidification, and even after that, there is an entrapment of a solute concentration in between the liquid of the cell. It creates segregation in the cells with eutectic in the cell walls, as shown in Figure 2.47 [229].
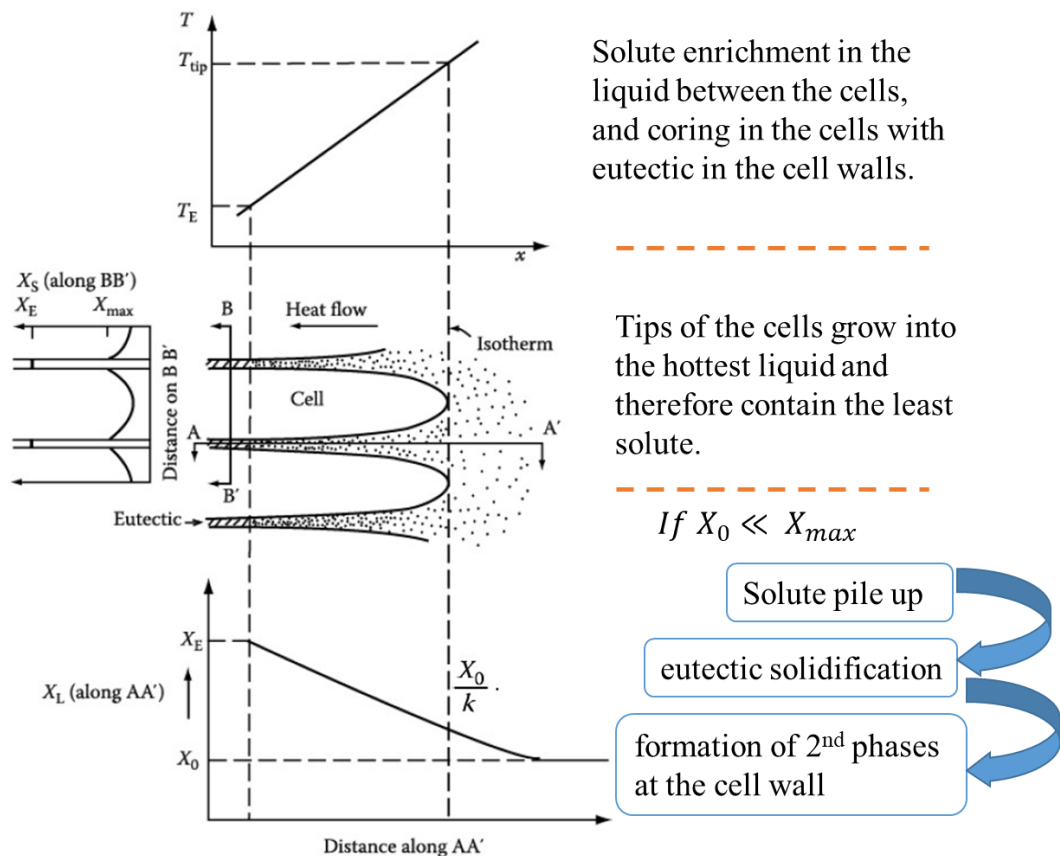
Figure 2.47 Solute profile and temperature gradient illustrating cellular segregation with eutectic cell walls where less segregation at the tip, and higher segregation at the lateral lower side between the cell walls [229].

The segregation can be reduced by decreasing diffusion during the cooling of a solidified object or subsequent homogenization annealing treatment. However, the dislocation associated with the solute at the cellular boundaries hinders the movement of the solute and reduces the efficiency of homogenization treatment. Kim et al. studied the direct squeeze cast 7075 wrought alloy by application 25, 50, and 75 MPa pressure, and found coarse

cellular structure with the eutectics at the periphery of the cell walls has micro-shrinkage cavities of non-pressurize as-cast Al7075. Increasing the pressure of squeezing (of 75 MPa) during solidification has changed the microstructure of cell size of 12.22 μm from 48.17 μm cell size of unpressured as-cast 7075. The subsequent ageing treatment at 120 °C for 36h reduced the eutectic segregation by a uniform distribution of eutectic within the matrix, which has improved the wear properties of the same [247].

2.4.1.2 Dendritic growth

During cell structure formation, the liquid is still in a positive temperature gradient (superheated condition), and the constitutional supercooling region is much less. When the critical temperature gradient of the liquid temperature lowers, it experiences some supercooling and develops a few features of dendrites in a cell structure known as cellular dendrite. Further decrease of a critical temperature gradient, the zone of supercooling is extensively larger, which produces independent nuclei of equiaxed dendrites [209, 218, 229, 234].

In cellular dendrite formation, the cell tip is a square pyramid shape instead of a flat curved dome. Cells form a square pattern which develops dendritic arms by changing the primary axis away from the heat flow direction, as shown in Figure 2.48. Cellular dendritic development occurs when the liquid temperature gradient is positive but not pronounced. Solute rejection diffuses into the liquid, but latent heat is still emitted into the solid. It can also control crystallographic factors such as shape and growth direction [248].
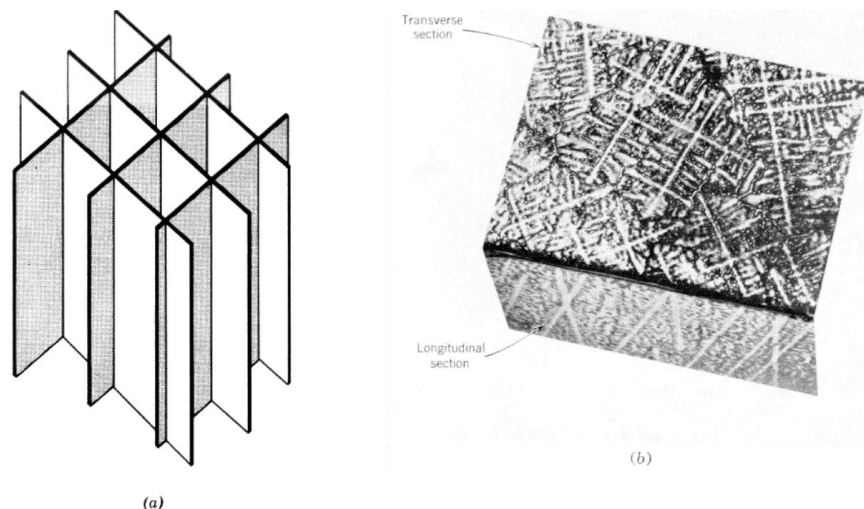

Figure 2.48 Cellular dendrites, dendritic arms in {100} planes (a), growth of dendrites are independent of its adjacent [230, 234].

The determination of significant growth of either cellular or cellular dendrites can be calculated by an experimental study proposed by Morris, Tiller, Rutter, and Winegard [249]. Tiller and Morris [250] studied lead-tin alloy liquid composition C_0/k_0, temperature gradient (G), and growth rate (R) is considered to determine cellular growth (G/R) or cellular dendritic $(G/R^{1/2})$.

The change from the cellular dendrite structure to the free dendrite structure happens naturally when supercooling at the interface increases drastically. The speed of progression of the growing tip in a free dendritic growth is only affected by "temperature" and "composition". The shape and growth of a crystal are determined by the local growth conditions instead of any externally applied temperature gradient [248, 251]. The local growth conditions are favourable to produce branched tree-like structures referred to as free equiaxed dendrites, while forced temperature gradient produces plate-like structures referred to as cellular dendritics. The contrast in growth behaviour could be attributed to the fact that the branches of the free type of dendrite cease development once they consumed the local supercooling, yet those of the cellular type persist in growth due to the constant heat extraction, potentially resulting in the branches combining into plates, as shown in Figure 2.49 [226].
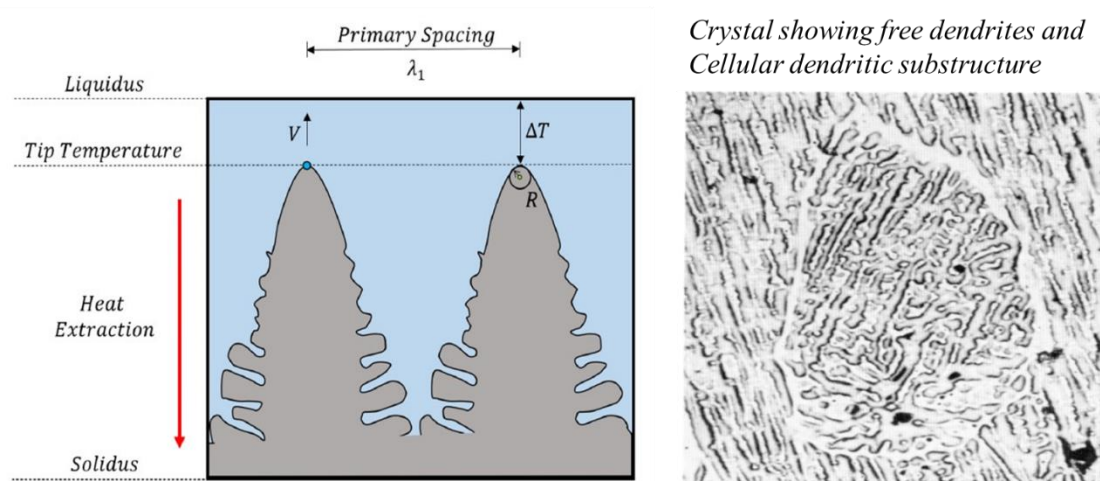

Figure 2.49 Cellular dendrite grows opposite to the heat extraction (a), and a combination of free dendrites and cellular dendrite in microstructure (b) [226]**.**

However, the rejection of the solute adds another difficulty and causes slower growth that would be observed in pure metal. The liquid in contact with an interface at the tip of the growing dendrite has a higher solute concentration than that of an ambient liquid, which

decreases the local equilibrium temperature of the volume element, hence effective supercooling decreases. The entrapment of liquid in the solid dendrites causes the problem of solute segregation. During the solidification, liquid shrinks in between secondary dendritic arms, and creates the problem of shrinkage porosities, as shown in Figure 2.50.
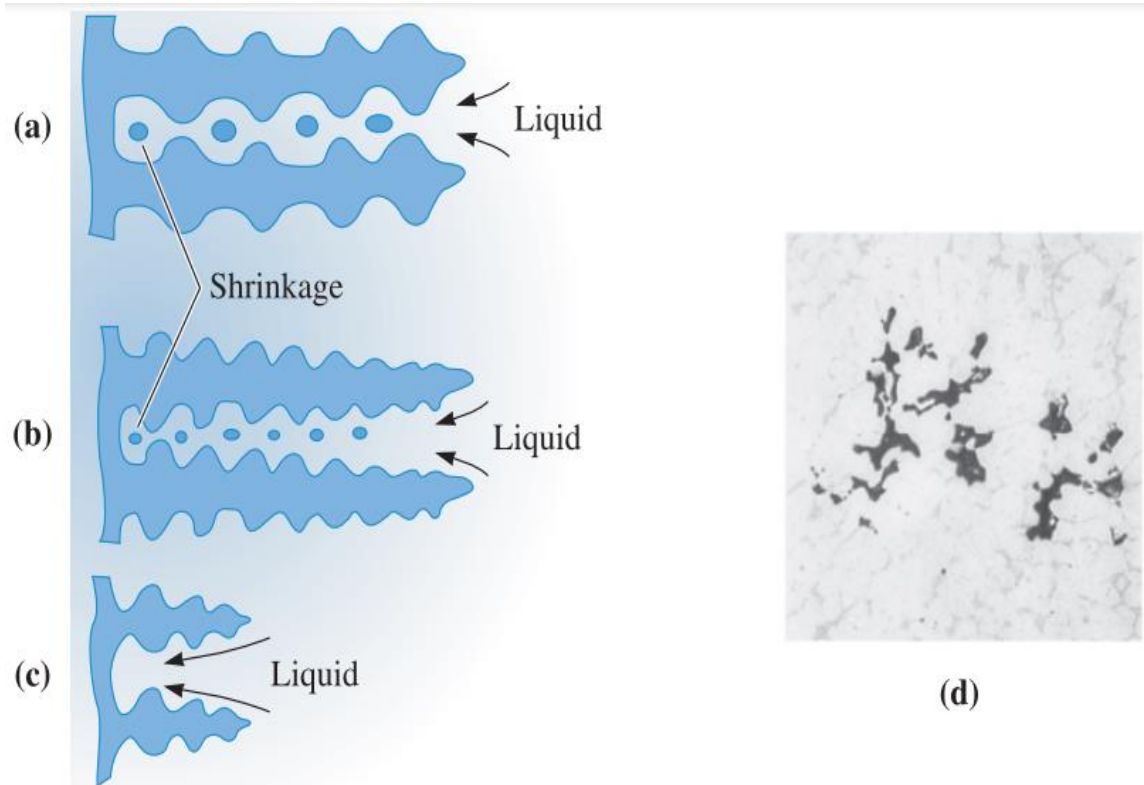

Figure 2.50 (a) Shrinkage can occur between the dendrite arms. (b) Small secondary dendrite arm spacing results in smaller, more evenly distributed shrinkage porosity. (c) Short primary arms can help avoid shrinkage. (d) Inter-dendritic shrinkage in an aluminium alloy (X 80) [219]**.**

2.4.1.3   Macro and Micro-segregation [229]

Cellular or dendritic morphology is created because of the instability of the S/L interface, which leads to the problem of chemical micro-segregation. Segregation of solutes during solidification refers to the non-uniformity of the chemical composition. The patterns of solute distribution result in a segregation pattern that may be considered a chemical structure [223, 240]. Morphology development and segregation patterns are intertwined phenomena and can be subdivided into macro-segregation and micro-segregation. Micro-segregation is complex in the multi-component system. Earlier refinement treatment and dendrite tip undercooling treatment was employed to control the solute redistribution [229]. Macro-

segregation results from localised micro-segregation because of the physical movement of the liquid and solid phases [59]. The fundamental distinction between macro and micro-segregation lies in their respective scales. Heat treatment (solution treatment followed by ageing) is often an effective way to reduce or even eliminate micro-segregation, which is not the case for macro-segregation. Macro-segregation has a relation to the stable solidifying interface, which can change solute concentration in the liquid as determined by a steady S/L interface of melt (D_L/R). Unlike microsegregation can decrease and increase solute concentration locally at unstable interface, such as cells, grooves, and dendrites [229]. Macro-segregation can be caused by four major factors: solidification shrinkage and thermal contraction, differences in liquid density among the dendrites, dissimilarity in solid and liquid density, and convection currents driven by temperature-induced dissimilarities in liquid density, as shown in Figure 2.51.
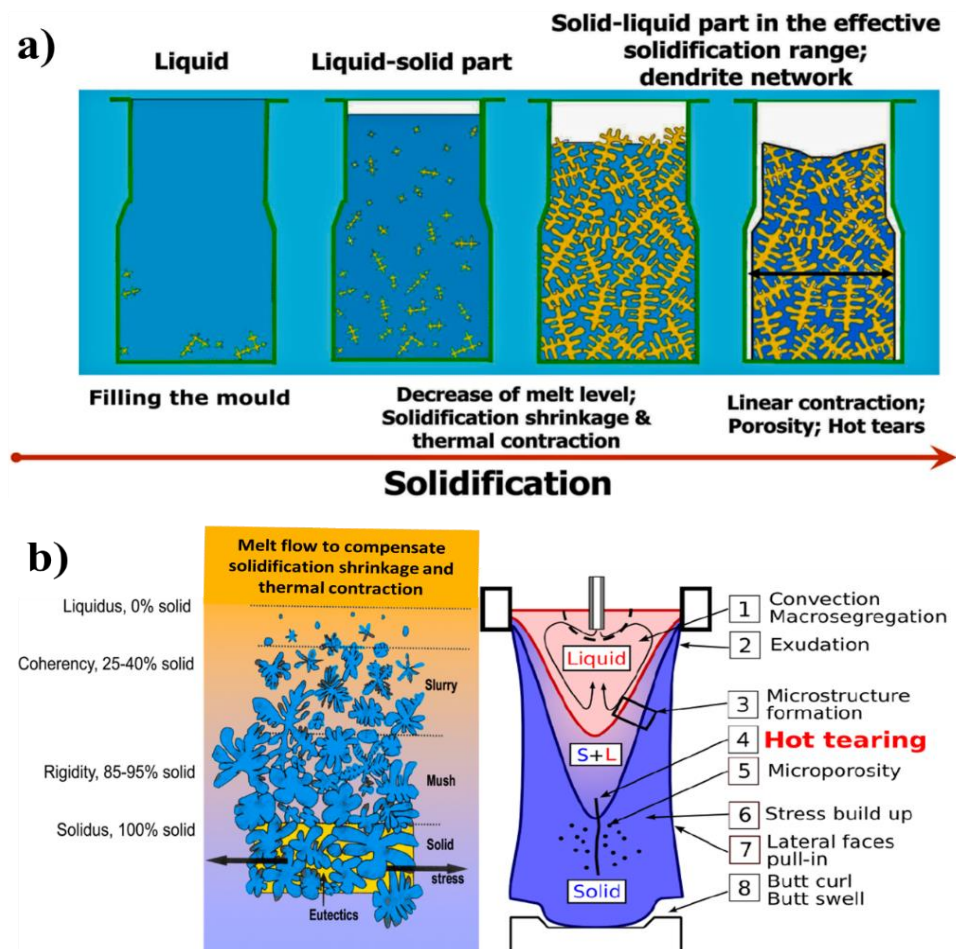

Figure 2.51 Schematic illustration of solidification shrinkage, thermal contraction, and linear contraction [252] **(a), Solidification behavioural characteristic points in the solidification range (left) and critical factors related to hot tearing (right) (b)** [18]**.**

Also, non-equilibrium solidification is accompanied by a certain degree of micro-segregation because of partitioning between solid-liquid interfaces [253]. The development of morphology by process parameters was studied in the literature. Figure 2.52 shows the correlation of the casting process, grain refiners and modifiers, and quenching media influence on the microstructure and segregation pattern.
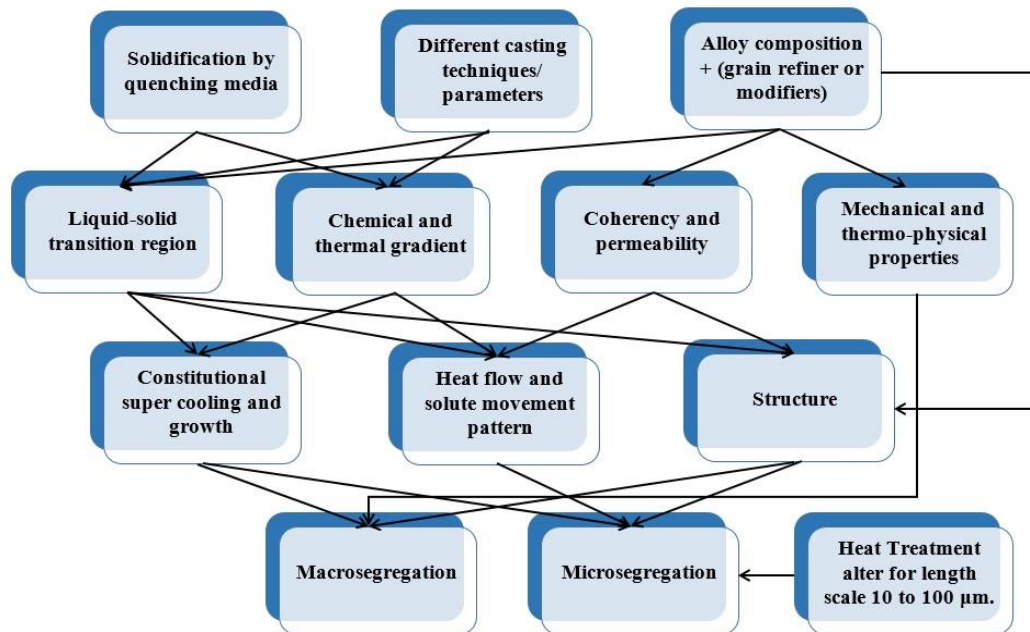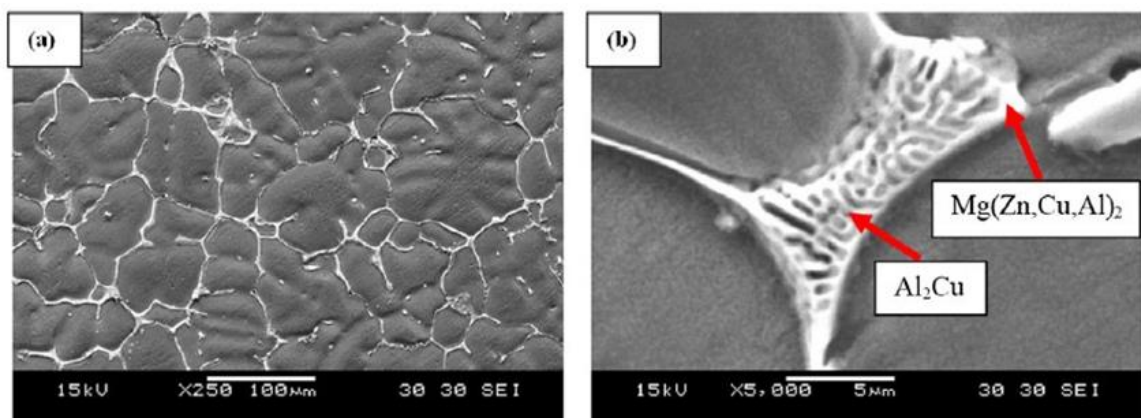

Figure 2.52 Casting process parameters, grain refiner/modifiers, and quenching media correlation between structure and segregation pattern.
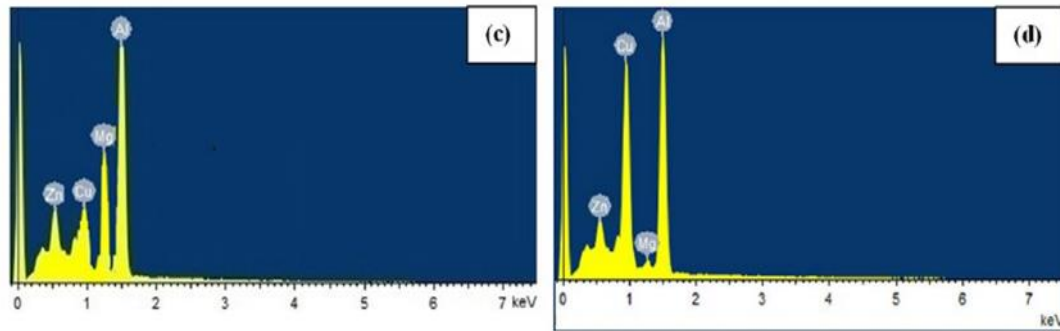
Figure 2.53 Microstructures of as-cast material (a) with a low level of magnification, (b) with a high level of magnification and EDS results of the intermetallic phases, (c) Mg (ZnCuAl)$_2$, and (d) Al$_2$Cu [254].

Gosh et al. [254] reported microstructural and textural development of Al7075 and found severe dendritic segregation in as-cast Al7075 because of non-equilibrium solidification, as shown in Figure 2.53. After homogenization treatment at 465 °C for (a) 15 min, (b) 6 h, (c) 12 h, (d) 24 h, (e) 48 h, and (f) 96 h, as shown in Figure 2.54, diffusion of solute atoms from the eutectic structure of primary η phase caused it to dissolve gradually during homogenisation treatment. Compared to Zn and Mg, the diffusion rate of Cu is slower, causing a greater concentration of Cu in this area. The presence of Cu at the grain boundary is enough to cause the S phase to nucleate, and after 6 h of homogenisation, the diffusion is then mainly Cu-controlled [61, 65, 254].

As a result, the reduction in the micro-segregation can be reduced by applying heat treatment. Even better distribution of the eutectic phases of as-cast can be achieved by the application of precipitation hardening or ageing treatment. Hence, the mechanism of heat treat is essential for understanding the homogeneous distribution of precipitates.
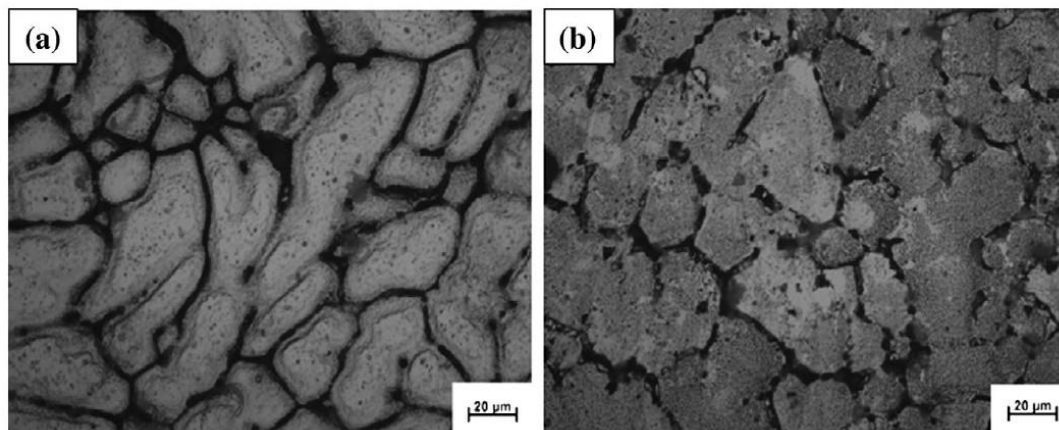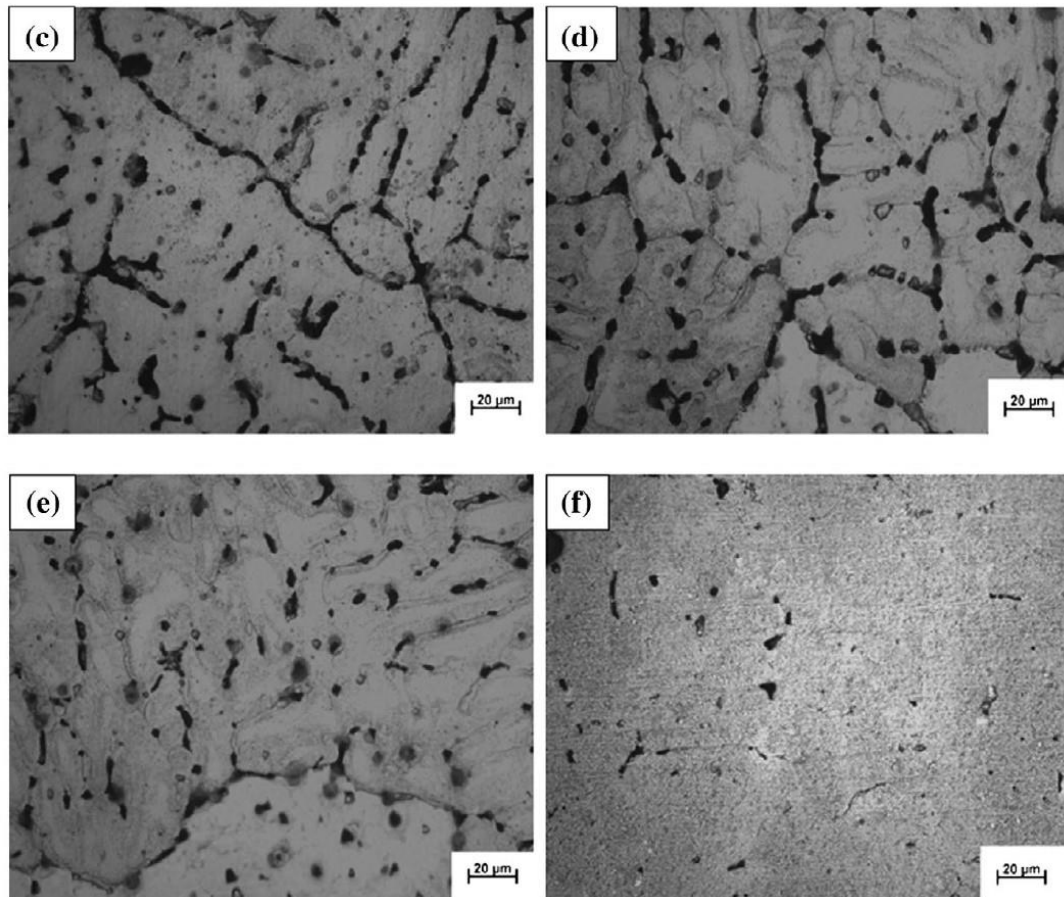
Figure 2.54 Optical micrograph of homogenised alloy at 465 °C for (a) 15 min, (b) 6 h, (c) 12 h, (d) 24 h, (e) 48 h, and (f) 96 h [254].

2.5   Heat Treatment of 7XXX aluminium alloys

Aluminium alloys are divided into heat-treatable and non-heat-treatable, depending on their response to precipitation hardening. Heat-treatable alloys like 7XXX, 6XXX, and 2XXX have alloying elements that are more soluble at higher temperatures than at room temperature. Different kinds of literature have discussed the generalised illustration of precipitation hardening for the Al-Cu phase [255] in Figure 2.55. The Al-4.5Cu phase diagram shows that full copper dissolution will occur when holding at 268 to 288°C, and is known as the solution heat treating temperature. The equilibrium structure of $Al + CuAl_2$ forms with slow cooling produces coarse and incoherent $CuAl_2$, while rapidly cooled alloy cannot produce $CuAl_2$ precipitate, hence a supersaturated solid solution formed. Natural ageing or artificial ageing is used to control the size and distribution of the precipitate dispersion in the matrix at room temperature and optimise the mechanical and corrosion properties of
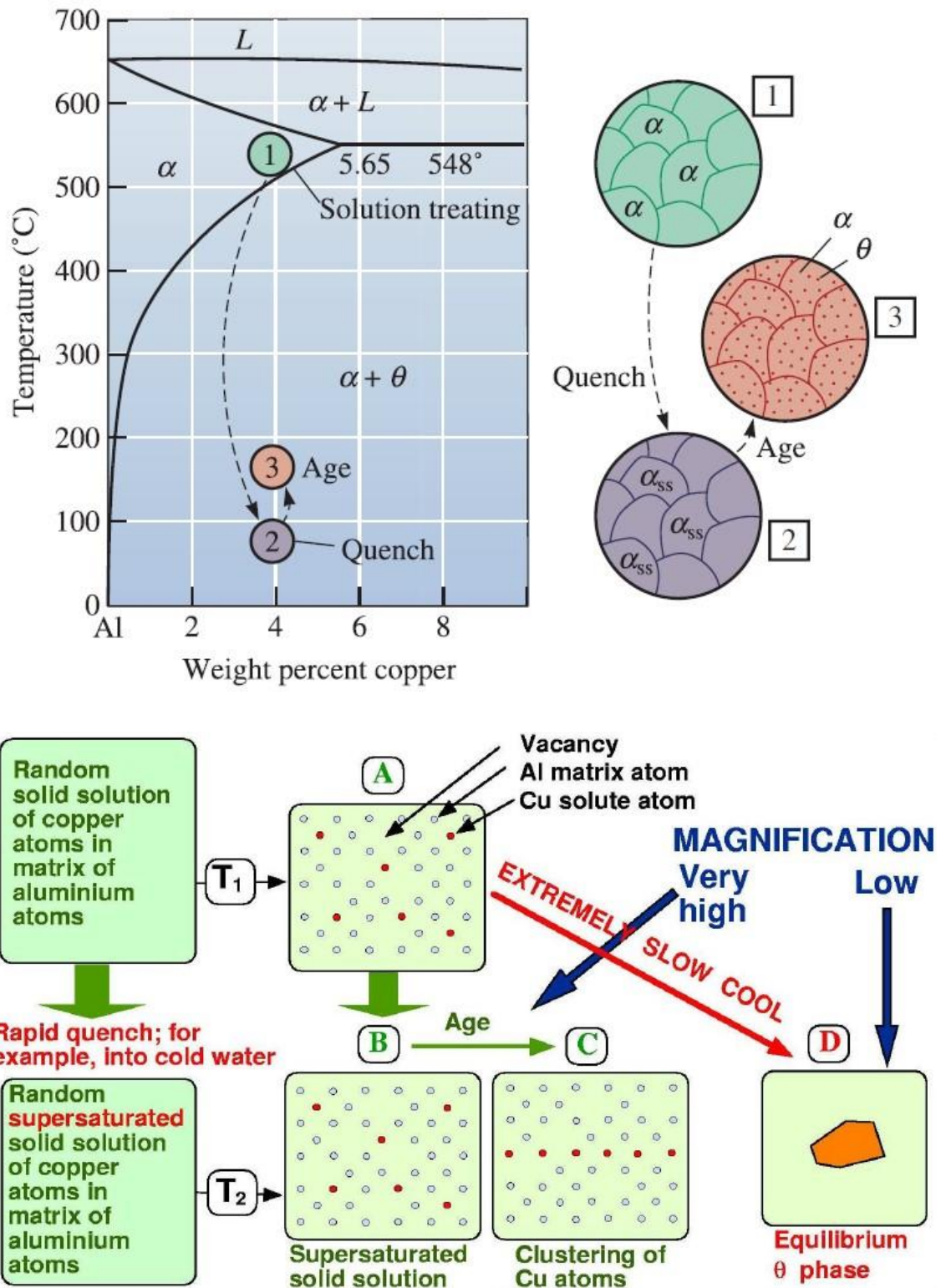
these alloys [256].

Figure 2.55 The aluminum-rich end of the aluminum-copper phase diagram showing the three steps in the age-hardening heat treatment (above), and the effect of slow cooling and rapid cooling on the microstructure [219].

Heat-treatable aluminium alloys use the temper designation system to decide the sequence of treatments, which can be mechanical, thermal, or both together, as shown in Figure 2.56. It also offers information on the heat treatment parameters that are applied to the alloy, like time, temperature and quenching rate [257]. According to the heat treatment tempers, 7XXX aluminium alloys are heat-treated by applying solution treatment, followed by artificial ageing (T6) traditionally [256]. As per a research review, retrogression and re-ageing (RRA) heat treatment is better than other common heat treatments like T6 and T7X. Moreover, using heat treatments like duplex ageing, multistage ageing and double ageing may have a more beneficial impact on the properties of 7xxx alloys [258]. The United States created Al 7075 alloy in 1943 and it used the T651 heat treatment temper for the B-29 bomber, which sped up the growth of high-strength aluminium alloys in the aviation sector. Afterwards, for the first time in 1956, the former Soviet Union included the Zr element in the Al-Zn-Mg-Cu series of alloys to prevent recrystallization. And then later, the double-step ageing process was implemented on Al7075 in 1960 [30]. Decades to decades, development of 7XXX aluminium alloys strengthened from 1st generation to now 5th generation aluminium alloys.
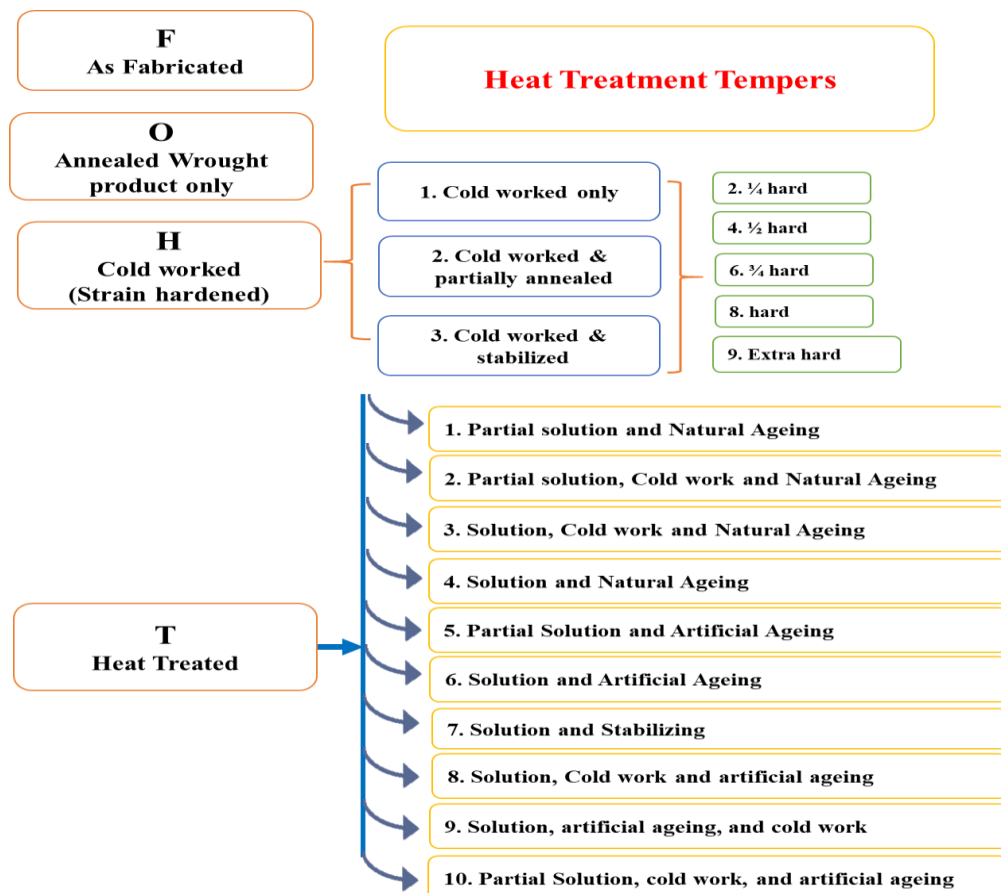

**Figure 2.56 Tempers' designations for aluminium alloys** [257].

2.5.1 Precipitation hardening or age hardening treatment of 7XXX aluminium alloy

2XXX, 6XXX, and 7XXX aluminium alloys are hardened by heat treatment because of the metallurgical characteristic of full solute solubility at high temperatures but only limited solute solubility at room temperature. As mentioned earlier, solution treatment followed by artificial ageing is the most applicable ageing treatment on the 7XXX aluminium alloys, particularly on Al7075. The aim of the ageing process is the fine dispersion of stable precipitates and to improve the mechanical, tribology, and corrosion properties of the materials [255, 257]. The dramatic distribution of precipitates in the Al7075 aluminium alloys needs more attention to strengthening mechanisms. Zinc and magnesium are the key components in obtaining a high strength in 7XXX aluminium alloys. Besides alloy addition in the base metal, there are several other fascinating strengthening techniques, including grain size reduction, precipitation hardening, dispersion strengthening, and work hardening. It may be one or a combination of these that is responsible for the final properties and drawbacks [258].

The heat treatment for 7XXX alloys is to get a uniform distribution of Zn, Mg, and Cu atoms in the Al matrix, which increases homogeneous solute atom clustering. It is a well-known precipitation sequence which is concurred by many researchers in the following sequential transition because of the lower activation barrier [47].

$$\alpha_{ssss} \rightarrow GP\ Zone\ (spherical) \Rightarrow \begin{matrix} \eta' \rightarrow \eta \\ T' \rightarrow T \end{matrix}$$
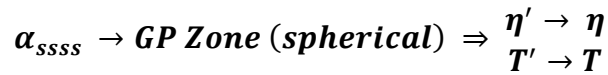
Establishing GP zones is a necessary step before the formation of the final precipitation, as is shown in Figure 2.57.
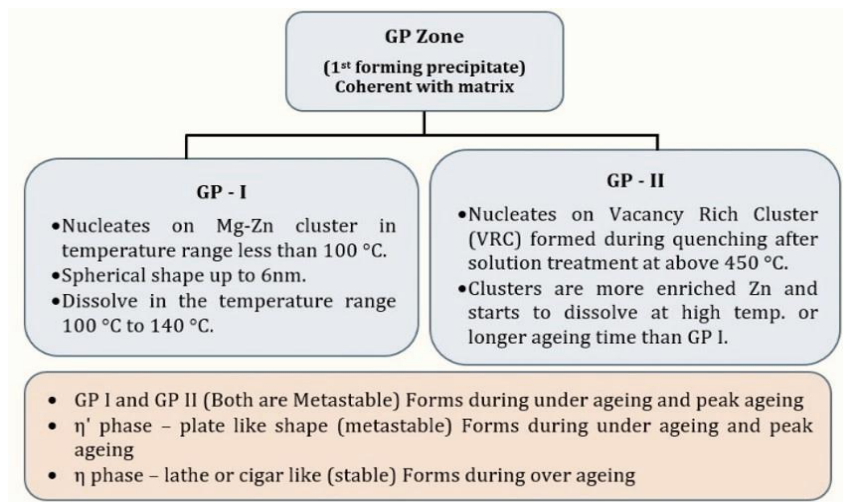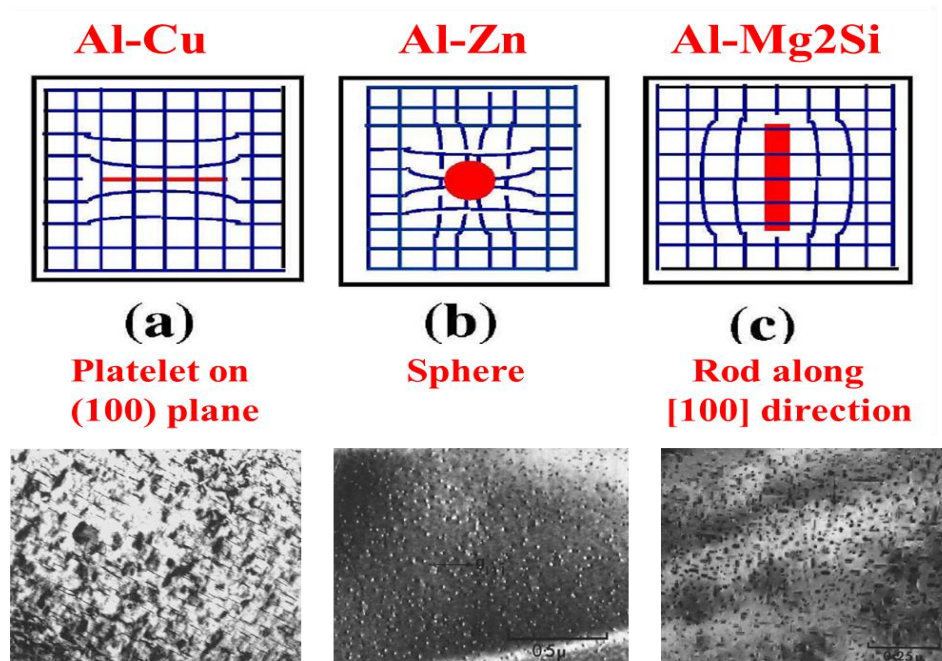
Figure 2.57 Difference between GP-I and GP-II (above), and GP zone morphology in different aluminium alloys (below) [259, 260].

An important concept related to the coherency of the GP zones is important for the hardening of an aluminium alloy, which is composed of clusters of solute atoms that may be coherent, semi-coherent, and incoherent, with the aluminium lattice [261]. Immediately after solution treatment, Al-Zn-Mg alloys create Zn-vacancy clusters and Mg aggregates. After a few months of natural ageing, GP zones are formed. It has been documented that when the naturally aged material is subjected to a temperature of 95 °C, the reversal of Mg-rich clusters and the conservation of Zn-vacancy clusters has occurred. Raising the heat treatment temperature to 150 °C results in semi-coherent or incoherent precipitates, and also stability of Zn-vacancy is observed at initially 30 mins [262]. The schematic illustration of the solute segregation at grain boundaries during the GP zone and PFZ formation of ageing treatment is shown in Figure 2.58. Zhao et al. [221] investigated a bulk model for Al-Zn-Mg-Cu alloy and set heat treatment parameters as at 475 °C solution treatment, followed by an early stage of ageing and peak ageing at 120 °C and 180 °C, respectively. So, the scaling of the formation of precipitates with respect to time varies from macro, micro, nano or even atomic level, as shown in Figure 2.59 (a) [261]. The coherency with the matrix lattice, softness & hardness, and size of the precipitates affect dislocation motion, which decides the strength of the aluminium alloys. The soft and apart spherical precipitates are cut through by dislocation, while hard and smaller inter-distance entangles in between and creates a loop,

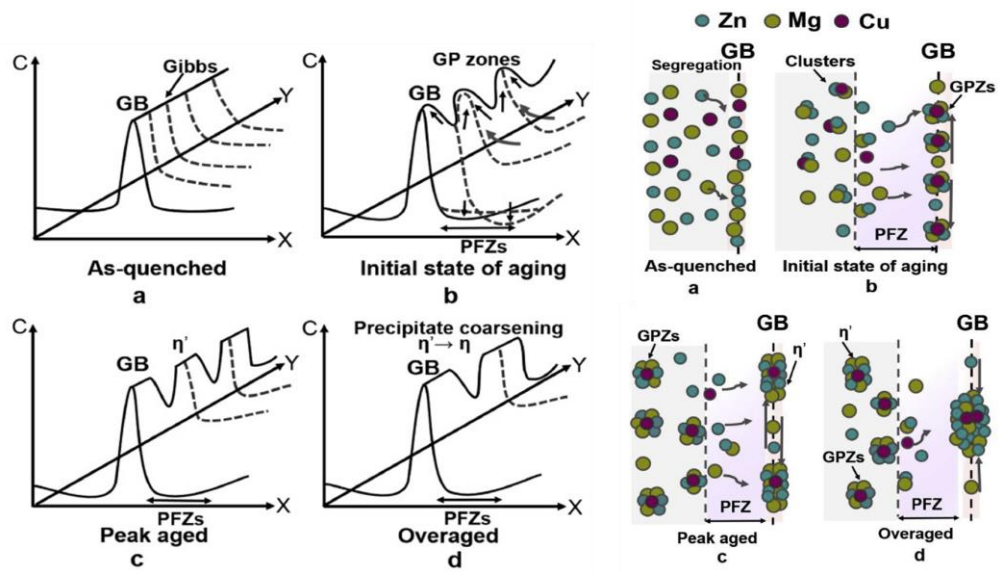known as Orowan looping, as shown in Figure 2.59 (b) & (C) [263].

Figure 2.58 Schematic illustration of solute segregation at grain boundaries during GP zone and PFZ formation of ageing treatment [221].
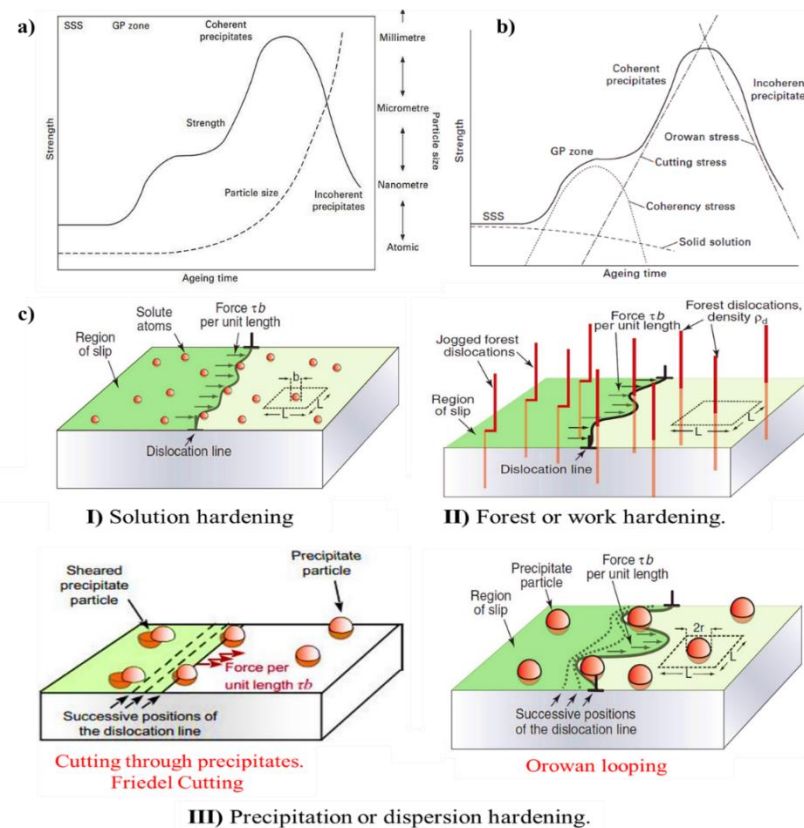

Figure 2.59 (a) Effect of ageing time on strength (solid line) and particle size (dashed line) during the thermal ageing process [261]**, (b) Precipitation hardening mechanisms with each**

successive stage in the strength–time graph[261], and (c) dislocation hindrance by solution hardening (I), work hardening (II), and precipitation hardening with Friedel cutting (Soft ppt.) & Orowan looping (hard ppt.) [263].

To maximise dispersion strengthening, several factors must be considered: (a) the precipitate should be hard and scattered, while the matrix should be continuous and pliable, (b) the dispersed phase particles should be tiny and in abundance, (c) the dispersed phase particles should be spherical instead of long and thin, and (d) an increased quantity of the dispersed phase will result in a greater strengthening effect, as shown in Figure 2.60 (a) to (d) [219].
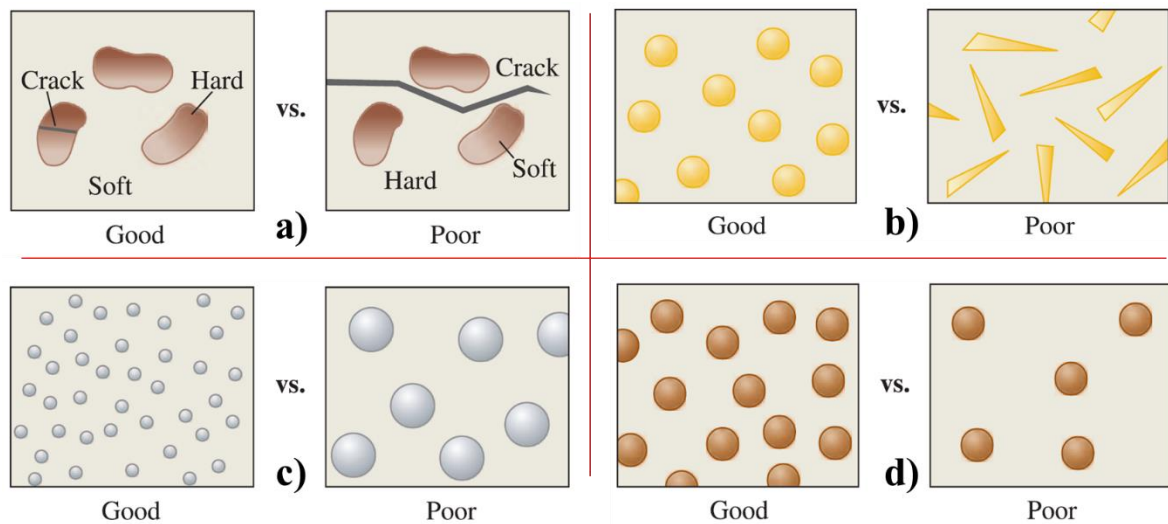

Figure 2.60 Illustration of the distribution of precipitates in the matrix and their morphology for greater strengthening effect: (a) hard and discontinuous precipitates with continuous and soft matrix, (b) precipitates particles should be round, (c) precipitates should be small and many, and (d) large amount of precipitates [219].

The summarized investigation of the 7XXX aluminium alloys is reviewed by Azarniya et al., as presented in Table 2.10.

Table 2.10 A summary of precipitates in aged 7XXX series Al alloys and their basic details.

Ageing Alloy System	Heat Treatment	Precipitates	Precipitates sequence	Ref.
7175 (Al-Zn-Mg-Cu)	Hot extrusion and Subsequent natural ageing	Al_2CuMg, $Al_{12}Mg_2Cr_2$	$Al_{12}Mg_2Cr_2$ precipitates are detrimental to subsequent hot deformation due to a strong possibility of re-melting.	[264]
Al-Zn-Mg-Cu	Non-isothermal Ageing	Al_3Zr, $\eta(MgZn_2)$, $\eta'(MgZn_2)$	The precipitates are often nano-metric in size and form along the grain boundaries or throughout the grains.	[265]

Al-Zn-Mg-Cu	Non-isothermal ageing	GPs, η, η′, T, S	Al-Zn-Mg-Cu GP zones form at 40-100 °C but immediately dissolve at 124 °C. At 186 °C, η′ phase starts to form, but it begins to dissolve up to 216 °C. At 240 °C, the η phase emerges, but it completely transforms into T and S phases at 264 °C.	[266]
High Zn containing Al-Zn-Mg-Cu	Two-step ageing	Al₃Zr, GPs, η	The precipitates are formed as elliptical or elongated along the grain boundaries and within the grains discontinuously.	[267]
7017 (Al-Zn-Mg)	Artificial ageing	GPs, η, η′	Unlike the η′ phase, η forms within the grain boundaries, but their geometrical size depends on the ageing time.	[268]
Al-Zn-Mg-Sc-Zr	Artificial ageing	GPs, η, η′, Al₃(Sc,Zr)	When Zr is present in the alloy, the coherent phase Al₃(Sc, Zr) may form. The formation of these fine precipitates suppresses the generation of GP zones and declines the relative content of η′.	[269]
Al-Zn-Mg-Sc-Zr	Artificial ageing	η (MgZn₂), T (Mg₃₂(Al,Zn)₄₉, Al₃(Sc,Zr)	The precipitates often form both inside the matrix grains and grain boundary regions. These particles can pin mobile dislocations or grain boundaries, and suppress the recrystallization.	[270]
7075 (Al-Zn-Mg-Cu-Zr)	Artificial ageing	Al₃Zr, Al₃(Sc,Zr), η, η′	The Al₃Zr phase forms as equiaxed 20-30 nm particles. As Sc is added to the alloy, the phase Al₃(Sc, Zr) starts evolving.	[271]
Al-Zn-Mg-Cu-Sc-Zr	Hot extrusion and subsequent artificial ageing	Al₃(Sc,Zr), GPs, η′	This alloy indicates a double-peak ageing curve due to the overlap of the precipitation of GP zones and η′ phases.	[272]
Al-Zn-Mg-Cu	Tensile stress-ageing treatment	GPs, η′(MgZn₂), η(MgZn₂)	The ageing under a tensile stress leads to a double-peak ageing curve. The tensile stress persuades the growth of the MgZn₂ phase, accelerates the formation of η′ phase, and suppresses the evolution of η phase.	[273]
Al-Zn-Mg-Cu	Two-stage stress ageing treatment	GPs, η′(MgZn₂), η(MgZn₂)	Two-stage stress-ageing treatment can result in the uniform distribution of in situ precipitates inside the grains and along the grain boundaries.	[274]
Al-Zn-Mg	Artificial ageing	η′(MgZn₂), η(MgZn₂), τ(MgZn₂) under overaged conditions)	There is a reverse relation between the ageing response of the alloy (i.e. micro-hardness) and the lattice parameter.	[275]
Al-Zn-Mg-Cu	Pre-ageing treatment and subsequent artificial ageing	GPs, η′(MgZn₂), η(MgZn₂)	A pre-ageing treatment after quenching of the alloy enables the accelerated formation of stabilized GP zones. These zones can effectively serve as precursors for the formation of the metastable phase η′.	[276]

7075 (Al-Zn-Mg-Cu)	Tensile stress-ageing treatment	GPs, η′(MgZn$_2$), η(MgZn$_2$)	While the external stress at low-temperature ageing declines the average size of GP zones, it promotes the formation of η′ precipitates at high-temperature ageing.	[277]
Al–Zn–Mg–Cu-Zr-Ti	Artificial ageing treatment	GPs, η′, L12-(Zr$_{(1-X)}$Ti$_X$)Al$_3$	The phase L12-(Zr$_{(1-X)}$Ti$_X$)Al$_3$ has a low tendency to coarsen during ageing and improves the mechanical properties.	[278]
Al–Zn–Mg–Cu	Non-isothermal ageing	GPs, η′(MgZn$_2$), η(MgZn$_2$), T(AlZnMgCu), S(Al$_2$CuMg)	GP zones and η′ phase are the dominant precipitates during the heating stage, but η′ is the crucial phase at the cooling step. The phases T and S can form at high ageing temperatures ($\geq$290 °C).	[279]
Al-Zn-Mg-Zr-Sc	Artificial ageing	η′ (MgZn$_2$), η(MgZn$_2$), Al$_3$(Sc,Zr)	The η′ phase often forms in the sub-grains, but η is developed along the grain boundaries. Also, Al$_3$(Sc, Zr) has a nano-metric spherical shape.	[280]
Al–Zn–Mg–Cu	Non-isothermal ageing.	GPs, η′, η	The phase η′ forms as platelets with 1-2 nm thickness and 10-20 nm length.	[281]

2.6 Different casting techniques

There are various casting techniques employed to shape the aluminium alloys. The control over the casting solidification parameter results in the desired microstructure and properties of the castings. Moving the heat from the hot liquid to the mold is a complex process, and different heat transfers can be noticed while the cast solidifies. Heat transfer is a major factor, but different dimensions of this solidification create resistance to the heat flow. Those are largely affected by liquid cast metal, latent heat release, interface, solidified cast, types of mold, and the environment.
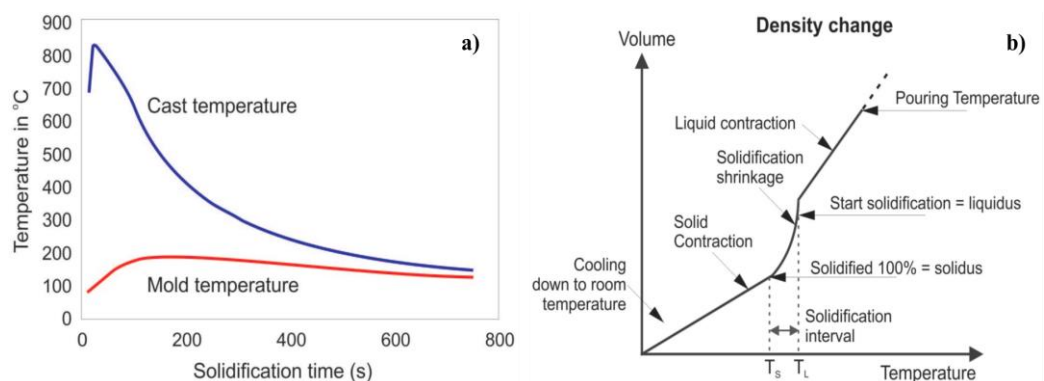

Figure 2.61 (a) Solidification curve for Al 6061, (b) generalised solidification curve for alloy [282].

Different casting techniques like sand casting, investment castings, and permanent mold casting have different mold characteristics in terms of heat dissipation. As solidification and growth start from the mold walls, and release of latent heat release plays a major role in constituting the microstructure [282]. Zakaria et al. [282] studied the casting process modelling for the Al 6061 and found a solidification curve for cast and mold temperature, shown in Figure 2.61. The variation in the thermal gradient at the mold wall generates undercooling and creates different grain morphology, as illustrated in Figure 2.62.
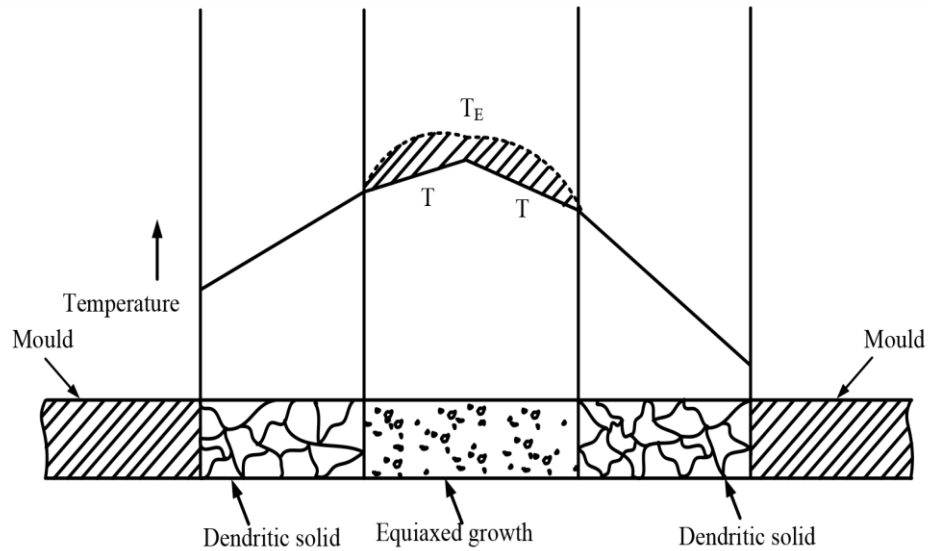

Figure 2.62 Variation of undercooling with alteration in the thermal gradient, showing different grain morphology [37].
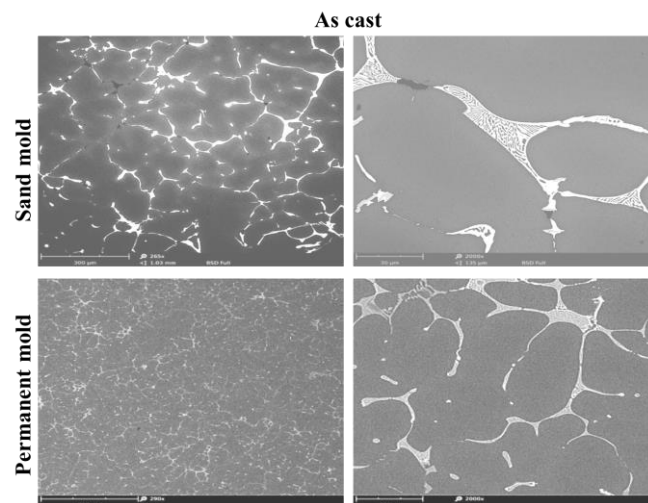

Figure 2.63 Microstructures of the material after sand and permanent casting [283].

Krzysztof et al. [283] studied the microstructure of sand cast and permeant mold casting, and

found a larger globular grain of α-Al in the sand cast compared to permanent mold casting, as shown in Figure 2.63. Reddy et al. [284] used alumina shell molds to cast Al 7075 and studied its microstructure and mechanical properties. The sample has a gradual decrease in hardness from the outer area to the inner area, as shown in Figure 2.64.
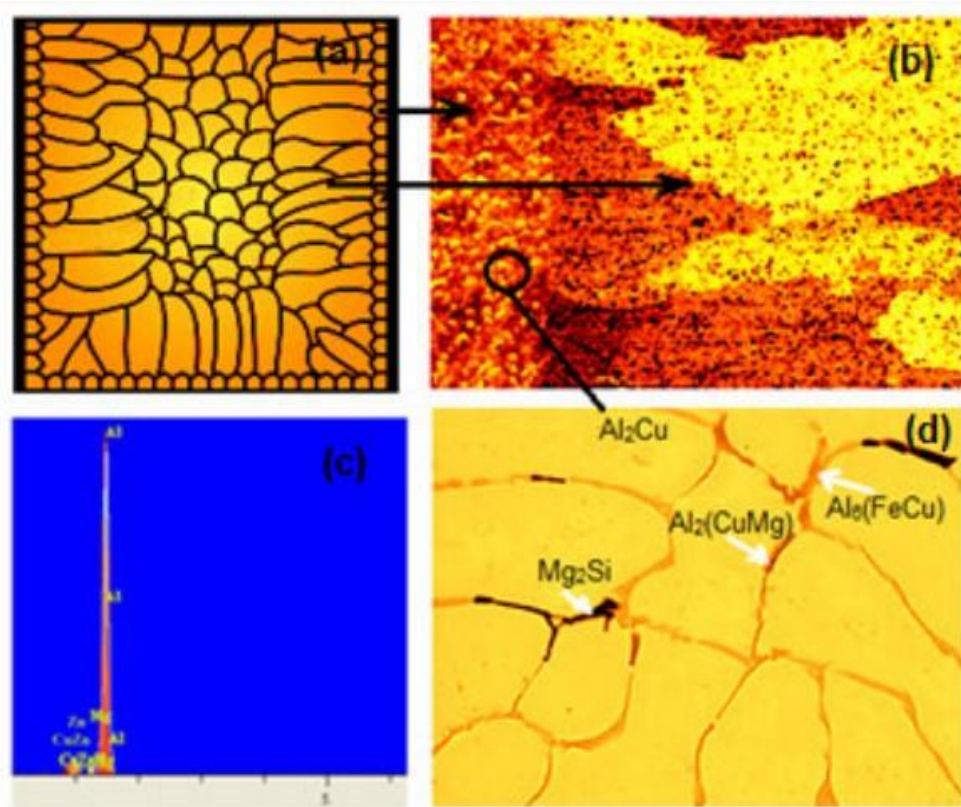

Figure 2.64 Metal-mould reaction (a) schematic representation grain formation in shell mould, (b) fine grain structure as metal-mould interface (c) EDX graph representing metal-mould reactions and (d) formation of intermetallic phases due to metal-mould reactions [284]**.**

As a result, the multiple casting methods have distinct mold features of heat dissipation, and their effect on the microstructure is an intriguing area to research in the eutectic stage formation.

2.7 Application of 7XXX aluminium alloys

The 7075 is the high-strength alloy of the 7XXX series, and its wide application to the structural components, aircraft structures and fittings, automobiles, security weapons, aerospace and defence applications [64, 77, 211]. The strength spectrum of aluminium alloys shown in Figure 2.65, Al 7075 has high strength among all. For the widespread application

of the alloy, the modification of existing alloys and re-melting or recycling is a necessary step towards maintaining the inventory of the aluminium alloys.
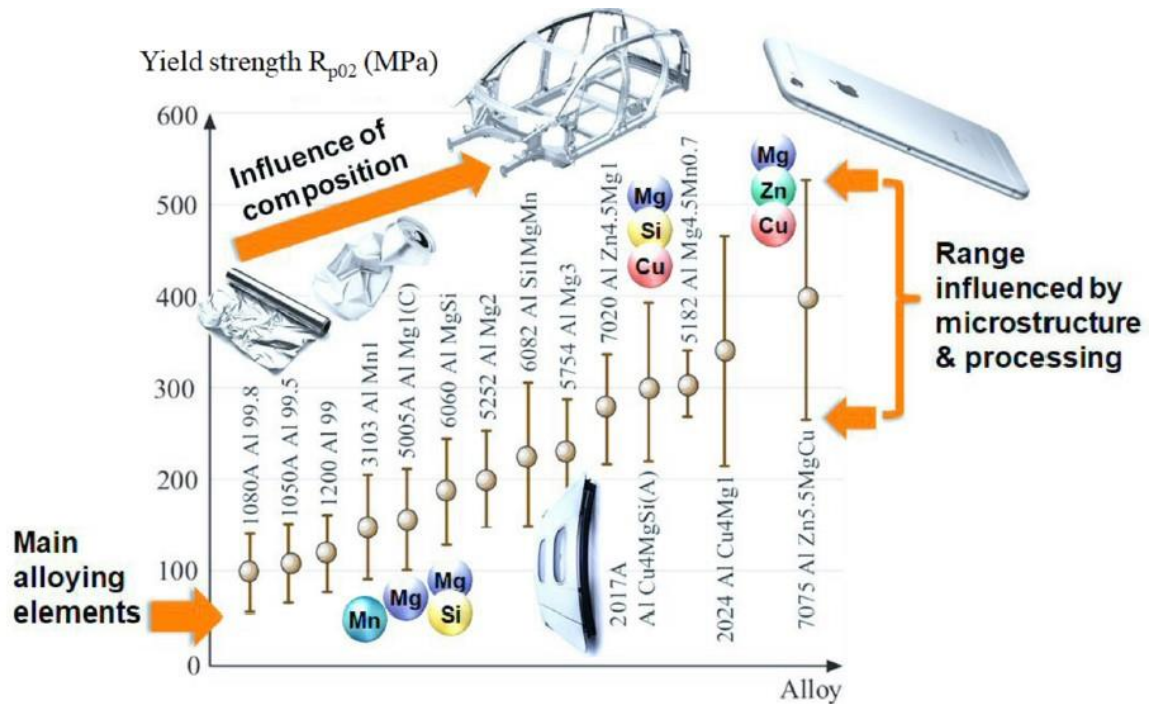

Figure 2.65 Strength spectrum of aluminium alloys [77]**.**

2.8   Research Gap

A research gap was identified after a thorough literature review. The major challenge is the application of Al 7075 by the casting route because of the solute segregation problem. The production of Al7075 by casting route might replace the costlier processing of wrought 7075 aluminium alloy. As per the literature survey, the wrought 7075 aluminium alloy has high strength, nearly similar to steel. The forming processes and secondary operations to get the final product are significantly costlier. Many researchers studied cast Al 7075 by adding grain refiners, modifiers, and micro-alloying elements to achieve significant mechanical properties. After an extensive literature survey, the present study focuses on changing the eutectic phase segregation pattern by adding high-temperature oxides like ZrO_2, TiO_2, and $ZrTiO_4$ in the cast Al7075 by die casting route. The comparative effect of these three oxides on the cast Al 7075 and their natural ageing is a novel study. However, the study on the solute segregation pattern and the intermediate phase formation within the microstructure is quite complex but essential to solving the problem of cast Al 7075.

A detailed discussion in the literature, the addition of grain refiners or modifiers (chemically), controlled diffusion solidification (thermally), mould vibration (mechanically), or a combination of either can alter solute segregation patterns. Another aspect of the study is focused on microstructural morphology and mechanical properties by quenching cast Al7075 in ice, hot water for 30 minutes, and hot water until cooled down. A similar work is hardly reported in the present literature. Further, a study on the different casting techniques is performed to produce the cast Al 7075 by permanent mould casting (gravity die casting), sand casting, and investment casting. The mould characteristics play a significant role in the solidification of cast Al 7075, which influences the solute segregation and phase morphology of the final microstructure.

The double step-ageing of oxide-added cast Al 7075 was studied to compare microstructure and mechanical properties before and after the heat treatment. SEM-EDS and XRD analysed the precipitate phase to understand the precipitation behaviour. The double-step ageing cycle is unique, as most literature studied conventional T6 treatment, retrogression and re-ageing or either homogenization treatment.

The cast Al 7075 was developed by alloying and compared the microstructure and properties with the wrought Al 7075. The motivation for development is the high cost of the wrought Al 7075. The chemistry was achieved after the four successive heats, but achieving mechanical properties is challenging. However, the developed as-cast results are promising compared to as-cast Al 7075 produced from Al 7075-T6.